THE SPIN STRUCTURE OF ^{3}He AND THE NEUTRON AT LOW Q^2: A MEASUREMENT OF THE GENERALIZED GDH INTEGRAND

A Dissertation

Presented to

The Faculty of the Department of Physics

The College of William and Mary in Virginia

In Partial Fulfillment

Of the Requirements for the Degree of

Doctor of Philosophy

---

by

Vincent Anthony Sulkosky

August 2007

ABSTRACT

Since the 1980's, the study of nucleon (proton or neutron) spin structure has been an active field both experimentally and theoretically. One of the primary goals of this work is to test our understanding of Quantum Chromodynamics (QCD), the fundamental theory of the strong interaction. In the high energy region of asymptotically free quarks, QCD has been verified. However, verifiable predictions in the low energy region are harder to obtain due to the complex interactions between the nucleon's constituents: quarks and gluons. In the non-pertubative regime, low-energy effective field theories such as chiral perturbation theory provide predictions for the spin structure functions in the form of sum rules.

Spin-dependent sum rules such as the Gerasimov-Drell-Hearn (GDH) sum rule are important tools available to study nucleon spin structure. Originally derived for real photon absorption, the Gerasimov-Drell-Hearn (GDH) sum rule was first extended for virtual photon absorption in 1989. The extension of the sum rule provides a unique relation, valid at any momentum transfer (Q^2), that can be used to study the nucleon spin structure and make comparisons between theoretical predictions and experimental data.

Experiment E97-110 was performed at the Thomas Jefferson National Accelerator Facility (Jefferson Lab) to examine the spin structure of the neutron and ^{3}He. The Jefferson Lab longitudinally-polarized electron beam with incident energies between 1.1 and 4.4 GeV was scattered from a longitudinally or transversely polarized ^{3}He gas target in the Hall A end station. Asymmetries and polarized cross-section differences were measured in the quasielastic and resonance regions to extract the spin structure functions $g_1(x, Q^2)$ and $g_2(x, Q^2)$ at low momentum transfers ($0.02 < Q^2 < 0.3$ GeV^2). The goal of the experiment was to perform a precise measurement of the Q^2 dependence of the extended GDH integral and of the moments of the neutron and ^{3}He spin structure functions at low Q^2. This Q^2 range allows us to test predictions of chiral perturbation theory and check the GDH sum rule by extrapolating the integral to the real photon point. This thesis will discuss preliminary results from the E97-110 data analysis.

Dedicated to the memory of my mother, B. Irene Sulkosky (1934-2004)

ACKNOWLEDGMENTS

During the course of the long journey to complete this dissertation, there have been many people who provided support, guidance and encouragement. First I would like to thank my thesis advisor, Dr. Todd Averett, who took this relatively inexperienced student and helped turn me into the young physicist I am today. His support and encouragement provided the incentive needed to complete this work. He also helped me to become independent and to think for myself.

Most of my graduate years were spent at Jefferson Lab, where I had the privilege to be mentored by Jian-Ping Chen. I would like to thank the spokespersons of experiment E97110 Jian-Ping along with Alexandre Deur and Franco Garibaldi for the confidence in my work and continued encouragement. I also would like to thank my committee members for their time in carefully going through this document and for providing useful feedback: David Armstrong, Mike Finn and Dirk Walecka . I am especially thankful to Todd and Jian-Ping for their guidance and advice in the preparation of this manuscript.

I would never have entered graduate school without the support and enthusiasm of my undergraduate physics professors: Anis Maize and John Smetanka. I will always be grateful for Anis and his physics lectures, which prompted me to consider graduate school. John was my undergraduate thesis advisor who I spent many days with learning about p-process nucleosynthesis.

Before running experiment E97-110, I had no idea how much work and effort went into running an experiment. I appreciate Jian-Ping's guidance and work ethic to ensure the experiment was installed safely and on time. In addition, I would like to thank the fellow graduate students, post-docs and colleagues that worked along side with me to ensure the experiment was a success: Patricia Solvignon, Jaideep Singh, Tim Holmstrom, Alexandre Deur, Robert Feuerbach, Kevin Kramer and Xiaochao Zheng. I would also like to recognize two colleagues that were unable to participate in the experiment: Jindong Zhou and Xiaofeng Zhu. The death of Jindong was unexpected and too soon. Xiaofeng was the unfortunate victim of INS and visa problems. I am happy that Xiaofeng was eventually able to come back after a few years.

Nilanga Liyanage was invaluable with his analysis help for the spectrometer optics. I am grateful for his patience with my unending questions and understanding. I am extremely grateful to Alexandre and Tim for many conversations both physics and life related. In the period leading up to my defense, both Karl and Rob were extremely supportive and understanding. I would like to thank them for their time and patience.

Wolfgang Korsch is a great person. I would like to thank him for taking me under his wing when I first came to JLab and teaching me the joys of C++ and ROOT. I would like to thank my fellow thesis students: Jaideep and Jing Yuan. Finally I will always be grateful for Hai-jiang Lu and his help with the PID analysis.

Finally this experiment would not have been successful without the support of the Hall A technical staff, designers and physics staff. The installation of the experiment would not have been possible without Ed Folts and his crew's continuous support. I am extremely grateful for having the opportunity to work with Al Gavalya, Joyce Miller and Susan Esp. They are a wonderful group to work with and I will always cherish the friendship I developed with them.

When I started my graduate life at William and Mary, my family and friends lived far away. I will always cherish the new friendships I found at William and Mary and Jefferson Lab. I would like to thank my friends for their support and encouragement: Josh Moss, Keoki Seu, Melanie Collins, Cherry Suewattana, Shannon Watson, Dandan Mao, Sarah Phillips, Chris and Gail Kulp, Lisa Kaufman, Kent Paschke, Ryan Snyder, Ameya Kolarkar, Kathy McCormick, Doug Higinbotham and Marcy Stutzman. I would also like to thank the lunch crew: Aidan Kelleher, Bryan Moffit, Joe Katich, Tim Holmstrom and Brian Hahn for the many great lunches we have shared.

I would like to thank the William and Mary secretarial staff. Without them I would never have gotten the paper work completed: Paula, Sylvia, Dianne and Carol.

Without my family, I would have never made it this far. My parents and sisters have been very supportive of my decisions and I am grateful to have them in my life. It wasn't easy for my parents to see me leave home and be so far away. I am thankfully they were supportive and understanding of my decision to come to William and Mary. My sisters, Anita and Sherry, have been wonderful. I am glad we have turned out to be such great friends. I am happy that they were able to see me graduate.

TABLE OF CONTENTS

Page

LIST OF TABLES

LIST OF FIGURES

THE SPIN STRUCTURE OF ^{3}He AND THE NEUTRON AT LOW Q^2: A MEASUREMENT OF THE GENERALIZED GDH INTEGRAND

CHAPTER 1

Introduction

The historical background of this thesis begins with the discovery of intrinsic spin by Stern and Gerlach in the 1920's. We consider the classical example of a rigid object that has two types of angular momentum: orbital and spin. The orbital angular momentum is related to motion of the center of mass about an external point and the spin with rotation around the object's center of mass. For a classical body such as a planet, the spin is associated with the planet's rotation about its polar axis. In the case of a particle such as an electron, there are analogous orbital and spin angular momenta. The orbital angular momentum is due to the electron's motion around the nucleus. Whereas the spin angular momentum S cannot be associated with rotation and is an intrinsic property of the particle, since as far as we know the electron is a point-like particle without structure.

A particle's spin is related to its magnetic moment by

$$\vec{\mu} = \frac{eQ}{M}\vec{S}\,, \tag{1.1}$$

where eQ and M are the particle's charge and mass, respectively. For a structureless

spin-$\frac{1}{2}$ particle, the magnetic moment was predicted by Dirac to be:

$$\mu = \frac{e}{2M}\hbar\,, \tag{1.2}$$

which agrees well, but not perfectly with the experimentally measured value for the electron. In 1933, Estermann and Stern measured the magnetic moment of the proton [1, 2] and discovered that the proton's magnetic moment was considerably different compared with Dirac's prediction. This was the first indication that the proton and neutron had composite structure and marked the beginning of hadronic physics, where hadrons are subatomic particles which interact via the strong force. The difference in the magnetic moment compared with Dirac's prediction is referred to as the anomalous part of the magnetic moment κ.

A couple of decades later, electron scattering experiments were used to confirm that the nucleon has a spatial distribution. Later on, an extensive study of the nucleon's structure [3] was performed using deep inelastic scattering experiments at the Stanford Linear Accelerator Center (SLAC). From these measurements, it was concluded that the nucleon is composed of point-like particles known as partons, which are now associated with quarks and gluons. Quantum Chromodynamics (QCD) has emerged as the theory that describes the strong interactions of quarks by the exchange of gluons. In the high energy region, predictions from perturbative QCD have been verified by comparison with experimental results. However, at low energies, QCD calculations become difficult due to the large coupling constant in this regime. Therefore low-energy effective field theories such as chiral perturbation theory have been utilized to make predictions.

A key remaining question is how the transition from partonic to hadronic degrees of freedom occurs. One way to approach this issue is to experimentally investigate the non-perturbative region. In the 1980's the nucleon's spin degrees of freedom were stud-

ied at SLAC and CERN [4]. The purpose of these measurements was to examine how the total nucleon spin is distributed among its constituents. The results gave rise to the "spin crisis"; only $\sim$ 30% of the nucleon's spin is carried by the quarks. The rest of the spin is expected to be carried by the gluons and orbital angular momentum of the nucleon's constituents. These studies have continued at CERN, DESY and Jefferson Lab. Measurements have been performed specifically at low and intermediate momentum transfers to study the non-perturbative regime at Jefferson Lab.

Experiment E97-110 has followed these measurements by providing precise data in the low energy region to test sum rule predictions from chiral perturbation theory. This thesis describes the theoretical formalism, experimental details, data analysis and preliminary results from this experiment.

CHAPTER 2

Inclusive Electron Scattering

Lepton scattering provides a powerful tool to probe the internal structure of the nucleon. Lepton interactions are well understood and described by the theory of Quantum Electrodynamics (QED). In this chapter, the process of inclusive electron-nucleon scattering, where only the scattered electron is detected, will be discussed. The relevant kinematic variables, the differential cross section, and the types of inclusive electron scattering are presented.

2.1 Kinematic Variables

The process of lepton-nucleon scattering is

$$l(p) + N(P) \rightarrow l(p') + X(P')\,, \tag{2.1}$$

in which a charged lepton l, in our case an electron, scatters from a nucleon N. In the Born approximation, the scattering occurs by the exchange of a virtual photon as shown in Fig. 2.1. The relevant kinematic variables are the incident and scattered electron four-

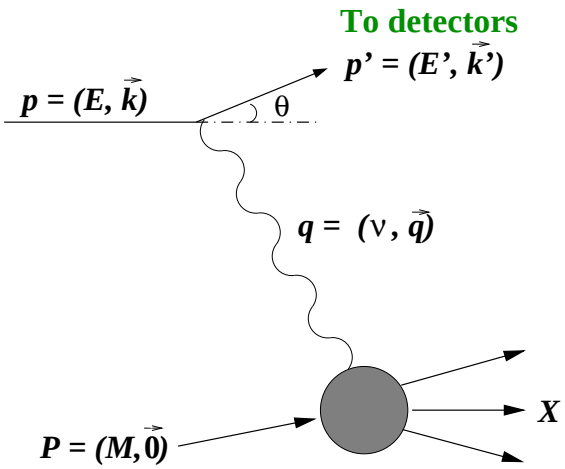

FIG. 2.1: Lowest order diagram for inclusive electron scattering.

momenta $p^\mu = (E, \vec{k})$ and $p'^\mu = (E', \vec{k'})$ respectively and the target four-momenta $P^\mu = (E_\mathrm{t}, \vec{P})$. The scattering angle is given by θ. For inclusive scattering, the final hadronic system X goes undetected. The exchanged virtual photon carries four-momentum $q^\mu = (p - p')^\mu = (\nu, \vec{q})$ and transfers an energy $\nu = \frac{P \cdot q}{M}$ and momentum $\vec{q}$ to the target.

The scattering process is a function of two Lorentz invariants and the scattering angle. Typically either the energy transfer, the squared four-momentum transfer Q^2 or the invariant mass of the residual hadronic system W are used. These variables are defined below with $P^\mu = (M, \vec{0})$ in the laboratory system. The electron mass is neglected, since E and $E' \gg m_\mathrm{e}$.

$$\nu = E - E' \tag{2.2}$$

$$Q^2 = -q^2 \simeq 4EE' \sin^2 \frac{\theta}{2} \tag{2.3}$$

$$W = \sqrt{(P+q)^2} = M^2 + 2M\nu - Q^2 \tag{2.4}$$

Two additional scalar invariants are sometimes used:

$$x = \frac{Q^2}{2P \cdot q} = \frac{Q^2}{2M\nu}\,, \tag{2.5}$$

the Bjorken scaling variable and

$$y = \frac{q \cdot P}{p \cdot P} = \frac{\nu}{E}\,, \tag{2.6}$$

the fraction of lepton energy loss.

2.2 Differential Cross Section and Structure Functions

The inclusive cross section for electron-nucleon scattering is proportional to the product of a leptonic and an hadronic tensor, $L_{\mu\nu}$ and $W^{\mu\nu}$, respectively:

$$\frac{d^2\sigma}{d\Omega dE'} = \frac{\alpha^2}{Q^4}\frac{E'}{E} L_{\mu\nu} W^{\mu\nu}\,, \tag{2.7}$$

where $\alpha \simeq 1/137$ is the electromagnetic fine structure constant. The formalism includes the possibility that both the electron and target are polarized.

The lepton tensor is calculable from QED:

$$L_{\mu\nu} = \sum_{s'} \bar{u}_s(p)\gamma_\mu u_{s'}(p')\bar{u}_{s'}(p')\gamma_\nu u_s(p) \tag{2.8}$$

$$= 2\left[p_\mu p'_\nu + p'_\mu p_\nu - g_{\mu\nu} p \cdot p' + i\epsilon_{\mu\nu\alpha\beta} s^\alpha q^\beta\right]\,, \tag{2.9}$$

where $u(p)$ are the Dirac spinors, $s_\mu = \bar{u}\gamma_\mu\gamma_5 u$ is the lepton spin vector, and the Levi-Civita tensor ϵ_{0123} = +1 uses the convention in [5].

In the inelastic process, one needs to consider all possible transitions of the nucleon from the ground state $|N(P)\rangle$ to any excited state $|X(P')\rangle$. In this case, the hadronic tensor becomes

$$W_{\mu\nu} = \frac{1}{4\pi M}\int d^4\zeta e^{iq\cdot\zeta}\langle N_s(P)|J_\mu(\zeta)J_\nu(0)|N_s(P)\rangle\,, \tag{2.10}$$

where ζ is the spatial four-vector, s is the target spin and $J_\mu(\zeta)$ is the electromagnetic current. In Eq. (2.10), completeness of the states $|X\rangle$ was used. The tensor can be further

split into symmetric and antisymmetric parts $W_{\mu\nu} = W^S_{\mu\nu} + W^A_{\mu\nu}$. The most general forms of these terms are obtained from Lorentz and gauge invariance and parity conservation of the electromagnetic interaction:

$$\begin{aligned} W^S_{\mu\nu} &= W_1(\nu, Q^2)\left(\frac{q_\mu q_\nu}{q^2} - g_{\mu\nu}\right) \\ &\quad + \frac{W_2(\nu, Q^2)}{M^2}\left(P_\mu - \frac{P\cdot q}{q^2}q_\mu\right)\left(P_\nu - \frac{P\cdot q}{q^2}q_\nu\right) \end{aligned} \tag{2.11}$$

and

$$W^A_{\mu\nu} = i\epsilon_{\mu\nu\alpha\beta}q^\alpha\left[G_1(\nu, Q^2)S^\beta + \frac{G_2(\nu, Q^2)}{M^2}\left(S^\beta P\cdot q - P^\beta S\cdot q\right)\right],$$

where the hadronic spin vector is given by $S^\mu = \bar{u}(P)\gamma^\mu\gamma_5 u(P)/2M$. The internal structure of the hadron is described by the four response functions: $W_{1,2}$ and $G_{1,2}$.

Usually the response functions are replaced with dimensionless structure functions that are dependent on the Bjorken variable x and Q^2:

$$F_1(x, Q^2) = MW_1(\nu, Q^2)\,, \tag{2.12}$$

$$F_2(x, Q^2) = \nu W_2(\nu, Q^2)\,, \tag{2.13}$$

$$g_1(x, Q^2) = M\nu G_1(\nu, Q^2)\,, \tag{2.14}$$

$$g_2(x, Q^2) = \nu^2 G_2(\nu, Q^2)\,. \tag{2.15}$$

The structure functions are measured experimentally by using different combinations of the beam and target polarizations. If one averages over the incident electron and target spins, then the differential cross section for unpolarized scattering in the lab frame is

$$\frac{d^2\sigma}{d\Omega dE'} = \left(\frac{d\sigma}{d\Omega}\right)_{\rm Mott}\left(\frac{2}{M}F_1(x, Q^2)\tan^2\frac{\theta}{2} + \frac{1}{\nu}F_2(x, Q^2)\right) \tag{2.16}$$

where the Mott cross section describes relativistic electron scattering from a point-like Dirac particle:

$$\left(\frac{d\sigma}{d\Omega}\right)_{\text{Mott}} = \frac{\alpha^2 \cos^2 \frac{\theta}{2}}{4E^2 \sin^4 \frac{\theta}{2}} \,. \tag{2.17}$$

The structure functions F_1 and F_2 parameterize information about the target's internal structure and cannot be separated using different beam and target polarization directions.

The spin-dependent structure functions g_1 and g_2 can be measured by using two different target spin orientations with respect to the electron beam polarization: longitudinal and perpendicular. In the former case, the electron has spin $\uparrow$ or $\downarrow$ either along or opposite to the beam direction, and the target spin $\Uparrow$ is along the direction of the electron's momentum. The cross section difference between the two spin states is

$$\Delta\sigma_{\parallel} = \frac{4\alpha^2}{M\nu Q^2}\frac{E'}{E}\left[(E + E'\cos\theta)\, g_1(x, Q^2) - 2Mx g_2(x, Q^2)\right] \,, \tag{2.18}$$

where

$$\Delta\sigma_{\parallel} = \frac{d^2\sigma^{\downarrow\Uparrow}}{d\Omega dE'} - \frac{d^2\sigma^{\uparrow\Uparrow}}{d\Omega dE'}. \tag{2.19}$$

For a transversely polarized target, $\Rightarrow$ denotes that the target spin is perpendicular (while in the scattering plane) to the electron beam direction. The polarized cross section difference for this process is

$$\Delta\sigma_{\perp} = \frac{4\alpha^2}{M\nu Q^2}\frac{E'^2}{E}\left[g_1(x, Q^2) + \frac{2E}{\nu} g_2(x, Q^2)\right] \sin\theta \,, \tag{2.20}$$

with

$$\Delta\sigma_{\perp} = \frac{d^2\sigma^{\downarrow\Rightarrow}}{d\Omega dE'} - \frac{d^2\sigma^{\uparrow\Rightarrow}}{d\Omega dE'}. \tag{2.21}$$

2.3 Types of Inclusive Electron Scattering

The inclusive differential cross sections described in Section 2.2 are rather general. When investigating inclusive scattering, separating the different kinematic regions is often

useful. In this section, three types of scattering are discussed: elastic, quasi-elastic and inelastic. The discussion on inelastic scattering includes both resonance production and deep inelastic scattering. Figure 2.2 from [6] shows a typical cross section spectrum for inclusive scattering from a light nuclear target. As Q^2 and ν vary, different nucleon resonances (Δ, N_1^* and N_2^*) are seen at specific invariant masses W. The mass of the nucleus and nucleon are given by M_T and M. If the target is a nucleon, then there is no quasi-elastic peak.

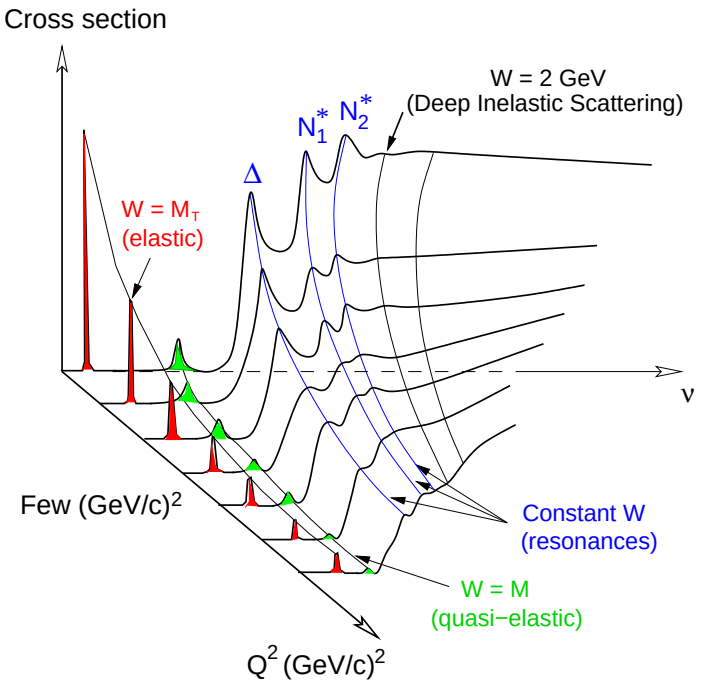

FIG. 2.2: Inclusive cross section (arbitrary units) versus Q^2 and ν for scattering off a nuclear target.

2.3.1 Elastic Scattering

In elastic scattering, the nucleon (or nucleus) remains in its ground state after the process, and the energy and momentum transfer are absorbed by the recoil nucleon. For elastic scattering, the invariant mass W is equal to the mass of the nucleon or nucleus so that $\nu = \frac{Q^2}{2M}$. Conservation of energy and momentum constrain the scattered electron energy to the following equation:

$$E' = \frac{E}{1 + \frac{2E}{M}\sin^2\frac{\theta}{2}}\,. \tag{2.22}$$

The differential cross section for unpolarized elastic scattering is a special case of Eq. 2.16. In the elastic scattering limit, the response functions $W_{1,2}$ reduce to combinations of the Sachs form factors [5]:

$$W_1 = \frac{Q^2}{4M^2}G_M^2(Q^2)\,, \tag{2.23}$$

and

$$W_2 = \frac{G_E^2(Q^2) + \frac{Q^2}{4M^2}G_M^2(Q^2)}{1 + \frac{Q^2}{4M^2}}\,. \tag{2.24}$$

Then Eq. 2.16 can be expressed as the Rosenbluth cross section [7] in terms of the electric and magnetic form factors G_E and G_M, respectively:

$$\frac{d\sigma}{d\Omega} = \left(\frac{d\sigma}{d\Omega}\right)_{\text{Mott}}\left(\frac{G_E^2(Q^2) + \frac{Q^2}{4M^2}G_M^2(Q^2)}{1 + \frac{Q^2}{4M^2}} + \frac{Q^2}{2M^2}G_M^2(Q^2)\tan^2\frac{\theta}{2}\right)\,. \tag{2.25}$$

The two form factors carry information on the charge and current distributions of the nucleon and are normalized at Q^2 = 0 to the nucleon charges and magnetic moments:

$$G_E^p(0) = 1 \quad \text{and} \quad G_M^p(0) = \mu_p = 2.793\,, \tag{2.26}$$

for the proton and:

$$G_E^n(0) = 0 \quad \text{and} \quad G_M^n(0) = \mu_n = -1.913\,, \tag{2.27}$$

for the neutron. The magnetic moments are given in terms of the nuclear magneton $\mu_N = \frac{e}{2M_p}$.

The behavior of the proton and neutron magnetic form factors follow a dipole form over a sizable range of Q^2, with deviations less than 10% for G_M^p at $Q^2 \leq 5$ GeV^2. The dipole parameterization is as follows:

$$G_D(Q^2) = \left(\frac{\Lambda^2}{\Lambda^2 + Q^2}\right)^2 , \tag{2.28}$$

where Λ = 0.84 GeV, so that

$$\frac{G_M^p(Q^2)}{\mu_p} = \frac{G_M^n(Q^2)}{\mu_n} = G_D(Q^2) . \tag{2.29}$$

The proton electric form factor follows the same dipole fit but only for $Q^2 \leq 1$ GeV^2. At higher Q^2 significant differences are seen between the proton electric and magnetic form factors [8, 9]. The transition between the low and high Q^2 regions provides information on the non-perturbative structure of the nucleon and where the onset of perturbative behavior begins.

2.3.2 Quasi-Elastic Scattering

For a nuclear target, quasi-elastic scattering involves the incident electron elastically scattering from one of the nucleons within the nucleus. In this process, the nucleon is knocked out of the nucleus and can be considered initially as quasi-free. Compared to elastic scattering from a free nucleon, the quasi-elastic peak is shifted and broadened due to the nuclear binding energy and Fermi motion of the nucleons inside the nucleus.

For quasi-elastic scattering, the Rosenbluth cross section [10] becomes

$$\frac{d^2\sigma}{d\Omega dE'} = \left(\frac{d\sigma}{d\Omega}\right)_{\text{Mott}} \left\{ \left(\frac{Q^2}{\vec{q}^2}\right)^2 R_L + \left[\frac{1}{2}\left(\frac{Q^2}{\vec{q}^2}\right)^2 + \tan^2\frac{\theta}{2}\right] R_T \right\} , \tag{2.30}$$

where $R_L(\nu, Q^2)$ and $R_T(\nu, Q^2)$ are the longitudinal and transverse virtual photon response functions.

2.3.3 Resonances

As the energy transfer increases, we leave the elastic region and enter the process of inelastic scattering. Inelastic scattering from nucleons has revealed a rich spectrum of excited states known as the resonances. The existence of these states was further evidence that the nucleon is a composite system. The resonances have been observed in the invariant mass region between the pion production threshold ($W_\pi = M_p + m_\pi$) 1.072 GeV and the onset of deep inelastic scattering at 2 GeV. Their properties have been studied using beams of leptons, photons and hadrons.

Beyond the elastic peak, we typically see three significant resonance features; the first peak is the $\Delta(1232)$ resonance, the second peak consists of the $N^*(1520)$ and $N^*(1535)$ resonances and the third peak contains many resonances with the $N^*(1680)$ being the strongest at low Q^2. The $N^*(1440)$ resonance also exists between the Δ and the second maximum. The Δ is a dominant spin-$\frac{3}{2}$ resonance in π-N scattering and has only a small amount of overlap with other states. Table 2.1 summarizes some of the properties of these resonances: invariant mass, width (Γ), total angular momentum and parity (J^p) and the orbital angular momentum (l). The total angular momentum is given by $J = \left|l \pm \frac{1}{2}\right|$. The nomenclature used to denote the resonances is given by L_{2I2J} :

- L = S (for l = 0), P (for l = 1), D (for l = 2), F (for l = 3).
- I is the isospin, either $\frac{1}{2}$ or $\frac{3}{2}$.

Using this notation the Δ is expressed as P_{33}. Several other resonances exist that contribute to the cross section; however, these resonances cannot be isolated with inclusive

electron scattering.

Resonance	W (MeV)	Γ (MeV)	J^p	l
P_{33}	1232	120	$\frac{3}{2}^+$	1
P_{11}	1440	350	$\frac{1}{2}^+$	1
D_{13}	1520	120	$\frac{3}{2}^-$	2
S_{11}	1535	150	$\frac{1}{2}^-$	0
F_{15}	1680	130	$\frac{5}{2}^+$	3

TABLE 2.1: Nucleon resonance properties. Reproduced from [5].

2.3.4 Deep Inelastic Scattering

The deep inelastic scattering (DIS) regime is typically defined as $Q^2 >$ 1-2 GeV^2 and $W >$ 2 GeV. In this region, the resonance peaks become indistinguishable and the scattering process occurs from an incoherent sum over the nucleon's constituents. The phenomenon known as scaling was discovered at the Stanford Linear Accelerator; at large momentum transfers, the structure functions are independent of Q^2 and essentially "only" depend on the dimensionless variable $x = Q^2/2M\nu$. Figure 2.3 shows the experimental Q^2-variation of the proton $F_2^p(x, Q^2)$ structure function for a large range of x [11]. For plotting purposes, a constant[1] $c(x) = 0.6(i_x - 0.4)$ is added to F_2^p.

Scaling of the structure functions was predicted by Bjorken [12], and the parton model of Feynman [13] provides a clear explanation for this phenomenon. Any particle with a finite size must have a form factor that introduces some Q^2 dependence. The fact that the structure functions are independent of the momentum transfer implies that the nucleon contains point-like objects, which Feynman named partons. The partons are now

[1] i_x is the number of the x bin ranging from i_x = 1 (x = 0.32) to i_x = 21 (x = 0.000032).

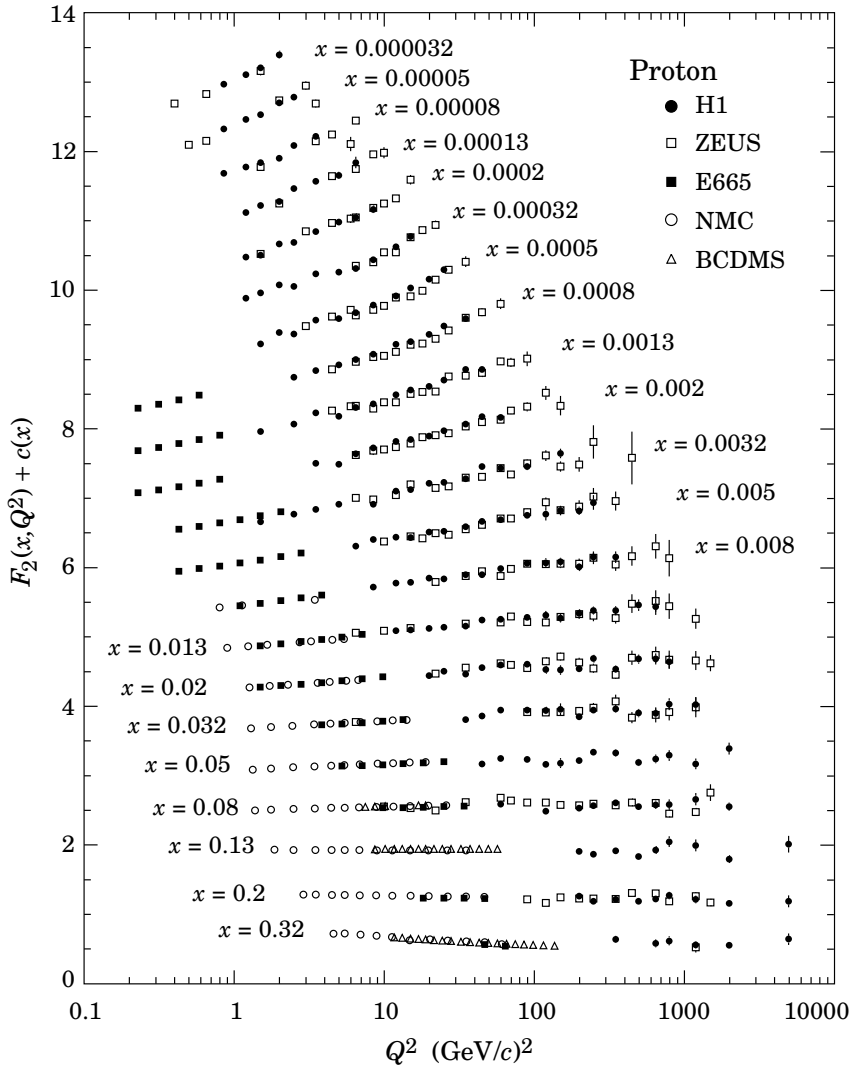

FIG. 2.3: The F_2^p structure function Q^2-dependence for a range of Bjorken x values. Reproduced from [11].

identified as the quarks and gluons of QCD. The parton model is typically formulated in the infinite momentum frame, where ν and Q^2 go to infinity while x remains finite. The scattering process can be treated using the impulse approximation (IA), since there is no time for interactions to occur between the partons. Hence, the DIS process can be viewed as the incoherent sum of elastic scattering from non-interacting partons.

In the parton model, the fraction of the nucleon's momentum carried by the struck quark can be associated with Bjorken's scaling variable x [5]. The nucleon cross section then becomes the sum of the cross sections for scattering from individual partons; the cross sections are then weighted by their respective number densities. Since the scattering process occurs through the electromagnetic interaction, the cross sections are additionally weighted by the parton's charge squared. The structure functions then take the form:

$$F_1(x) = \frac{1}{2}\sum_f e_f^2 q_f(x) = \frac{1}{2}\sum_f e_f^2 \left[q_f^{\uparrow}(x) + q_f^{\downarrow}(x)\right] \tag{2.31}$$

$$F_2(x) = 2xF_1(x) \tag{2.32}$$

$$g_1(x) = \frac{1}{2}\sum_f e_f^2 \Delta q_f(x) = \frac{1}{2}\sum_f e_f^2 \left[q_f^{\uparrow}(x) - q_f^{\downarrow}(x)\right] \ , \tag{2.33}$$

where $q_f(x)$ and $\Delta q_f(x)$ are the unpolarized and polarized parton distribution functions with parton flavor f. The distribution functions involve the two cases where the quark spin is aligned parallel ($\uparrow$) or anti-parallel ($\downarrow$) to the nucleon spin. Eq. (2.32) is known as the Callan-Gross relation [14]. There is no simple interpretation of g_2 in the parton model, but it carries information about the quark-gluon interactions that occur inside the nucleon.

Bjorken scaling is only an approximation, since quarks can radiate gluons before and after the scattering process. These processes cannot be separated from electron scattering off a quark without gluon radiation. This causes the structure functions to develop a logarithmic dependence on Q^2, and hence, Bjorken scaling is only a "a good approximation".

This variation of the structure functions with the momentum transfer squared is referred to as QCD evolution. The DGLAP equations developed by Dokshitzer [15], Gribov, Lipatov [16], Altarelli and Parisi [17] provide a method to calculate the Q^2-evolution of the parton distributions. Once the parton distributions are know at one scale, they can be calculated at any other scale where perturbative QCD is applicable.

CHAPTER 3

Sum Rules

In Chapter 2, we have seen that the internal structure of the nucleon is parameterized by structure functions; however, the available theoretical tools are unable to calculate the structure functions. Instead, these tools are used to provide predictions of the moments of the structure functions. In addition to the moments, there are several dispersive sum rules that link the Compton scattering amplitudes to integrals of the inclusive photoproduction cross sections of the target under investigation. These sum rules are based on universal principles such as causality, unitarity and gauge invariance. The interest in sum rules lies in the fact that they provide a useful testing ground to study the internal degrees of freedom of the system. The extension from real to virtual photons provides a probe with variable resolution. At small Q^2, the long range phenomena are sampled and described by effective degrees of freedom (hadrons), whereas at large Q^2, the primary degrees of freedom (quarks and gluons) become visible.

The first part of this chapter provides an overview of the formalism of virtual photoabsorption cross sections. In the second part, we derive an important spin sum rule

known as the GDH sum rule. In the third part, the GDH sum rule is generalized for virtual photons along with a few other Q^2-dependent sum rules that are relevant for experiment E97-110.

3.1 Virtual Photoabsorption Cross Sections

In Section 2.2, we have seen that the inclusive differential cross section can be described in terms of four structure functions. The cross section can also be written equivalently as a cross section for the absorption of a virtual photon, which involves four partial cross sections [18, 19]:

$$\frac{d^2\sigma}{d\Omega dE'} = \Gamma \left[\sigma_T + \epsilon\sigma_L - hP_x\sqrt{2\epsilon(1-\epsilon)}\sigma_{LT} - hP_z\sqrt{1-\epsilon^2}\sigma_{TT}\right] , \tag{3.1}$$

where ϵ and Γ are the ratio of the longitudinal to transverse polarization of the virtual photon and the virtual photon flux factor given by Eq. (3.2) and Eq. (3.3):

$$\epsilon = \left[1 + 2\left(1 + \frac{\nu^2}{Q^2}\right)\tan^2\frac{\theta}{2}\right]^{-1} \tag{3.2}$$

and

$$\Gamma = \frac{\alpha}{2\pi^2 Q^2}\frac{E'}{E}\frac{K}{1-\epsilon} . \tag{3.3}$$

The flux factor Γ is proportional to the virtual photon flux K, which is convention dependent. A few of the common conventions follow below:

$$K_{\rm A} = \nu \tag{3.4}$$

$$K_{\rm H} = \frac{W^2 - M^2}{2M} = \nu(1-x) \tag{3.5}$$

$$K_{\rm G} = |\vec{q}| = \sqrt{\nu^2 + Q^2} . \tag{3.6}$$

The first convention connects the flux to the virtual photon energy ν [10]. The second convention is Hand's convention [20] and associates the flux with the "equivalent photon energy". The third convention by Gilman [21] uses the photon momentum in the lab frame. At the real photon point, all the conventions reduce to ν, but at intermediate Q^2, the photon flux is strongly convention dependent.

The four partial cross sections consists of the longitudinal (σ_L), transverse (σ_T) and two interference terms: longitudinal-transverse (σ_{LT}) and transverse-transverse (σ_{TT}) and are functions of ν and Q^2. The two interference terms involve a spin-flip and can only be measured by double-polarization experiments. The longitudinal and transverse terms involve the absorption of a longitudinal and transverse virtual photon on a nucleon respectively. In the real photon limit (Q^2 = 0), σ_L vanishes and the total photoabsorption cross section is given by $\sigma(\nu) = \sigma_T(\nu)$. In Eq. (3.1), $h = \pm 1$ refers to the helicity of the longitudinally polarized electron, and P_z (P_x) denote that the target polarization is parallel (perpendicular) to the virtual photon momentum $\vec{q}$. The helicity is defined as:

$$h = \frac{\vec{\sigma} \cdot \vec{p}}{|\vec{p}|}\,, \tag{3.7}$$

where $\vec{\sigma}$ are the Pauli spin matrices, and $\vec{p}$ is the particle's momentum.

The partial cross sections σ_T and σ_{TT} can be expressed in terms of the helicity-dependent photoabsorption cross sections $\sigma_{\frac{1}{2}}$ and $\sigma_{\frac{3}{2}}$. The subscripts refer to the total helicity projections of the photon plus target helicities. The projections are illustrated in Fig. 3.1 for a spin-$\frac{1}{2}$ target. These helicity cross sections are related to the transverse (spin-averaged) and transverse-transverse (spin-dependent) interference terms via the following expressions:

$$2\sigma_T = \sigma_{\frac{1}{2}} + \sigma_{\frac{3}{2}}, \quad 2\sigma_{TT} = \sigma_{\frac{1}{2}} - \sigma_{\frac{3}{2}}\,. \tag{3.8}$$

The virtual photoabsorption cross sections are also related to the structure functions

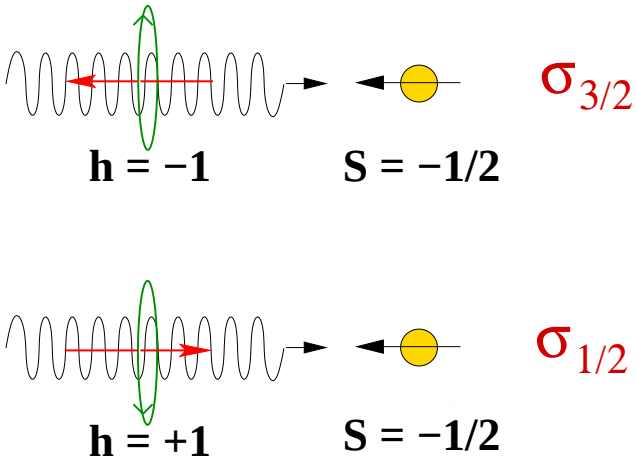

FIG. 3.1: Schematic of the helicity-dependent cross sections $\sigma_{\frac{1}{2}}$ and $\sigma_{\frac{3}{2}}$. The virtual photon helicity and target spin projections are denoted by h and S respectively

F_1, F_2, g_1 and g_2, which are dependent on ν and Q^2:

$$\sigma_T = \frac{4\pi^2\alpha}{MK} F_1 \tag{3.9}$$

$$\sigma_L = \frac{4\pi^2\alpha}{K}\left[\frac{F_2}{\nu}\left(1+\gamma^2\right) - \frac{F_1}{M}\right] \tag{3.10}$$

$$\sigma_{LT} = \frac{4\pi^2\alpha}{MK}\gamma\left(g_1 + g_2\right) \tag{3.11}$$

$$\sigma_{TT} = \frac{4\pi^2\alpha}{MK}\left(g_1 - \gamma^2 g_2\right)\ , \tag{3.12}$$

where $\gamma = Q/\nu$, and the correspondence is dependent on the virtual photon flux K. The interference terms can also be defined as $\sigma_{LT(TT)} = -\sigma'_{LT(TT)}$.

3.2 The GDH Sum Rule

The Gerasimov-Drell-Hearn (GDH) Sum Rule [22–25] relates a particle's anomalous magnetic moment κ to an energy-weighted integral over its photoabsorption cross

section. The sum rule's significance is that it relates static properties of the particle's ground state to dynamic properties of all its excited states. It also divulges that a non-zero anomalous magnetic moment requires that a particle have a finite size and hence an excitation spectrum [19]. Consequently, the discovery that the nucleon had a large anomalous magnetic moment provided a strong indication that the nucleon has an intrinsic structure and is not a point-like particle. The sum rule for spin-$\frac{1}{2}$ particles is

$$\int_{\nu_0}^{\infty} \frac{d\nu}{\nu} \left[\sigma_{\frac{1}{2}}(\nu) - \sigma_{\frac{3}{2}}(\nu) \right] = -2\pi^2 \alpha \frac{\kappa^2}{M^2} \,, \tag{3.13}$$

where $\nu_0 = m_\pi \left(1 + \frac{m_\pi}{2M}\right) \approx 150$ MeV is the threshold energy for pion production. This sum rule provides an ideal testing ground to study the nucleon's internal structure, since the right hand side is given by the nucleon's ground state properties that are known rather precisely. In addition, the sum rule was generalized for virtual photoabsorption on a nucleon, which allows us to study the Q^2-evolution and hence the spatial distribution of the spin observables. The following discussion provides a derivation of the GDH sum rule based on dispersion relations, which follows Refs. [23] and [24].

3.2.1 Derivation of the GDH Sum Rule

The general assumptions used in the derivation of the sum rule are Lorentz and gauge invariance, unitarity and causality. We begin with the forward Compton amplitude $T(\nu, \theta = 0)$ for real photon scattering from a nucleon:

$$T(\nu) = \vec{\varepsilon}'^{*} \cdot \vec{\varepsilon} f(\nu) + i\vec{\sigma} \cdot (\vec{\varepsilon}'^{*} \times \vec{\varepsilon})\, g(\nu) \,, \tag{3.14}$$

where $\vec{\varepsilon}$ and $\vec{\varepsilon}'^{*}$ are the incident photon and outgoing photon polarization vectors respectively. Crossing symmetry requires that the T-matrix is symmetric under exchange of incoming and outgoing photons, $\vec{\varepsilon}'^{*} \leftrightarrow \vec{\varepsilon}$ and $\nu \rightarrow -\nu$, which implies that f is an even

function and g is an odd function of ν. The amplitudes can be separately determined by using circularly polarized photons incident on a nucleon that is polarized either parallel or anti-parallel with respect to the photon momentum $\vec{q}$. The polarization vectors can take the following form for a photon moving along the z-axis:

$$\varepsilon_{\pm} = \mp\frac{1}{\sqrt{2}}\left(\hat{e}_x \pm i\hat{e}_y\right) , \tag{3.15}$$

which corresponds to right-handed (+1) and left-handed (-1) circularly polarized light. For the above description the transverse gauge ($\varepsilon \cdot q$ = 0) was used with the photon four-momentum and polarization defined as $q = (\nu, \vec{q})$ and $\varepsilon = (0, \vec{\varepsilon})$ with $q \cdot q$ = 0.

Unitarity of the scattering matrix relates the imaginary part of the amplitudes to the photoabsorption cross sections by the optical theorem:

$$\mathrm{Im}\, f(\nu) = \frac{\nu}{8\pi}\left(\sigma_{\frac{1}{2}}(\nu) + \sigma_{\frac{3}{2}}(\nu)\right) = \frac{\nu}{4\pi}\sigma_T \tag{3.16}$$

and

$$\mathrm{Im}\, g(\nu) = \frac{\nu}{8\pi}\left(\sigma_{\frac{1}{2}}(\nu) - \sigma_{\frac{3}{2}}(\nu)\right) = \frac{\nu}{4\pi}\sigma_{TT}\,. \tag{3.17}$$

The helicity-dependent cross sections were defined in Section 3.1.

At small photon energies, the amplitudes can be expanded in powers of ν, and the low energy theorem (LET), of Low [26] and Gell-Mann & Goldberger [27], based on Lorentz and gauge invariance gives the leading order terms:

$$f(\nu) = -\frac{Z^2e^2}{4\pi M} + (\alpha+\beta)\nu^2 + O(\nu^4)\,, \tag{3.18}$$

$$g(\nu) = -\frac{e^2\kappa^2}{8\pi M^2}\nu + \gamma_0\nu^3 + O(\nu^5)\,, \tag{3.19}$$

where Z is the target's charge (1 for the proton and 0 for the neutron). The leading term $f(0)$ is the classical Thomson scattering result. The $O(\nu^2)$ term describes Rayleigh scattering and introduces the electric (α) and magnetic (β) dipole polarizabilities. For the

spin-flip amplitude g, the leading term is associated with κ, the anomalous magnetic moment, and the $O(\nu^3)$ term is related to the forward spin polarizability γ_0, which contains information on the spin structure.

The final piece needed to form the sum rule is a dispersion relation. Dispersion relations can be derived for $f(\nu)$ and $g(\nu)$ by using the analytic properties of the forward Compton scattering amplitudes with unitarity and crossing symmetry. The dispersion relation for the spin-averaged amplitude f is the Kramers-Kronig relation from optics, which connects the real part of f with an integral over the imaginary part of f:

$$\mathrm{Re}\, f(\nu) = \frac{2}{\pi} P \int_{\nu_0}^{\infty} d\nu' \nu' \frac{\mathrm{Im}\, f(\nu')}{\nu'^2 - \nu^2}\,. \tag{3.20}$$

With the optical theorem, the imaginary part is replaced by the total cross section so the dispersion relation becomes

$$\mathrm{Re}\, f(\nu) = f(0) + \frac{\nu^2}{2\pi^2} P \int_{\nu_0}^{\infty} d\nu' \frac{\sigma_T(\nu')}{\nu'^2 - \nu^2}\,, \tag{3.21}$$

where P denotes the principal value integral. Since the total cross section has a slow logarithmic increase beyond the resonance region, a subtraction is made at $\nu = 0$ to ensure that the integral converges. The term $f(0)$ is the Thomson limit that was encountered in the LET above.

Applying the same general principles, an unsubtracted dispersion relation can be derived for the spin-flip amplitude:

$$\mathrm{Re}\, g(\nu) = \frac{\nu}{4\pi^2} P \int_{\nu_0}^{\infty} \nu' d\nu' \frac{\sigma_{\frac{1}{2}}(\nu') - \sigma_{\frac{3}{2}}(\nu')}{\nu'^2 - \nu^2}\,, \tag{3.22}$$

where the optical theorem was used to replace the imaginary part of g with the helicity-dependent cross section difference. In this relation, it is assumed that the cross section difference decreases fast enough at large ν' so that the integral converges without a subtraction. This assumption is called the non-subtraction hypothesis.

Using the result from the LET from Eq. (3.19) and Eq. (3.22), we can now form the GDH integral by comparing the $O(\nu)$ terms such that

$$I \equiv -\frac{\alpha}{2M^2}\kappa^2 = \frac{1}{4\pi^2}\int_{\nu_0}^{\infty}\frac{d\nu}{\nu}\left[\sigma_{\frac{1}{2}}(\nu) - \sigma_{\frac{3}{2}}(\nu)\right] . \tag{3.23}$$

where α = $e^2/4\pi$. Sum rules have also been formed for the electric and magnetic polarizabilities and the forward spin polarizability. These will not be discussed further in this document. More information on these sum rules is available in Refs. [5] and [19].

3.2.2 GDH Sum Rule Measurements

The GDH sum rule given by Eq. (3.23) connects a non-zero anomalous magnetic moment to the excitation spectrum of the target being investigated. This in turn provides a link to the target's internal degrees of freedom, which we are attempting to understand in the context of QCD. We expect that the low energy region including the lower mass resonances must have a significant contribution to the sum rule because of the ν^{-1} weighting. Table 3.1 provides, for selected targets, the anomalous magnetic moment, the GDH sum rule values for the right hand side $I_{\rm RHS}$ and the measured values for the left hand side $I_{\rm LHS}$ of Eq. (3.24). All the targets listed except the deuteron have spin = $\frac{1}{2}$. The sum rule

Target	κ (μ_N)	$I_{\rm RHS}$ (μb)	$I_{\rm LHS}$ (μb)
Proton	1.793	-204.8	–211 $\pm$ 15
Neutron	-1.916	-233.2	
Deuteron	-0.143	-0.65	–440 $\pm$ 21(stat) $\pm$ 25(syst)
^{3}He	-8.371	-497.9	

TABLE 3.1: Anomalous magnetic moments and GDH sum rule values for select targets. The anomalous moments are given in units of the nuclear magneton, $\mu_N = e/2M_p$.

can be generalized for a target of spin-S. In this case, the GDH sum rule becomes

$$\int_{\nu_0}^{\infty} \frac{d\nu}{\nu} \left[\sigma_P(\nu) - \sigma_A(\nu)\right] = -4\pi^2 \alpha S \frac{\kappa^2}{M^2}\,, \tag{3.24}$$

where the helicity-dependent cross sections σ_P and σ_A are for the photon helicity parallel or anti-parallel to the target spin. For nuclear targets, the energy threshold begins at the photo-disintegration threshold, 2.2 MeV and 5.5 MeV for the deuteron and ^{3}He nucleus respectively [10].

Measurements have been conducted for the proton and neutron GDH sum rules. The first proton measurement was performed at MAMI (Mainz) [28] for photon energies between 200 MeV and 800 MeV. The GDH Collaboration extended the measurement up to 2.9 GeV at ELSA (Bonn) [29]. With the two sets of data combined and an estimate for the unmeasured regions, the proton sum rule was found to be –211 $\pm$ 15 μb [19] implying that the sum rule is valid for the proton. Results on the deuteron GDH sum rule are available between 200 MeV and 1800 MeV from MAMI and ELSA [30, 31] with a value of –440 $\pm$ 21(stat) $\pm$ 25(syst) μb. For the deuteron sum rule to hold, these measurements indicate that the contribution from photo-disintegration has to be significantly large to cancel the resonance contributions. The neutron sum rule can be evaluated from the measured proton and deuteron results; however, the neutron extraction has yet to be performed. The region between the breakup threshold to pion production will be measured at the High Intensity Gamma Source (HIγS) [32]. There are other measurements planned, which are discussed in Ref. [19].

3.3 Dispersive Sum Rules for all Q^2

Using the framework developed in Section 3.1, we will now discuss the generalization of the GDH sum rule for virtual photons. In addition to the GDH sum rule, other important spin sum rules will be discussed. The extension of the sum rule was originally proposed to investigate the "spin crisis" of the 1980's by Anselmino et. al. [33]. The spin crisis was later resolved by taking into account the gluon spin, the sea quarks (q-$\bar{q}$ pairs) and the angular momentum of the partons. Various methods have been proposed to generalize the sum rule [34, 35], and we have chosen to follow the generalization discussed in Refs. [19] and [36].

In addition to the transverse polarization vectors $\vec{\varepsilon}_{\pm}$, the virtual photon has a third polarization vector $\vec{\varepsilon}_0$. The polarization four-vector can be defined as

$$\varepsilon_0 = \frac{1}{Q}\left(|\vec{q}|, 0, 0, q_0\right) , \tag{3.25}$$

where the z-axis was chosen to be in the direction of the photon propagation,

$$q = \left(q_0, 0, 0, |\vec{q}|\right) . \tag{3.26}$$

The three polarization vectors and the photon momentum are orthogonal in the Lorentz metrics. The forward Compton amplitude of Eq. (3.14) is then generalized for doubly-virtual Compton scattering (VVCS) by adding the longitudinal polarization vector $\hat{q}$:

$$\begin{aligned} T(\nu, Q^2) \;\; &= \;\; \vec{\varepsilon}'^{*} \cdot \vec{\varepsilon} f_T(\nu, Q^2) + f_L(\nu, Q^2) + i\vec{\sigma} \cdot (\vec{\varepsilon}'^{*} \times \vec{\varepsilon})\, g_{TT}(\nu, Q^2) \\ &\quad + i\,(\vec{\varepsilon}'^{*} - \vec{\varepsilon}) \cdot (\vec{\sigma} \times \hat{q})\, g_{LT}(\nu, Q^2) . \end{aligned} \tag{3.27}$$

For the following, we are only interested in the spin-flip amplitudes g_{TT} and g_{LT}. Alternatively the spin-flip amplitudes can be cast into a covariant form involving the am-

plitudes $S_1(\nu, Q^2)$ and $S_2(\nu, Q^2)$:

$$\begin{aligned} S_1(\nu, Q^2) &= \frac{\nu M}{\nu^2 + Q^2}\left[g_{TT}(\nu, Q^2) + \frac{Q}{\nu} g_{LT}(\nu, Q^2)\right] \\ S_2(\nu, Q^2) &= -\frac{M^2}{\nu^2 + Q^2}\left[g_{TT}(\nu, Q^2) - \frac{\nu}{Q} g_{LT}(\nu, Q^2)\right] . \end{aligned} \tag{3.28}$$

Under the crossing transformation, the VVCS amplitude has to be symmetric, which leads to the following properties:

$$S_1(\nu, Q^2) = S_1(-\nu, Q^2), \quad S_2(\nu, Q^2) = -S_2(-\nu, Q^2)\,, \tag{3.29}$$

$$g_{TT}(\nu, Q^2) = -g_{TT}(-\nu, Q^2), \quad g_{LT}(\nu, Q^2) = g_{LT}(-\nu, Q^2)\,. \tag{3.30}$$

The inelastic contributions can be related to the inclusive electroproduction cross sections via the optical theorem:

$$\begin{aligned} \mathrm{Im}\; g_{TT}(\nu, Q^2) &= \frac{K(\nu, Q^2)}{4\pi}\sigma_{TT}(\nu, Q^2)\,, \\ \mathrm{Im}\; g_{LT}(\nu, Q^2) &= \frac{K(\nu, Q^2)}{4\pi}\sigma_{LT}(\nu, Q^2)\,. \end{aligned} \tag{3.31}$$

Then the imaginary parts of the covariant spin amplitudes follow from Eqs. (3.28) and Eqs. (3.31) so that

$$\begin{aligned} \mathrm{Im}\; S_1(\nu, Q^2) &= \frac{\nu M}{\nu^2 + Q^2}\frac{K(\nu, Q^2)}{4\pi}\left[\sigma_{TT}(\nu, Q^2) + \frac{Q}{\nu}\sigma_{LT}(\nu, Q^2)\right] , \\ \mathrm{Im}\; S_2(\nu, Q^2) &= -\frac{M^2}{\nu^2 + Q^2}\frac{K(\nu, Q^2)}{4\pi}\left[\sigma_{TT}(\nu, Q^2) - \frac{\nu}{Q}\sigma_{LT}(\nu, Q^2)\right] . \end{aligned} \tag{3.32}$$

Consider the spin-dependent amplitude g_{TT}; assuming it has an appropriate convergence at high energy, we obtain the following unsubtracted dispersion relation:

$$\mathrm{Re}\,\left[g_{TT}(\nu, Q^2) - g_{TT}^{\mathrm{pole}}(\nu, Q^2)\right] = \frac{\nu}{2\pi^2} P \int_{\nu_0}^{\infty} \frac{K(\nu', Q^2)\sigma_{TT}(\nu', Q^2)}{\nu'^2 - \nu^2} d\nu'\,, \tag{3.33}$$

where the elastic contribution $g_{TT}^{\rm pole}$ was separated from the inelastic contribution $\nu' > \nu_0$. A low energy expansion can then be used

$$\mathrm{Re}\,\left[g_{TT}(\nu,Q^2) - g_{TT}^{\rm pole}(\nu,Q^2)\right] = \frac{2\alpha}{M^2} I_{TT}(Q^2)\nu + \gamma_{TT}(Q^2)\nu^3 + O(\nu^5)\,, \qquad (3.34)$$

that yields a generalization of the GDH sum rule for the leading term,

$$\begin{aligned} I_{TT}(Q^2) &= \frac{M^2}{4\pi^2\alpha}\int_{\nu_0}^{\infty}\frac{K(\nu,Q^2)}{\nu}\frac{\sigma_{TT}(\nu,Q^2)}{\nu}d\nu\,, \\ &= \frac{2M^2}{Q^2}\int_0^{x_0}\left[g_1(x,Q^2) - \frac{4M^2}{Q^2}x^2 g_2(x,Q^2)\right]dx\,, \end{aligned} \qquad (3.35)$$

and the second term leads to a generalized form of the forward spin polarizability ,

$$\begin{aligned} \gamma_{TT}(Q^2) &= \frac{1}{2\pi^2}\int_{\nu_0}^{\infty}\frac{K(\nu,Q^2)}{\nu}\frac{\sigma_{TT}(\nu,Q^2)}{\nu^3}d\nu\,, \\ &= \frac{16\alpha M^2}{Q^6}\int_0^{x_0} x^2\left[g_1(x,Q^2) - \frac{4M^2}{Q^2}x^2 g_2(x,Q^2)\right]dx\,, \end{aligned} \qquad (3.36)$$

where x is the Bjorken scaling variable and $x_0 = \frac{Q^2}{2M\nu_0}$ corresponds to the pion production threshold. In the real photon limit ($Q^2 \to 0$), $I_{TT}(0) = -\frac{1}{4}\kappa^2$ and $\gamma_{TT}(0) = \gamma_0$, i.e., the real photon sum rules are recovered for GDH and the forward spin polarizability.

With the same assumptions, we can construct an unsubtracted dispersion relation for the amplitude g_{LT}:

$$\mathrm{Re}\,\left[g_{LT}(\nu,Q^2) - g_{LT}^{\rm pole}(\nu,Q^2)\right] = \frac{2\alpha}{M^2} Q I_{LT}(Q^2) + Q\delta_{LT}(Q^2)\nu^2 + O(\nu^4)\,. \qquad (3.37)$$

The leading term results in a sum rule for $I_{LT}(Q^2)$:

$$\begin{aligned} I_{LT}(Q^2) &= \frac{M^2}{4\pi^2\alpha}\int_{\nu_0}^{\infty}\frac{K(\nu,Q^2)}{\nu}\frac{\sigma_{LT}(\nu,Q^2)}{Q}d\nu\,, \\ &= \frac{2M^2}{Q^2}\int_0^{x_0}\left[g_1(x,Q^2) + g_2(x,Q^2)\right]dx\,. \end{aligned} \qquad (3.38)$$

The $O(\nu^2)$ term gives the generalized longitudinal-transverse polarizability:

$$\begin{aligned}\delta_{LT}(Q^2) &= \frac{1}{2\pi^2}\int_{\nu_0}^{\infty}\frac{K(\nu,Q^2)}{\nu}\frac{\sigma_{LT}(\nu,Q^2)}{Q\nu^2}d\nu\,,\\ &= \frac{16\alpha M^2}{Q^6}\int_0^{x_0}x^2\left[g_1(x,Q^2)+g_2(x,Q^2)\right]dx\,. \end{aligned} \tag{3.39}$$

We can also construct unsubtracted dispersion relations for the covariant amplitudes S_1 and S_2:

$$\mathrm{Re}\,\left[S_1(\nu,Q^2)-S_1^{\mathrm{pole}}(\nu,Q^2)\right]=\frac{2\alpha}{M}I_1(Q^2)+\gamma_{g1}(Q^2)\nu^2+O(\nu^4)\,, \tag{3.40}$$

where the leading order term leads to the sum rule:

$$I_1(Q^2)\equiv\frac{2M^2}{Q^2}\int_0^{x_0}g_1(x,Q^2)dx\,, \tag{3.41}$$

and the second term's coefficient can be expressed as

$$\gamma_{g1}(Q^2)=M\delta_{LT}(Q^2)+\frac{2\alpha}{MQ^2}(I_{TT}(Q^2)-I_1(Q^2))\,. \tag{3.42}$$

A "super-convergence relation" can be formed that is valid at any Q^2 by considering the S_2 amplitude, which is odd in ν. Assuming the behavior for this amplitude as $\nu\to\infty$ is given by $S_2\to\nu^{\alpha_2}$ with $\alpha_2<-1$, then there should be a dispersion relation for νS_2, which is even. By subtracting the dispersion relations for S_2 and νS_2 we obtain:

$$\int_0^1 g_2(x,Q^2)dx=0\,. \tag{3.43}$$

This result is known as the Burkhardt-Cottingham (BC) sum rule [37] and indicates that the sum of all elastic and inelastic contributions should vanish. The elastic and inelastic contributions can be separated and the sum rule can be written in terms of the Sachs form factors

$$I_2(Q^2)=\frac{2M^2}{Q^2}\int_0^{x_0}g_2(x,Q^2)dx=\frac{G_M(Q^2)}{4}\frac{G_M(Q^2)-G_E(Q^2)}{1+\tau}\,, \tag{3.44}$$

with $\tau=Q^2/4M^2$.

3.4 Summary

In this chapter, the formalism of the virtual photoabsorption cross sections and various spin-dependent sum rules were introduced. The generalization of the sum rules to $Q^2 > 0$ provides a unique tool to test theoretical predictions with experimental data over the entire range of the four-momentum transfer. In Chapter 3, the theoretical methods to perform QCD predictions will be discussed and then a comparison will be conducted with the available data. Finally the motivation for experiment E97-110 will be unveiled with respect to theoretical calculations in terms of the sum rules discussed in this chapter. For this dissertation, the measurement of the generalized GDH sum rule of Eq. (3.35) is the main result.

CHAPTER 4

Theoretical Methods

Over the past couple of decades, the spin structure of the nucleon has been experimentally mapped out for a large range of Q^2. Recently, experiments at Jefferson Lab have contributed to the low and intermediate Q^2 region between 0.02 and 2 GeV^2. In this chapter, we will examine some of the more common theoretical methods that are used to predict the Q^2-variation of the structure functions. At low Q^2, predictions are calculated using chiral perturbation theory, whereas the operator product expansion is utilized at large Q^2. The predictions are usually made in regards to the virtual photon-nucleon amplitudes $S_1(\nu, Q^2)$ and $S_2(\nu, Q^2)$. However experimentally, these amplitudes cannot be measured for a space-like virtual photon, $Q^2 > 0$. This is where the dispersive sum rules from Chapter 3 become important, since they relate the Compton amplitudes to integrals of the structure functions. Using the various sum rules, theoretical predictions of the amplitudes can be tested against measurements of the structure functions, provided the dispersion integrals converge [35].

In the first part of this chapter, we give an overview of the theoretical methods avail-

able with an emphasis on chiral perturbation theory, since the results of this thesis are in the low Q^2 regime where it is expected to be applicable. In the second half, the current data will be compared to the different predictions in the low to intermediate Q^2 region.

4.1 Chiral Perturbation Theory

4.1.1 Chiral Symmetry

At low energies and four-momenta, $Q^2 < 1$ GeV^2, the strong interaction's running coupling constant $\alpha_s(Q^2)$ is of order one. This makes expansions in powers of α_s no longer useful. In this region, different techniques are relied upon to make QCD predictions. At low energies, the relevant degrees of freedom in QCD are composite hadrons instead of the quarks and gluons of the DIS region. One approach to tackle the non-perturbative region is to make use of basic QCD symmetries and conserved currents. These serve as guiding principles to construct effective Lagrangians, which approximate QCD at low energy.

We begin with the QCD Lagrangian [38]:

$$\mathcal{L}_{\rm QCD} = -\frac{1}{4g^2} G^{\alpha}_{\mu\nu} G^{\mu\nu}_{\alpha} + \bar{q} i \gamma^{\mu} D_{\mu} q - \bar{q} \mathcal{M} q \,, \tag{4.1}$$

where G is the gluon field strength, q is the quark field, and $\mathcal{M}$ is the diagonal quark mass matrix. The absolute values of the running quark masses $\bar{m}_i$ at the scale of 1 GeV are [5]:

$$\bar{m}_u(1GeV) = (4 \pm 2)\mathrm{MeV} \,, \tag{4.2}$$

$$\bar{m}_d(1GeV) = (8 \pm 4)\mathrm{MeV} \,, \tag{4.3}$$

These masses are small compared to the characteristic hadronic scales, such as the proton's mass, i.e., $m_u/M_p \sim 5{\cdot}10^{-3}$. So we now consider the limit where the m_i vanish and

then treat the light quark masses as perturbations. In this approximation, the c, b and t quarks can be treated as infinitely heavy. For massless fermions, chirality or handedness is identical to the particle's helicity as defined in Eq. 3.7. This results in an extra symmetry of the QCD Lagrangian, so we can introduce left and right handed quark fields:

$$q_{L,R} = \frac{1}{2}(1 \mp \gamma_5)q\,, \tag{4.4}$$

which do not interact with each other. The theory admits a $SU(3)_L \times SU(3)_R$ symmetry, and the invariance of the Lagrangian under this group is referred to as chiral symmetry. The existence of the small but non-zero quark masses explicitly breaks chiral symmetry.

4.1.2 Chiral Symmetry Breaking and Perturbation Theory

In the limit of massless quarks, the theory admits an $U(3)_{\rm L} \times U(3)_{\rm R}$ symmetry; however, the ground state of QCD does not have the full symmetry. Otherwise, all the known hadrons would have a partner of the same mass but with opposite parity, which is contrary to the observed hadron spectrum. As a matter of fact, the physical QCD ground state is asymmetric under chiral symmetry [38]; hence, chiral symmetry is spontaneously broken down to the flavor group $SU(3)_V$, i.e, the vector charge. Goldstone's theorem [39, 40] requires the existence of eight massless pseudoscalar mesons [5]. In nature, the eight lightest hadrons are the pseudoscalar mesons, which include the pions ($\pi^{\pm}$,π^0), kaons ($K^{\pm}$,K^0,$\bar{K}^0$) and eta (η). The Goldstone bosons have mass, since the non-zero quark masses explicitly break chiral symmetry.

We can now construct an effective Lagrangian, which replaces Eq. (4.1) in the low energy limit with two parts:

$$\mathcal{L}_{\rm QCD} = \mathcal{L}_0 + \mathcal{L}_{sb}\,, \tag{4.5}$$

with

$$\mathcal{L}_{\rm sb} = -\bar{q}\mathcal{M}q\,, \tag{4.6}$$

which can now be regarded as a perturbation to the chiral symmetric part of the Lagrangian $\mathcal{L}_0$. The effective Lagrangian still retains the symmetries and symmetry breaking patterns of the fundamental theory of QCD. This approach is reasonable because the light quark masses are small compared to the 1 GeV hadronic gap, which is a consequence of the spontaneous breaking of chiral symmetry.

A low energy expansion is used to order the energies and momenta (p) of the interacting particles such that any matrix element or amplitude derived from the effective Lagrangian is organized in a power series, $\sum_n c_n p^n$. The framework for the expansion is called chiral perturbation theory (χPT) [38]. We note that the radius of convergence is expected to be quite limited; however within this limit, rigorous statements are possible [5].

4.1.3 Baryon Chiral Perturbation Theory

Over the past 15 years, there has been very productive theoretical activity in regards to χPT calculations. Here we highlight the main theoretical work [41–44] relevant to this thesis involving the spin-dependent structure functions and their moments. The theoretical effort is limited to the two flavor case of the up and down quarks. The predictions have typically examined the Q^2-dependence of the Compton amplitudes $S_1(\nu, Q^2)$ and $S_2(\nu, Q^2)$ in the low energy and momentum regions. In Section 3.3, we saw that the Compton amplitudes can be connected to integrals of the spin structure functions via dispersion relations.

As mentioned in the previous section, the low-energy expansion is made in powers of small momenta and quark (pion) masses, which involves pion loops of the effective

theory. The introduction of baryons to the theory creates a complication: the baryon mass is nonvanishing in the chiral limit and adds a new scale to the theory [45]. The implications of this are that there is no guarantee that all next-to-leading-order corrections at order p^4 are given completely by one-loop graphs. Theorists have considered two main approaches for dealing with these complications: Heavy Baryon χPT (HBχPT) and Relativistic Baryon χPT (RBχPT).

Heavy Baryon χPT

In the Heavy Baryon approach, the baryons are considered as very heavy and the theory is expanded in inverse powers of the baryon mass, which results in a consistent counting scheme. However the authors in Ref. [45] warn that the expansion in the ratio of pion to nucleon masses m_π/M_N is not expected to converge very fast. In fact, a significant Q^2-variation was seen for the generalized GDH sum rule when the next-to-leading ($O(p^4)$) order was calculated in χPT [41].

Lorentz-invariant Baryon χPT

Recently Bernard et al. [42, 44] have studied the Compton amplitudes for low Q^2 in a Lorentz-invariant formulation of baryon χPT. A complete one-loop (fourth order) calculation was performed that showed significant differences from the previous results based on HBχPT. The underlying method of this approach involves "infrared regularization", where any dimensionally regularized one-loop integral can be split into an infrared singular and a regular part depending on a particular choice of Feynman parameterization. The contributions from the regular part can be absorbed into low-energy constants of the effective Lagrangian, whereas the chiral expansion of the infrared part leads to the non-trivial momentum and quark-mass dependences of χPT. Results obtained from this

approach are compatible with expectations from naive-dimensional analysis, which was not the case for the HBχPT calculations.

Resonance and Vector Meson Contributions

So far we have only discussed the pion-nucleon contributions. However there are expected to be reasonably sized resonance contributions to the Compton amplitudes, especially from the $\Delta(1232)$ resonance. Ideally, the Δ resonance would be included as a dynamical degree of freedom in the effective Lagrangian, but an effective field theory of the relativistic pion-nucleon-delta system does not exist. So the Δ contribution has only been added systematically in the heavy baryon approach. In this approach, the nucleon-delta mass difference is treated as an additional small parameter. In RBχPT, the Δ contribution is estimated by calculating relativistic Born graphs, which are dependent on a few experimental parameters that are not well known. The predictions with this contribution included have a band of values due to the uncertainties in these parameters. The authors of Ref. [44] have also included contributions from the vector mesons.

One possibility to get around the resonance contributions is to consider quantities involving the difference between proton and neutron observables. In the difference, the resonance contribution largely cancels out and a reduced Q^2 dependence is expected [46], generating a quantity for which χPT predictions are expected to be more reliable.

4.2 Operator Product Expansion

In 1969, Wilson originally introduced the Operator Product Expansion (OPE) [47] as an attempt to formulate a substitute for quantum field theory. The expansion can provide model-independent QCD predictions for the moments of the structure functions via sum

rules. The OPE method separates the perturbative part of the product of two operators from the non-perturbative part. The product of the two operators can be written in the small distance limit $d \to 0$ as

$$\lim_{d\to 0} \sigma_a(d)\sigma_b(0) = \sum_k C_{abk}(d)\sigma_k(0)\,, \tag{4.7}$$

where C_{abk} are known as the Wilson coefficients, which contain the perturbative part and are calculable perturbatively in QCD. The operators σ_k contain the non-perturbative information and hence are not calculable in perturbative QCD. In the DIS region, this formalism is used to develop a product of currents on a local operator basis. The contribution of any operator to the cross section is of the order:

$$x^{-n}\left(\frac{M}{Q}\right)^{\tau-2} \tag{4.8}$$

where $Q = \sqrt{Q^2}$, and $\tau \equiv D - n$ is defined as the "twist". The dimensionality (in powers of mass or momentum) and spin of the operator are represented by D and n, respectively. At large Q^2, the leading twist term known as twist-2 dominates, since higher twists are suppressed by increasing powers of $\frac{M}{Q}$. For small values of Q^2, higher twist contributions are expected to be important.

When the parton model was discussed in Section 2.3.4, we claimed that the $g_2(x, Q^2)$ structure function had no simple interpretation. Now we will explore the g_2 structure function in terms of the twist expansion. This structure function can be separated into twist-2 and higher twist terms:

$$g_2(x, Q^2) = g_2^{WW}(x, Q^2) + \bar{g}_2(x, Q^2)\,, \tag{4.9}$$

where $g_2^{WW}(x, Q^2)$ is purely a twist-2 contribution and is entirely determined by $g_1(x, Q^2)$ from the Wandzura-Wilczek relation [48]:

$$g_2^{WW}(x, Q^2) = -g_1(x, Q^2) + \int_x^1 \frac{g_1(y, Q^2)}{y} dy\,. \tag{4.10}$$

The second term of Eq. (4.9) contains information on higher twist effects which are related to quark-gluon interactions.

First Moment of $\mathbf{g_1(x, Q^2)}$

We now consider the first moment of the structure function $g_1(x, Q^2)$ defined by

$$\Gamma_1(Q^2) \equiv \int_0^1 g_1(x, Q^2) dx \,. \tag{4.11}$$

Using the OPE leads to the twist expansion for the first moment:

$$\Gamma_1(Q^2) = \sum_{\tau=2,4,\ldots} \frac{\mu_\tau(Q^2)}{(Q^2)^{(\tau-2)/2}} \,, \tag{4.12}$$

with the coefficients μ_τ are a perturbative series in α_s. The coefficients are related to nucleon matrix elements of twist $\leq \tau$. The application of the OPE requires summation over all hadronic final states, so the elastic contribution at x = 1 is included [49].

The leading-twist term μ_2 can be expressed into flavor triplet (g_A), octet (a_8) and singlet ($\Delta\Sigma$) axial charges:

$$\mu_2(Q^2) = \left(\pm \frac{1}{12} g_A + \frac{1}{36} a_8 \right) + \frac{1}{9} \Delta\Sigma + O(\alpha_s(Q^2)) \tag{4.13}$$

where +(–) denotes the proton (neutron) and the $O(\alpha_s)$ terms are the Q^2 evolution due to QCD radiative effects. These higher order terms are calculable from perturbative QCD. The g_A axial charge is known precisely from neutron β-decay and a_8 can be extracted from hyperon β-decay assuming $SU(3)$ flavor symmetry. Within the parton model, $\Delta\Sigma$ is the amount of spin carried by quarks. This quantity has been extracted from a global analysis of the world data from DIS experiments [50].

The difference between the first moments of the proton and neutron g_1 spin structure function gives rise to the well-known Bjorken sum rule as $Q^2 \to \infty$:

$$\Gamma_1^p(Q^2) - \Gamma_1^n(Q^2) = \frac{1}{6} g_A + O(\alpha_s(Q^2)) + O(1/Q^2) \,. \tag{4.14}$$

Bjorken first derived this sum rule using the current algebra method [51], so it provides a fundamental test of the structure of QCD. With the perturbative QCD corrections included, the Bjorken sum rule has been tested and verified to the level of 10%.

4.3 Lattice Gauge Theory

Lattice QCD [5] provides a framework for non-perturbative calculations of hadronic structure. The difficulties of solving QCD analytically are avoided by discretizing QCD on a finite space-time lattice. In principle, the technique involves a simulation of QCD; however, the calculations are numerically intensive. To ensure that the calculation provides the desired observable, the lattice spacing a needs to be small and the finite volume needs to be large. However a compromise needs to made, since the calculations are computationally costly. Lattice QCD is a rapidly developing field and important conceptual and technical progress is being made to improve this method's current capabilities.

The hope is one day lattice calculations will bridge the gap in the intermediate Q^2 regime, where neither OPE or χPT can make predictions. A strong connection between lattice calculations and χPT has recently developed. The results from lattice QCD have to be extrapolated to the value of the observable in the limit of infinite volume and as the lattice spacing becomes infinitesimal. One approach has been to use the predictions from χPT to make these extrapolations [52, 53]. Hence, lattice QCD results are now tied to χPT, and the verification of χPT predictions with data is essential.

4.4 The Phenomenology MAID Model

The unitary isobar model MAID [54] utilizes phenomenological fits to photo- and electroproduction data on the nucleon from the pion-production threshold to W = 2 GeV. Resonance contributions are included by taking into account unitarity to provide the correct phases of the pion photoproduction multipoles. The model also assumes the resonance contributions have Breit-Wigner forms with contributions to the helicity-dependent cross sections given by

$$\sigma_{\frac{1}{2}(\frac{3}{2})} = \frac{4M}{W_{\rm res}\Gamma_{\rm res}} A^2_{\frac{1}{2}(\frac{3}{2})} B(\nu, Q^2)\,, \tag{4.15}$$

where $W_{\rm res}$ and $\Gamma_{\rm res}$ are the mass and width of the resonance, respectively. The helicity-dependent amplitudes are given by $A^2_{\frac{1}{2}(\frac{3}{2})}$, and $B(\nu, Q^2)$ represents the generalization to electroproduction of the Breit-Wigner form. The model includes the resonances mentioned in Table 2.1 plus the P_{11}(1440) and D_{33}(1700). Contributions from vector mesons and a non-resonant background are also included.

With this model, good agreement has been obtained with pion photo- and electroproduction data on the nucleon for both polarized observables and differential cross sections (see [18, 19, 54]). The model validates the proton GDH sum rule; however, the model does not verify the neutron GDH sum rule at the real photon point. The neutron discrepancy may be caused by neglecting final state interactions for pion production from deuterium or ^{3}He targets, a larger than expected two-pion contribution for the neutron, or possible multipole expansion modifications due nuclear binding effects for the neutron.

4.5 Data and Theoretical Prediction Comparisons

In the last decade, experimental results have become available in the low and intermediate Q^2 regions which allows us to test our understanding of QCD in the non-perturbative and transition regimes. In this region, the effective degrees of freedom are the hadrons rather than the quarks and gluons of perturbative QCD. In this section, we discuss the experimental data and make a comparison to the available theoretical predictions. The discussion will be restricted to measurements of the neutron spin structure from a polarized ^{3}He target. However data are also available for the proton [55] and deuteron [56]. An overview of the recent data on sum rules and moments of the nucleon spin structure functions is available in Ref. [49]

Results for the neutron generalized GDH sum rule (red squares) from Eq. (3.35) are shown in Fig. 4.1. The results were extracted from JLab experiment E94-010 [57] from pion threshold to W = 2 GeV. For the virtual photon flux factor, the convention in Eq. (3.4) was used to make comparisons with the theoretical predictions. The uncertainties on the data are statistical only. The systematic uncertainties are represented by the green band. The blue squares include an estimate of the unmeasured $W > 2$ GeV contribution. The data illustrate a smooth Q^2-variation from large negative values at low Q^2 to smaller values at higher Q^2. The data approach the HERMES neutron results [58], which only include contributions from the DIS part of the integral. At the real photon point, the value of the GDH sum rule (-232.8 μb) is represented by the asterisk. Two χPT predictions are shown for $Q^2 > 0$ using HBχPT [41] and RBχPT [42]. The band indicates the RBχPT calculation with resonance and vector meson effects included [44], where the large uncertainty is due to the parameters used as discussed in Section 4.1.3. The lowest Q^2 point overlaps the band from the RBχPT calculation with resonance contributions.

Above Q^2 = 0.3 GeV^2, the χPT predictions are much more negative than the data. Also shown is the MAID model calculation, which is more positive than the data and should only be compared to the red squares.

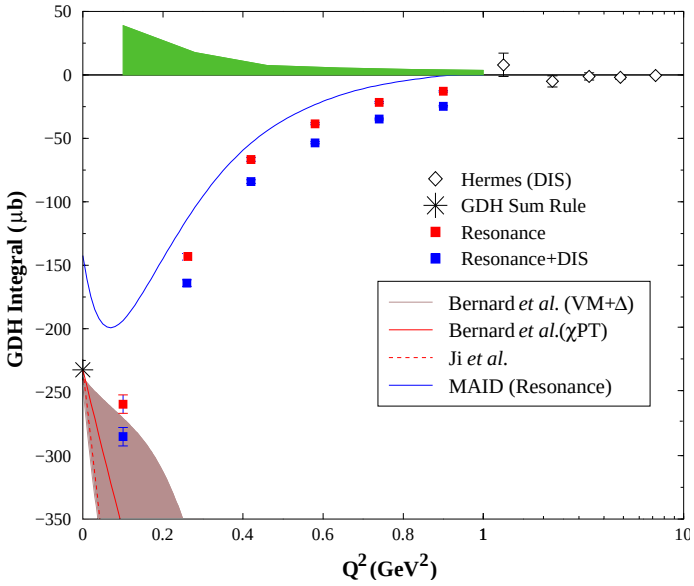

FIG. 4.1: Results for the neutron generalized GDH sum rule $I_{TT}(Q^2)$ from experiment E94-010.

The generalized spin polarizabilities as defined in Section 3.3 provide bench mark tests for the χPT predictions. The integrands for the polarizabilities are weighted by an additional factor of ν^{-2}, which suppresses the DIS contribution from the unmeasured region $W > 2$ GeV^2. One of the biggest questions in χPT is how to handle the nucleon resonance contributions, especially the dominant Δ resonance. The authors in Refs. [43] and [44] have pointed out that the δ_{LT} spin polarizability should be insensitive to the Δ resonance, whereas γ_0 is much more sensitive.

In Fig. 4.2, the spin polarizabilities for the neutron [59] are shown between Q^2 of 0.1 and 0.9 GeV^2. The solid squares show the data with statistical uncertainties, and the

systematic uncertainties are given by the dark band. Predictions from HBχPT [43] and RBχPT [42] are compared with the experimental data. The calculation with resonance contributions [44] is indicated by the light gray bands. First we consider the lowest Q^2 points at 0.1 and 0.26 GeV^2. For the γ_0 spin polarizability (top, left panel), the RBχPT calculation with resonance contributions agrees well with the data for Q^2 = 0.1 GeV^2. However the HBχPT shows significant differences even at this low Q^2. The MAID model shows good agreement with the higher Q^2 point, whereas a sizable difference is seen for the lower point.

The δ_{LT} spin polarizability, which is expected to be less sensitive to the resonance contributions, is shown in the bottom left panel. Surprisingly the data show a significant disagreement with both predictions even at the lowest Q^2 point. The MAID model on the other hand is in good agreement with these results.

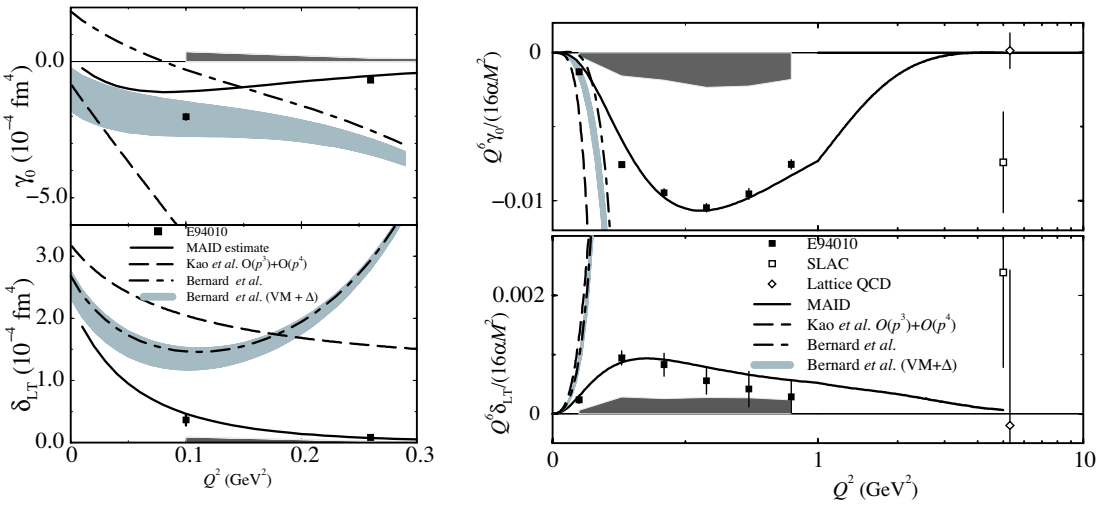

FIG. 4.2: Results for the neutron spin polarizabilities $\gamma_0(Q^2)$ and $\delta_{LT}(Q^2)$ from experiment E94-010.

In the right panel of Fig. 4.2, the polarizabilities are shown multiplied by Q^6. The MAID and χPT calculations are shown for comparison. The Q^6-weighted polarizabilities

are expected to exhibit scaling (become independent of Q^2) at large Q^2. Clearly neither spin polarizability shows this below 1 GeV^2. The world data from Ref. [60] and a lattice QCD calculation [61] are shown at Q^2 = 5 GeV^2.

The above results are only a sample of the quantities that provide comparisons between the data and theoretical predictions. Comparisons have also been made for the BC sum rule and the first moment of $g_1(x, Q^2)$. As mentioned previously, data are also available for the proton and deuteron. From the discussion in this section, it becomes clear that with the available data at $Q^2 \geq 0.1$ GeV^2 that the χPT predictions have some success as in the extended GDH sum rule and also for the proton results. However the δ_{LT} spin polarizability, which was expected to be a solid testing ground, shows significant differences with the current calculations for the neutron. The predictions from χPT are expected to have a limited range, perhaps only up to 0.1 GeV^2. At present, the data is at the limits of this range, and further measurements at very low Q^2 are required to provide definitive tests of the χPT predictions.

4.6 Summary

In this chapter, the theoretical tools that are commonly employed to predict the sum rules and the moments of the spin structure functions were presented. At high Q^2, the operator product expansion is used to make non-perturbative calculations. Ji and Osborne [35] have argued that OPE is expected to be a good approximation down to $Q^2 \sim 0.5$ GeV^2. In the low Q^2 region, predictions from low-energy effective field theories such as χPT have grown into a mature field. However the predictions from χPT are expected to be valid in a limited range from Q^2 = 0 to 0.1 GeV^2. For observables that involve a difference between proton and neutron observables, the range maybe extended up to 0.2–0.3 GeV^2.

A small gap region exists between the two methods that may possibly be filled by lattice QCD calculations, which have shown promise in the past decade. Of course, theoretical predictions are complemented by the experimental data, which help guide the theoretical process in the transition region between perturbative and non-perturbative QCD.

CHAPTER 5

The Experiment

Experiment E97-110 was conducted at the Thomas Jefferson National Accelerator Facility (TJNAF) in experimental Hall A in April-May and July-August 2003. TJNAF, also known as Jefferson Lab (JLab), is located in Newport News, VA. The experiment was performed to provide a precise measurement of the inclusive polarized cross sections for electron scattering from ^{3}He. The data was acquired at low momentum transfers (0.02 $< Q^2 <$ 0.3 GeV^2) in the quasi-elastic and resonance regions. The goal of the experiment was to extract the ^{3}He and neutron spin-dependent structure functions $g_1(x, Q^2)$ and $g_2(x, Q^2)$ and their relevant moments. This low-Q^2 range allows us to make a definitive test of the χPT predictions presented in the previous chapter. The kinematic coverage is shown in Fig. 5.1. Longitudinally polarized electrons with nine incident energies between 1.1 and 4.4 GeV were scattered from a high-pressure polarized ^{3}He target. The target was polarized in both longitudinal and transverse directions, which allows us to extract both structure functions. The scattered electrons were detected in the right Hall A high resolution spectrometer (HRS) at angles of 6° and 9°. The small scattering angles were reached

with the addition of a septum magnet [62] located in front of the spectrometer.

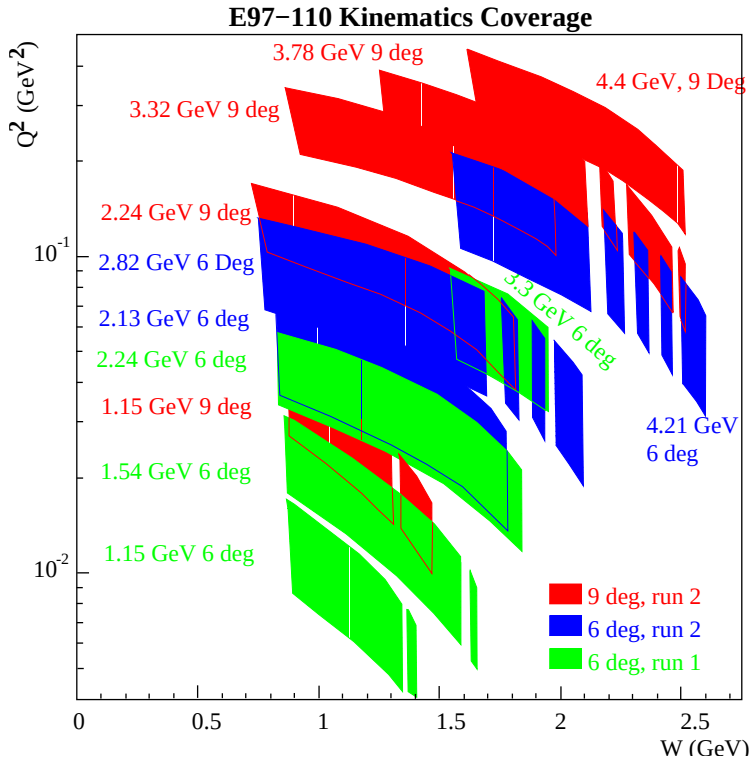

FIG. 5.1: Kinematic coverage of experiment E97-110.

The experimental data were acquired in two separate run periods denoted as the first (green regions) and second periods (blue and red regions) in Fig. 5.1. E97-110 was the first experiment to use the septum magnet, and the magnet was found to be mis-wired during the commissioning period. In particular, this caused a significant loss in acceptance but not in statistics due to the forward scattering angle and low beam energies. Between the two run periods, the magnet was repaired and successfully commissioned during the second period. However due to the complications of the mis-wired magnet, the analysis presented in this document is only concerned with the eight incident beam energies shown in blue and red. The first period analysis is being conducted by other collaborators [63].

This chapter will discuss the polarized electron beam, the Hall A beamline components and the details of the polarized ^{3}He target. Various beamline components are available to monitor the beam current, position, polarization and energy in the hall. Understanding the systematics from these components is crucial in performing a precise measurement of the polarized cross sections.

5.1 The Electron Accelerator

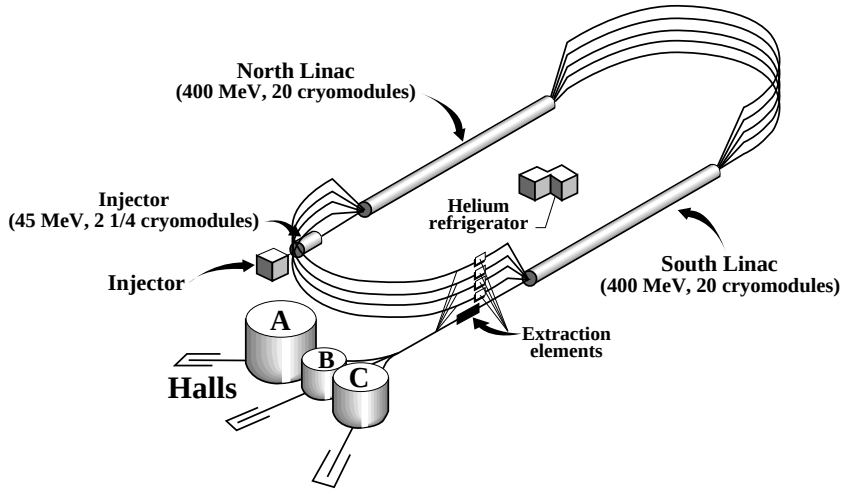

FIG. 5.2: Schematic of the Jefferson Lab accelerator and experimental halls.

The accelerator consists of a polarized source, an injector, two linacs, two re-circulation arcs and extraction elements to send beam into the three experimental halls: A, B and C. A diagram of the accelerator and its components is shown in Fig. 5.2. The polarized electron source will be discussed in the next section (Section 5.1.1).

Once the polarized electron beam is generated, the electrons enter into the accelerator. The polarization angle of the electrons is set with a Wien filter so that the electrons are

longitudinally polarized in the halls. The $g-2$ precession through the accelerator is taken into account when the polarization angle is set. The injector then accelerates the electrons up to 45 MeV before they enter the first linac. Each linac consists of 20 superconducting cryomodules that are composed of eight superconducting radio-frequency (RF) cavities. The cavities produce field gradients of $\simeq$ 7 MeV/m. The electrons then enter a recirculation arc and are sent into the second linac where they are accelerated again. After the second linac, the beam can either enter the second recirculation arc and be accelerated up to five passes, or it can be extracted and sent into the experimental halls. The extraction is performed using RF separators and magnets.

Originally the accelerator was designed to accelerate the electrons up to 4 GeV. However the maximum achieved beam energy is slightly less than 6 GeV due to the high performance of the cavities. The accelerator can provide beam to all three halls simultaneously at three different energies. It is also possible for the accelerator to deliver the maximum beam energy to all three halls at the same time. The maximum beam current available among the three halls is 200 μA, which is split arbitrarily between three interleaved 499 MHz bunches. Each of the bunches can then be peeled off to any one of the halls. Halls A and C are capable of taking beam currents greater than 100 μA, whereas Hall B typically runs at less than 100 nA.

5.1.1 Polarized Electron Beam

The polarized electron beam is produced by illuminating a gallium arsenide (GaAs) photocathode with circularly polarized photons. The photons excite electrons from the valence band to the conduction band in the photocathode. The electrons are pulled from the conduction band into the accelerator by holding the crystal at a bias voltage of -100

kV [64]. The GaAs cathode crystal structure contains a $P_{3/2}$ valence band and a $S_{1/2}$ conduction band. The degeneracy of the GaAs valence band is broken by introducing a strain on the crystal. A "strained" GaAs cathode is created by growing a thin layer of GaAs on a GaAsP substrate. With the degeneracy broken, it becomes (theoretically) possible to produce a beam of 100% polarized electrons. The energy levels and band gaps of a strained GaAs cathode is shown in Fig. 5.3. Right (left) circularly polarized light excites electrons from the valence band into the m_J = +(−) 1/2 state of the conduction band.

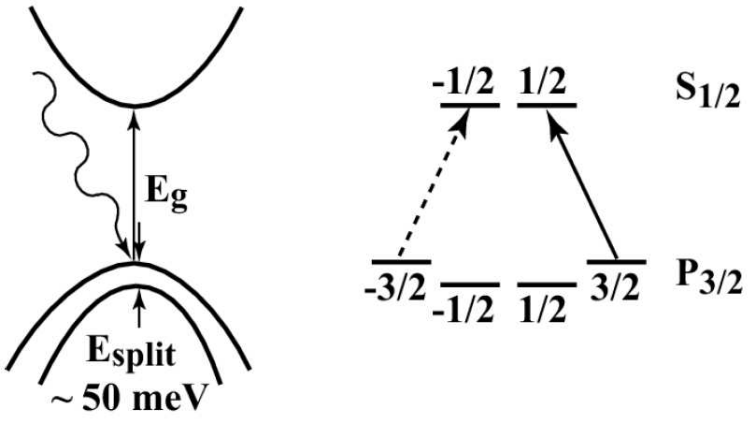

FIG. 5.3: Energy level and bandgap diagram for a strained GaAs cathode. Reproduced from [64].

To enable the measurement of helicity-dependent observables such as asymmetries and cross-section differences, the beam helicity is reversed. This process is performed frequently with the aid of a Pockels cell to minimize the impact of time-dependent systematic effects. Pockels cells are electro-optic devices that are birefringent. Their birefringence is linearly proportional to the electric field applied. At Jefferson Lab, they are used to provide fast reversal of the beam helicity and to convert linearly-polarized laser

light into circularly-polarized light. The beam helicity is pseudorandomly flipped at 30 Hz by switching the sign of the voltage in the Pockels cell. An insertable half-wave plate (IHWP) located upstream of the Pockels cell also provides a means to reverse the beam helicity. Insertion of the half-wave plate is done to check and to help cancel helicity-dependent systematic effects.

5.1.2 Beam Helicity

For experiment E97-110, the "G0 helicity scheme" [65] as shown in Fig. 5.4 was used. The characteristics of this scheme are as follows:

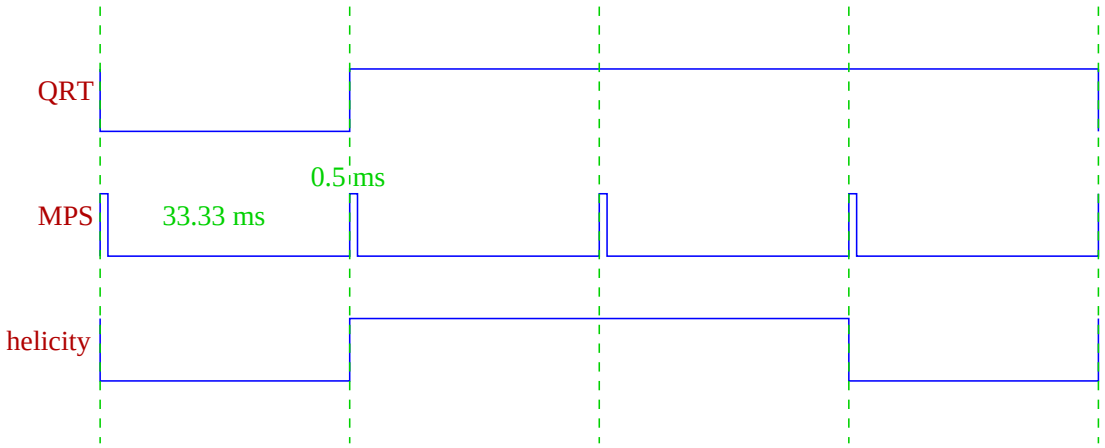

FIG. 5.4: Beam helicity sequence used during experiment E97-110.

- The macro-pulse trigger (MPS signal at 30 Hz) is used as a gate to define periods when the helicity is valid.
- The helicity sequence has a quartet structure (either $+--+$ or $-++-$). The helicity of the first MPS gate is chosen pseudorandomly.

- Quartet trigger (QRT) defines when a new random sequence of four helicity states has begun.
- The helicity information sent to the halls are typically delayed by eight MPS.

A blank-off period of approximately 0.5 ms exists for each 33.3 ms gate period. During this blank-off period, the Pockels cell has time to change and settle. The quartet sequence provides for exact cancellation of linear drifts over the sequence's timescale, and the delay in helicity reporting breaks any correlations with the helicity of the event by suppressing crosstalk. For the experiment, two different delays were used. For the first period, the helicity reporting was delayed by 8 MPS; whereas for the second period, the helicity was reported in-time, i.e., with no delay.

5.1.3 Charge Asymmetry Feedback

Though the Pockels cell produces highly circularly polarized light, the cells contain imperfections that generate a small linear component causing the polarization to become elliptical. When the helicity is reversed, the angle of the ellipse changes creating an helicity-correlated asymmetry known as Polarization Induced Transport Asymmetry (PITA) [66].

An helicity feedback system was used to minimize this effect for the physics data. The Hall A Proton Parity Experiment (HAPPEx) data acquisition system was used to monitor the charge asymmetry and adjust the Pockels cell voltage accordingly. A rotatable half-wave plate (RHWP) was also placed downstream of the Pockels cell. This half-wave plate can rotate the direction of the residual linear polarization to reduce its effect on the helicity-correlated beam parameters. For this experiment, a charge asymmetry less than 200 ppm was sufficient to suppress this effect as a source of systematic error. Typically

the charge asymmetry was better than this. However there were a few times when the feedback system failed. These instances are discussed in Section 7.2.3.

5.2 Hall A Beamline

5.2.1 Beam Current Measurement

The beam current is measured by two beam current monitors (BCMs), which are located 25 m upstream from the target. The BCMs are stainless steel cylindrical high-Q ($\sim$ 3000) waveguides that are tuned to the beam's frequency (1497 MHz) [67]. Their outputs' voltage levels are proportional to the beam current. The RF output signals from the cavities are split into two parts: sampled and integrated data. In between the two BCM cavities is an Unser Monitor (Parametric Current Transformer) which provides an absolute measurement of the current and can be used to calibrate the cavities. However since the Unser's output signal drifts over a time period of several minutes, it is not used for continuous current monitoring. For this experiment, the Faraday cup was used in the calibration [68], and the Unser was used as a crosscheck of the calibration.

The sampled data are processed by a high-precision digital AC voltmeter. The digital output of the voltmeter represents the RMS of the input signal once every second. The output is then recorded every 1–2 s by the data logging process. The integrated data are sent to an RMS-to-DC converter and then to a voltage-to-frequency converter. The output frequency is then sent to the VME scalers and injected into the data stream. The scalers accumulate during the run and each BCM scaler provides a number proportional to the time-integrated voltage level, which represents the total beam charge. The RMS-to-DC output is linear for currents between 5 to 200 μA. A set of amplifiers was introduced with

gain factors of 1, 3 and 10 to extend the linearity below 5 μA.

The beam current and hence charge, $Q_a = I_a t$, is obtained from the BCM scaler reading as follows:

$$I_a = \frac{\frac{N_a}{t} - f_a}{k_a}, \tag{5.1}$$

where a = 1, 3, 10 is the gain factor, t is the time for each run (in seconds) and N_a is the BCM scaler reading for each gain factor. The calibration constants k_a and BCM offsets f_a are determined from calibration runs. For E97-110, the calibration was performed during the experiment in August 2003 [69]. The calibration constants for the upstream and downstream cavities are given in Table 5.1, and compared to earlier calibrations [68]; these results differ by $< 1\%$.

Amplification	Upstream Cavity	Downstream Cavity
1	1338.4	1335.5
3	4100.7	4140.9
10	12467.5	13015.1

TABLE 5.1: The E97-110 BCM calibration constants [69].

The BCM offsets are determined from the calibration runs during the periods without beam delivery to the experimental hall. The time dependence of the offsets were checked by using runs with periods without beam or cosmic runs and were expected to be reasonably stable during the experiment. Unfortunately the offsets were not stable during the experiment, so a careful analysis was conducted to determine the offsets throughout the second run period. Details of this analysis can be found in Ref. [70].

For experiment E97-110, the data were taken with beam currents between 0.5 and 10 μA. For currents above 5μA, the x3 gain signals were used, and below 5μA, the x10

gain signals were used. The x1 gain signals were not used in the data analysis.

5.2.2 Beam Position Measurement

Two beam position monitors (BPMs) located 7.524 m and 1.286 m upstream of the target are used to determine the position and direction of the beam at the target location. The BPMs provide a non-invasive measurement when beam is present in the hall. Each BPM consists of four wire antennas contained within a cylinder, which is parallel to the beam direction. When the beam passes through the BPM system, a signal is induced in the antennas that is inversely proportional to the distance from the beam.

The absolute position of the beam is determined by calibrating the BPMs with two superharps (wire scanners) that are located adjacent to the BPMs. The superharps provide an invasive measurement of the beam position and consist of three wires oriented vertically and at $\pm$ 45°. The wires are scanned across the electron beam resulting in a shower of particles that are then detected. The superharps are routinely surveyed with respect to the Hall A coordinate system. The BPMs have a resolution of 20 μm at 10 μA.

5.2.3 Raster

The experiment used high-pressure glass cells with thin glass end windows (100–300 μm). The beam position was rastered to avoid overheating the glass windows, since the electron beam is typically focused to 100–200 μm when it enters the hall. For experiment E97-110, a new triangular raster was used, which copied the Hall C design [71]. The new raster provides a major improvement over the sinusoidal raster [10] reducing dwell time at the peaks. A uniform density distribution of beam on the target is achieved by moving the beam position with a time-varying dipole magnetic field with a triangular waveform.

The raster contains two dipole magnets, one vertical and one horizontal, which are located 23 m upstream from the target.

In the electronics design, an "H-bridge" is used that allows one pair of switches to open and another pair to close simultaneously and rapidly at 25 kHz. The current is drawn by HV supplies and rises according to

$$I(t) = \frac{\varepsilon}{R}\left(1 - e^{-\frac{t}{\tau}}\right) , \tag{5.2}$$

where $\tau = \frac{L}{R}$ is the time constant with resistance R and inductance L. The time and applied voltage are t and ε, respectively. In Fig. 5.5, a sample raster pattern using the triangular waveform is shown. For the experiment, different raster sizes were used. Early in the experiment a 2 mm $\times$ 2 mm raster was used. After one of the target cells ruptured, the raster size was increased to 3 mm $\times$ 3 mm for the 4.209 GeV data, and the majority of the second period data were taken with a 4 mm $\times$ 4 mm raster size.

5.2.4 Beam Energy

There are two independent methods to measure the absolute beam energy in Hall A. The eP measurement [67] utilizes the elastic ^{1}H(e,e'P) reaction. The beam energy is determined by measuring the scattered electron angle θ_{e} and the recoil proton angle θ_{p}, which are constrained by

$$E = M_{\mathrm{p}} \frac{\cos\theta_{\mathrm{e}} + \frac{\sin\theta_{\mathrm{e}}}{\tan\theta_{\mathrm{p}}} - 1}{1 - \cos\theta_{\mathrm{p}}} + O\left(\frac{m_{\mathrm{e}}^2}{E^2}\right) , \tag{5.3}$$

where M_{p} and m_{e} are the proton and electron masses, respectively. The schematic of the eP system is shown in Fig. 5.6. The eP target consists of a rotating thin film (10$-$30 μm) of CH_2 located about 17 m upstream of the Hall A pivot. The electron and proton are measured in coincidence by two sets of detectors [72], which are placed symmetrically

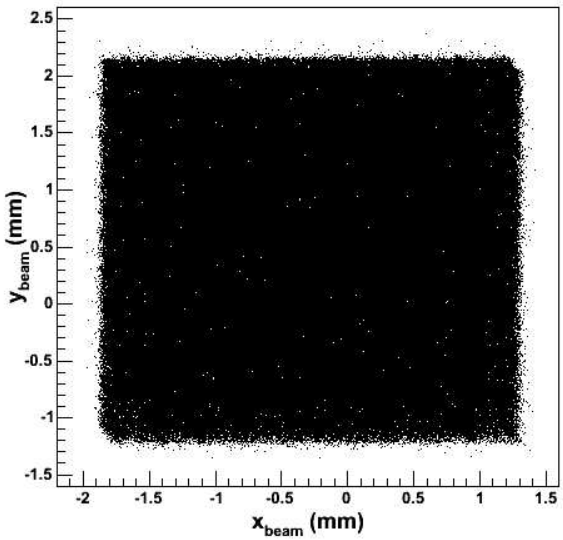

FIG. 5.5: Raster pattern ($\simeq$ 3mm $\times$ 3 mm) showing the horizontal ($x_{\rm beam}$) and vertical beam ($y_{\rm beam}$) positions in mm.

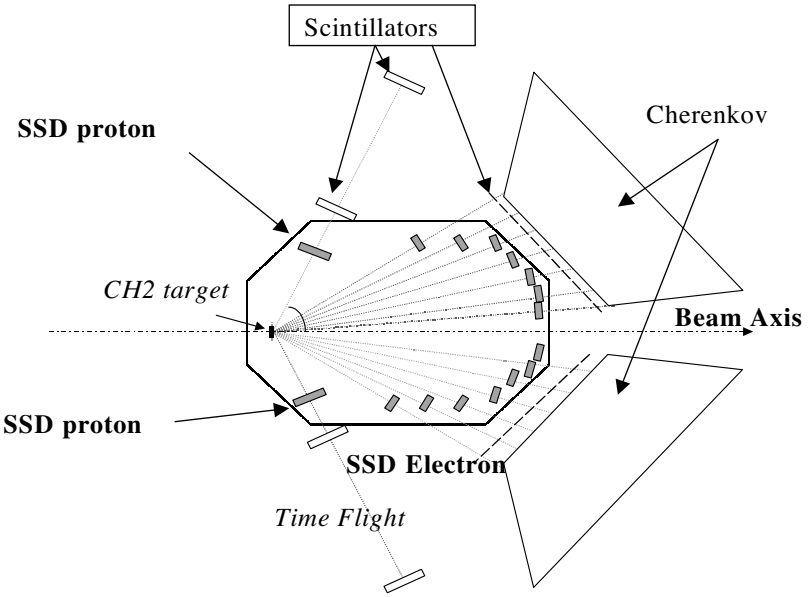

FIG. 5.6: Diagram showing the components of the eP energy measurement system. Reproduced from [67].

about the beamline. The proton detectors are located at an angle of 60° with respect to the beamline. On the other hand, the electron detectors are located at a range of angles from 9° to 41°, which corresponds to an incident energy range of 0.5 to 6.0 GeV. The proton detectors consists of two scintillator planes and a silicon micro-strip detector. The electron detector consists of silicon strip detectors, a scintillator plane and a Čerenkov counter. The achieved uncertainty from the eP method is $\leq$ 2 x 10^{-4} GeV.

The second method to measure the beam energy is called the Arc energy measurement [72]. The energy is determined by measuring the deflection angle of the beam in the 40 m arc section of the beamline. The momentum of the electron deflected by a magnetic field is related to the field integral of the eight dipoles and the bend angle θ through the arc section by

$$p = k\frac{\int \vec{B} \cdot \vec{dl}}{\theta}\,, \tag{5.4}$$

with k = 0.299792 GeV rad T^{-1} m^{-1}/c. The nominal bend angle of the electron beam in the arc section is 34.3°. Two measurements are performed simultaneously. The field integral of the eight dipoles in the arc is measured using a 9th identical dipole (reference magnet) that is connected in series with the others, and the actual bend angle of the arc is measured using two pairs of wire scanners (superharps), one before and one after the arc. The Arc energy measurement also provides an absolute measurement to the 2 x 10^{-4} GeV level.

The beam energy is also monitored continuously online using the Tiefenback measurement [73]. This method is non-invasive and uses the relation between the field integral value and the set current in the eight dipoles of the arc section. Corrections are made using the arc BPMs and the transfer functions for the Hall A beamline magnets. The energy from this method is accurate to the 5 x 10^{-4} GeV level.

Angle	Beam Energy (MeV)	Target Cell
6°	2134.2	Penelope
6°	4208.8	Priapus
6°	2134.9	Priapus
6°	2844.8	Priapus
9°	1147.3	Priapus
9°	2233.9	Priapus
9°	3318.8	Priapus
9°	3775.4	Priapus
9°	4404.2	Priapus

TABLE 5.2: The average beam energy from Tiefenback measurements for the second run period.

Beam Energy for E97-110

During the experiment, only one beam energy measurement was performed using the eP measurement system. That measurement was performed at the end of running for the 2.135 GeV beam energy. The result from this measurement was 2135.67 MeV $\pm$ 0.20 MeV $\pm$ 0.46 MeV, where the first uncertainty is statistical and the second from systematics. The Tiefenback measurement is relied on for the remaining energies. Table 5.2 summarizes the average beam energies for the experiment's second run period. Details on the energy determination are available in Ref. [74]. Two periods of data taking exists for the 2.135 GeV beam energy. The first four momentum settings at this energy were taken with the polarized ^{3}He cell Penelope. After a week of running, the cell ruptured and was replaced with the cell Priapus. The rest of the data at this energy were taken with Priapus. Both the Tiefenback and eP energy measurements indicate that beam energy for the Priapus data was about 0.7 MeV higher than for the Penelope data. Within the total uncertainty, the eP measurement agrees with the Tiefenback measurement.

5.2.5 Beam Polarization

The typically electron beam polarization is $75-85\%$. Two polarimeters exist in Hall A to measure the beam polarization: the Møller and Compton polarimeters. The two polarimeters provide partially overlapping and complementary measurements.

Møller Polarimeter

The Møller polarimeter [67] exploits Møller scattering of polarized electrons off polarized atomic electrons in a magnetized foil:

$$\vec{e} + \vec{e} \rightarrow e + e \,. \tag{5.5}$$

The Møller scattering cross section depends on the beam $P^i_{\rm b}$ and target polarization $P^i_{\rm t}$ along the i^{th} axis:

$$\sigma = \sigma_0 \left[1 + \sum_{i=X,Y,Z} \left(A_{ii} P^i_{\rm t} P^i_{\rm b} \right) \right] , \tag{5.6}$$

where i defines the polarization projections. The analyzing powers of the polarization projections are given by A_{ii}, and σ_0 is the unpolarized Møller cross section:

$$\sigma_0 = \left[\frac{\alpha(1+\cos\theta_{\rm cm})(3+\cos^2\theta_{\rm cm})}{2m_{\rm e}\sin^2\theta_{\rm cm}} \right]^2 , \tag{5.7}$$

where $\theta_{\rm cm}$ is the scattering angle in the center of mass frame.

If we take the beam direction to be along the z-axis and the y-axis is normal to the scattering plane, then the analyzing powers become:

$$A_{ZZ} = -\frac{\sin^2\theta_{\rm cm}\,(7+\cos^2\theta_{\rm cm})}{(3+\cos^2\theta_{\rm cm})^2} \,, \tag{5.8}$$

$$A_{XX} = -A_{YY} = -\frac{\sin^4\theta_{\rm cm}}{(3+\cos^2\theta_{\rm cm})^2} \,. \tag{5.9}$$

The longitudinal polarization is extracted from A_{ZZ} and from the knowledge of the target polarization. The analyzing power has its maximum value of 7/9 for $\theta_{\rm cm}$ = 90°.

The polarization measurement is invasive and conducted at very low beam currents. An asymmetry is measured rather than the cross section, since the asymmetry, which is a ratio of cross sections, is insensitive to many of the systematics related to cross-section measurements. The target foil, which is oriented at an angle of $\pm$ 20° with respect to the beam in the horizontal plane, provides sensitivity to both longitudinal and transverse beam polarizations. The transverse component then cancels out when the average is taken. False asymmetries are also partially canceled by taking measurements with the target foil polarized in the opposite direction.

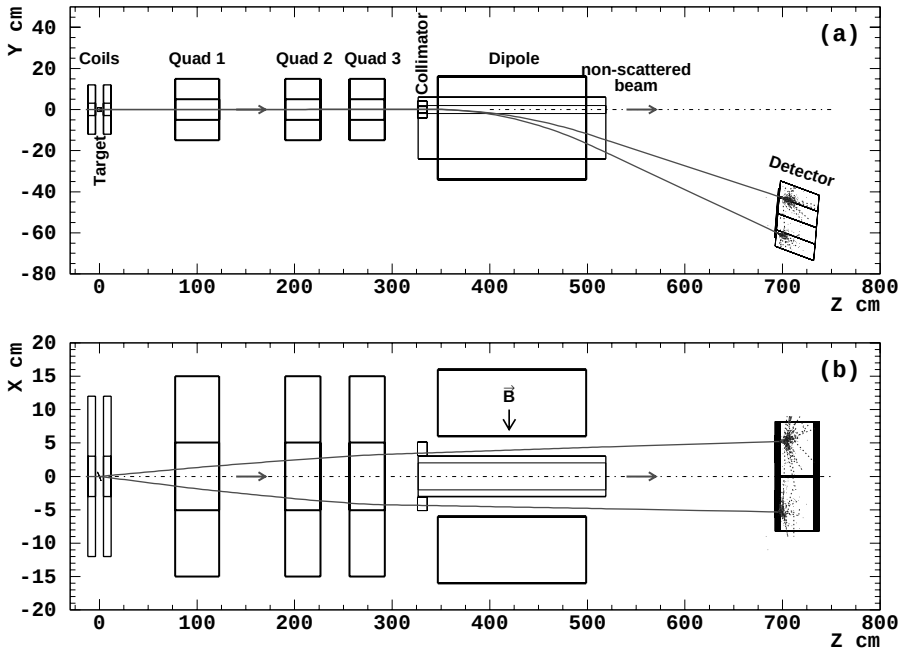

FIG. 5.7: Schematic of the Møller Polarimeter with the top plot presenting a side view and the bottom a top view. Reproduced from [67].

Figure 5.7 shows the schematic of the Møller polarimeter and magnetic spectrometer that is used to detect two scattered electrons in coincidence. The spectrometer consists of three quadrupoles and a dipole. The detector system contains two lead-glass calorimeter

modules that are split into two arms for the coincidence measurement. The statistical accuracy is typically 0.2% [67], whereas the systematic error is dominated by the knowledge of the foil polarization, which has a 3% relative uncertainty.

Compton Polarimeter

The Compton polarimeter [67] is located at the entrance of Hall A and consists of a magnetic chicane, polarized photon source, electromagnetic calorimeter and an electron detector. The polarimeter measures the asymmetry in the scattering of circularly polarized photons off of the polarized electron beam. The beam polarization P_b is extracted from

$$P_b = \frac{A_{\rm exp}}{P_\gamma A_{\rm th}}\,, \tag{5.10}$$

where A_{exp} is the experimentally measured asymmetry, P_γ is the photon polarization and $A_{\rm th}$ is the Compton analyzing power. The photon polarization has been measured to be greater than 99%.

The electron beam is deflected vertically by the four dipole magnets in the Compton chicane so that the beam will cross the photon beam at the Compton interaction point. The interaction point is located at the center of the chicane. A resonant Fabry-Pérot cavity is used to increase the photon density. The scattered electrons are detected in the silicon strip detector, and the backscattered photons are detected by the calorimeter. The data acquisition system can be triggered either by single electrons, single photons, or with electrons and photons detected in coincidence.

The polarization measurement is non-invasive, so it can be performed while the primary beam is delivered on the experimental target. The polarization of the photon beam can be reversed with a half-wave plate in order to reduce beam helicity-correlated effects. The figure of merit of the Compton polarimeter is proportional to E^2_{beam}, the electron

beam energy squared, which leads to less accurate measurements at low beam energies. The relative systematic error is approximately $1-1.5\%$, with the main contribution coming from the detectors' resolution in the determination of the analyzing power [67]. A statistical accuracy of 1% has been achieved with an hour of running the polarimeter. For experiment E97-110, the statistical accuracy from the Compton polarimeter was 3–5% because of the low beam currents used. Hence, the Møller polarimeter was the main source of beam polarimetry for the experiment.

Beam Polarization for E97-110

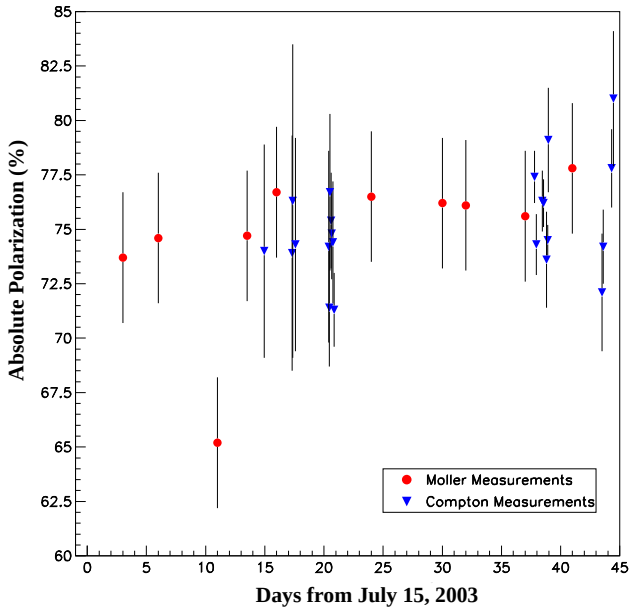

FIG. 5.8: The average beam polarization from the Møller and Compton polarimeters for the second run period.

The beam polarization measurements from both polarimeters are shown in Fig. 5.8. The average Møller and Compton polarizations were 74.7% and 74.9%, respectively [69].

A summary of the beam polarization measurements are available from Ref. [74].

During the first run period, a sizable bleedthrough from the Hall C beam was discovered in the Hall A beamline. Since the Hall C beam polarization has the opposite sign to the Hall A beam polarization, this bleedthrough can result in a large correction to the beam polarization. When the Møller measurements were performed, the bleedthrough from Hall C was measured and corrected. However typically only one Møller measurement was performed at each beam energy, whereas several measurements were made with the Compton polarimeter, which can only measure the polarization of the Hall A beam and the Hall C bleedthrough together.

The bleedthrough from Hall C in Hall A is dependent on the beam currents from the two halls and the Hall A slit position. The Hall A slit can be closed to reduce the bleedthrough from Hall C. Since the Hall A and Hall C currents vary, the bleedthrough also varies. During the second run period, dedicated measurements were performed to measure the Hall C bleedthrough. If the Hall C bleedthrough was more than a few percent, then the Hall A slit was closed to reduce the bleedthrough to an acceptable level.

The corrected beam polarization in Hall A $P_{\rm A}^{corr}$ is determined by

$$P_{\rm A}^{corr} = P_{\rm A}^{pure} - \left(\frac{B}{100}\right)(P_{\rm A}^{pure} - P_{\rm C}) \ , \tag{5.11}$$

where $P_{\rm A}^{pure}$ is the beam polarization in Hall A with the Hall C laser off, and B is the percentage of the Hall C current in Hall A measured by the Hall A BCM. $P_{\rm C}$ is the polarization in Hall A with the Hall A laser off. The polarizations used in Eq. (5.11) are taken from the Møller measurements. The bleedthrough from Hall C was empirically determined from the Hall A current, the Hall C current and the Hall A slit position [74].

There are two cases that had to be considered: with the Hall A slit out and with the

Time Period	Hall A Slit	α	β
Before August Maintenance	OUT	-0.1885	0.431
	IN	-0.01776	10.53 x 10^{-5}
After August Maintenance	OUT	0.0125	0.1902
	IN	-0.01776	8.962 x 10^{-5}

TABLE 5.3: The bleedthrough coefficients for Eqs. (5.12) and (5.13).

Hall A slit partially inserted. The bleedthrough formulas take the following forms:

$$B = \alpha + \beta \cdot R \,, \tag{5.12}$$

for the slit out and

$$B = \alpha + \beta \cdot R \cdot S^2 \,, \tag{5.13}$$

for when the slit is partially closed. The ratio of the Hall C to Hall A current is given by R, and the slit position is denoted by S. The empirically determined fit coefficients are given by α and β, which are listed in Table 5.3. There are two sets of coefficients, since the bleedthrough's dependency changed after the accelerator maintenance period in August 2003. These coefficients provide an accuracy for the bleedthrough calculation to better than 1%. However, the dominant systematic uncertainty comes from the measurement of the polarizations from the Møller polarimeter, which is at the 3% level.

5.3 The Polarized ^{3}He target

Ideally, we would use a free polarized neutron target to study the spin-dependence of the neutron. However the neutron's short half-life of 886.7 $\pm$ 1.9 s [11] and neutral charge make the creation of a free neutron target impractical so that precise spin structure

measurements can be conducted. Instead polarized nuclear targets such as deuterium and ^{3}He have been used as a substitute.

For experiment E97-110, a polarized ^{3}He gas target provides an effective neutron target, since in the ground state configuration the wave function is dominated by the S-wave. In this configuration, the two proton spins in the ^{3}He are paired, so the lone neutron spin is aligned with the spin of the ^{3}He nucleus. This target has been used successfully for several Jefferson Lab Hall A experiments (E94-010 [57], E95-001 [75], E99-117 [76], E97-103 [77] and E01-012 [73]) prior to E97-110. The target has demonstrated reasonable polarizations (35-42%) with electron beam currents up to 15 μA. More details about the Jeffreson Lab polarized ^{3}He target are available in Ref. [78].

5.3.1 Overview of the Polarized Target

A diagram of the polarized ^{3}He target is illustrated in Fig. 5.9. The two chambered target cell is placed in the center of the target system. The top chamber, known as the pumping chamber, resides inside an oven heated to 170° C. The lower target chamber is where the electron beam interacts with the polarized ^{3}He and is centered in two orthogonal sets of Helmholtz coils. The Helmholtz coils produce a 25 Gauss field that can be oriented in any direction (in-plane).

Rubidium (Rb) alkali vapor is optically pumped inside the pumping chamber using circularly polarized light from three 30 W diode lasers, which are tuned to a wavelength of 795 nm. The Rb polarization is then transferred to the ^{3}He nuclei via a spin-exchange process. The laser light is circularly polarized with a series of optical elements, which include a polarizing beam-splitter and quarter-wave plates.

Two independent polarimetry methods are used to reduce the systematic uncertainty

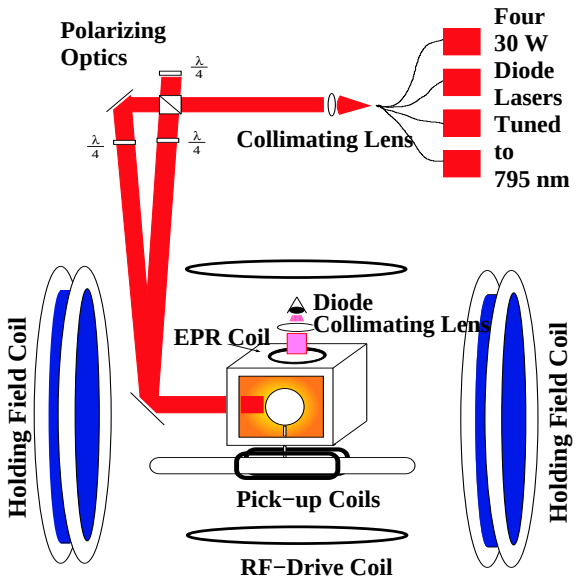

FIG. 5.9: Diagram of the polarized ^{3}He Target system. The transverse Helmholtz coils are not shown to provide clarity.

in the polarization. For the nuclear magnetic resonance (NMR) method, the signal amplitude of ^{3}He nuclei is detected to measure the polarization in the target chamber while the holding field is swept through resonance. The second method of electron paramagnetic resonance (EPR) detects the change in the Zeeman frequency of rubidium when the ^{3}He polarization direction is flipped.

5.3.2 Target Cell

The target cells used in experiment E97-110 are highly pressurized (10−12 atm under operating conditions) glass cells with 130−140 micron thick end windows. The glass walls of the cells were approximately 0.7 mm thick. The thin glass walls were needed to reduce the radiation length of the electrons passing through the glass at scattering angles

of 6° or 9°. The amount of glass traversed by the scattered electron goes as $(\sin\theta_{\rm sc})^{-1}$, where $\theta_{\rm sc}$ is the scattering angle. The two-chambered cells consists of a pumping chamber and a target chamber connected by a transfer tube as shown in Fig. 5.10. The spherical pumping chamber contains the Rb vapor and is where optical pumping occurs. The electron beam passes through and interacts with the polarized ^{3}He in the cylindrical target chamber. Typical cell dimensions are as follows:

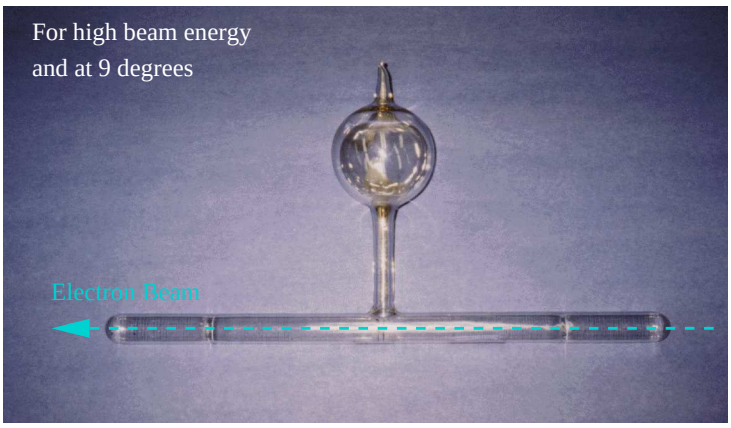

FIG. 5.10: A standard 40 cm long target cell used during E97-110.

- Target chamber diameter: 1.9 cm.
- Transfer tube length: 6 cm.
- Transfer tube diameter: 1.2 cm.
- Pumping chamber diameter: 6.5 cm.

For the low beam energies at 6°, even the thin 0.7 mm walls was not sufficient to reduce the electron's energy loss, so a new cell design was developed that consisted of an asymmetric cone for the downstream part of the target chamber. The "ice cone" cell

is depicted in Fig. 5.11, where the scattered electrons at 6° pass through the thin end windows instead of the glass walls. The exit end window is only 200-250 microns thick suppressing the amount of glass traversed by almost a factor of 30. The length of the new cells were 35 cm long compared to the standard cells. The "ice cone" cell Proteus was used for the first period, and the two standard cells Penelope and Priapus were used for the second period.

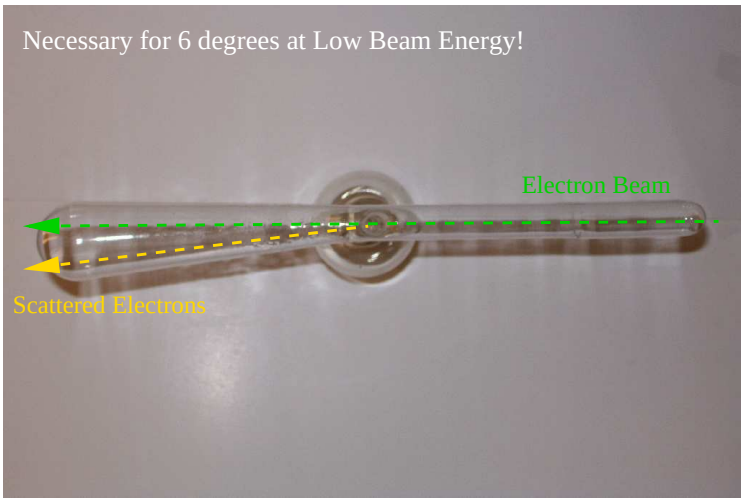

FIG. 5.11: An "ice cone" target cell used during E97-110.

Table 5.4 gives the main characteristics that are crucial in determining the target polarization during operation. The three target cells used during the experiment were characterized at the University of Virginia (UVa) [74]. The pumping chamber volume, transfer tube volume, target chamber volume and total volume of the cell in cm^3 are represented by $V_{\rm pc}$, $V_{\rm tt}$, $V_{\rm tc}$ and $V_{\rm tot}$, respectively. The cell density and lifetime (see Section 5.3.4) are respectively given in units of amagats[1] and hours. The lifetime uncertainties are large,

[1] 1 amagat = 2.6868 $\times$ 10^{19} atoms per cm^3. The unit is dimensionless and is the ratio of the number density of a gas to the number density of an ideal gas at 0° C and 1 atm.

cell	$V_{\rm pc}$	$V_{\rm tt}$	$V_{\rm tc}$	$V_{\rm tot}$	η_0	Lifetime
proteus	89.2	3.1	139.9	236.0	6.85	74
penelope	100.8	4.0	98.6	204.4	8.90	56
priapus	109.9	3.9	96.3	208.7	8.72	54
Uncertainty	0.7%	0.7%	0.7%	0.5%	1.5%	10–20%

TABLE 5.4: Target cell characteristics for experiment E97-110. Cell volumes are given in cm^3, and densities are in amagats at room temperature.

since polarization loss corrections were not applied and the polarization time evolution was not measured over a full lifetime of the cell.

5.3.3 Optically Pumped Rubidium

The ^{3}He nuclei are polarized using a two step process commonly called spin exchange optical pumping (SEOP). The first stage involves optically pumping the rubidium vapor with circularly polarized light. Neglecting the spin of the rubidium nucleus, the energy levels of the rubidium atoms placed in an external magnetic field depend on the quantum numbers of the system and the magnetic field's magnitude. The presence of the external field separates the energy levels. The following notation will be used to designate the different energy levels:

$$\mathrm{N}^{2\mathrm{S}+1}\mathrm{L}_{\mathrm{J}}\,, \tag{5.14}$$

where N represents the electron shell, S is the intrinsic electron spin, L is the orbital angular momentum, and J is the total angular momentum $\vec{L}+\vec{S}$. Other useful quantities are the angular momentum of the rubidium nucleus, denoted as I, the angular momentum of the atom F with $\vec{F}=\vec{I}+\vec{J}$, and $m_{\rm F}$ the z-component of $\vec{F}$.

At Jefferson Lab, right circularly polarized light tuned to 794.8 nm induces a transition of the ^{85}Rb valence electrons from the $5^2\mathrm{S}_{1/2}$ (m = $-1/2$) ground state to the $5^2\mathrm{P}_{1/2}$

(m = +1/2) excited state[2] subject to the selection rule Δm = +1. Left circularly polarized light could also be used, but instead the m = +1/2 ground state sublevel would be excited to the m = −1/2 sublevel. After the electrons are excited, they can decay by emitting photons. These photons are unpolarized and can be reabsorbed by other rubidium atoms, which would reduce the polarization efficiency. A small amount of nitrogen gas is added to the system, which allows a non-radiative decay by absorbing the energy into the nitrogen's rotational and vibrational degrees of freedom via collisions. The excited electron will then decay into either the m = +1/2 or m = −1/2 $5^2S_{1/2}$ state. Since the m = −1/2 state is continuously being pumped, eventually the majority of the atoms will collect in the m = +1/2 state causing the rubidium gas to become magnetically aligned. This process of optical pumping is depicted in Fig. 5.12.

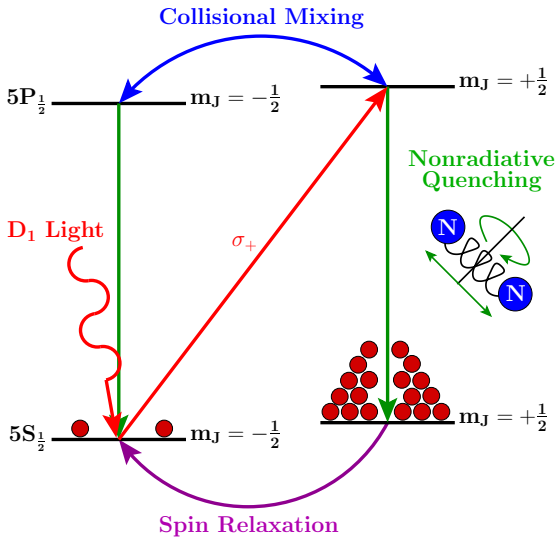

FIG. 5.12: Diagram of the optical pumping technique to polarize rubidium (Rb) vapor. Provided by [79].

[2]The energy splitting between the $S_{1/2}$ and $P_{1/2}$ levels is referred to as the D1 line.

5.3.4 Spin Exchange and Relaxation Rates

The rubidium electrons can transfer their polarization to the ^{3}He nuclei by a hyperfine-like interaction between the Rb electron and ^{3}He nucleus. The transfer of polarization primarily occurs in binary collisions between the Rb atoms and ^{3}He nuclei as illustrated in Fig. 5.13.

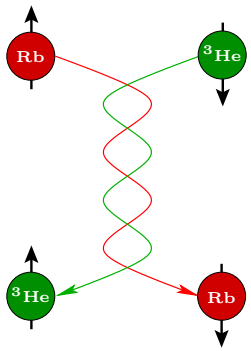

FIG. 5.13: Diagram of spin exchange between a Rb atom and ^{3}He nucleus. Provided by [79].

The spin exchange rate with ^{3}He is given by the formula:

$$\gamma_{\mathrm{SE}} = k_{\mathrm{SE}}[\mathrm{Rb}]\,, \tag{5.15}$$

where k_{SE} is the spin exchange coefficient and [Rb] is the rubidium number density. A factor of two uncertainty has existed for k_{SE}, but recently the spin exchange coefficient was measured and found to have a value of $(6.8 \pm 0.2) \times 10^{-20}$ cm^3/s [80]. The Rb density is given by the Killian formula [81], but a more commonly used formula [82] provides the rubidium density with a 5% accuracy:

$$[\mathrm{Rb}] = \left(10^{26.178-4040/T}\right)/T\,, \tag{5.16}$$

where T is the temperature in Kelvin. For the operating temperature of 170 °C, Eq. (5.16) gives a Rb vapor density of 2.58×10^{14} cm^{-3}, and hence a spin-exchange rate of (16h)$^{-1}$.

This slow exchange rate makes the polarization of ^{3}He via spin exchange an inefficient process.

The time evolution of the ^{3}He polarization is described by

$$P_{^3\mathrm{He}}(t) = \langle P_{\mathrm{Rb}} \rangle \frac{\gamma_{\mathrm{SE}}}{\gamma_{\mathrm{SE}} + \Gamma} \left[1 - e^{-(\gamma_{\mathrm{SE}}+\Gamma)/t}\right] , \tag{5.17}$$

with $\langle P_{\mathrm{Rb}} \rangle$ the volume averaged Rb polarization with $\langle P_{\mathrm{Rb}} \rangle > 90\%$. The ^{3}He nuclear spin relaxation is represented by Γ. Since the spin exchange rate is small, quite a bit of effort is made to minimize this quantity. The relaxation rate can be obtained from a spin-down measurement, where the ^{3}He polarization versus time is measured in the absence of optical pumping and the electron beam. The exponential decay constant τ is called the lifetime of the target cell and is related to the spin relaxation by $\Gamma = \tau^{-1}$. Cell lifetime is one of the primary characteristics that determines the cell's maximum polarization.

Spin Relaxation

The spin relaxation rate can be expressed in terms of the main sources of depolarization:

$$\Gamma = \tau^{-1} = \Gamma_{\mathrm{dipole}} + \Gamma_{\nabla \mathrm{B}} + \Gamma_{\mathrm{wall}} + \Gamma_{\mathrm{beam}} . \tag{5.18}$$

In Eq. (5.18), Γ_{dipole} represents the relaxation due to the ^{3}He-^{3}He magnetic dipole interaction at 23 °C [83] and is expressed as

$$\Gamma_{\mathrm{dipole}} = \frac{[^3\mathrm{He}]}{744} \mathrm{h}^{-1} \tag{5.19}$$

where $[^3\mathrm{He}]$ is the ^{3}He density in amagats. For the typical operating density during E97-110, the dipole relaxation rate was about (70h)$^{-1}$. The authors of Ref. [83] did not provide the analytical form of the temperature dependence. However a parameterization of the temperature dependence was performed [84], which results in a $\sim$ 14% correction to Eq. (5.19) at 170 °C, $\Gamma_{\mathrm{dipole}} \approx$ (80h)$^{-1}$.

The second term in Eq. (5.18) represents the depolarization due to magnetic field gradients:

$$\Gamma_{\nabla \mathrm{B}} = D_{^3\mathrm{He}} \frac{|\nabla B_x|^2 + |\nabla B_y|^2}{B_z^2}\,, \tag{5.20}$$

where $D_{^3\mathrm{He}}$ = 0.28 cm^2/s is the ^{3}He self-diffusion constant, and B_z = 25 G is the holding field. The gradients perpendicular to the holding field are given by ∇B_x and ∇B_y. The gradients are usually kept below 10 mG/cm, which results in a negligible depolarization from this source.

Another source of relaxation is ^{3}He collisions with the glass cell walls. The walls of the cell can contain paramagnetic impurities and microscopic fissures. Unfortunately this aspect of the depolarization is hard to control and depends on the fabrication of the cell, and Γ_{wall} has been seen to vary significantly from one cell to another. The typical high polarization cells at Jefferson Lab have a wall relaxation rate of (90h)$^{-1}$.

Finally the electron beam produces another depolarization effect by ionizing the ^{3}He atoms as it passes through the target. The ^{3}He nucleus can then be depolarized due to a hyperfine interaction with the remaining atomic electron spin. A study of this effect has recently been conducted, and details are available in Ref. [84].

5.3.5 Target Polarimetry

NMR Polarimetry

The technique of adiabatic fast passage (AFP) [85] is utilized in both target polarimetry methods to measure the polarization of the ^{3}He nuclei. In the AFP method, the spins are reversed while keeping the loss in polarization minimal. Nuclear magnetic resonance (NMR) AFP can be classically described for a free particle with spin $\vec{I}$ and magnetic moment $\vec{M} = \gamma \vec{I}$, where γ is the particle's gyromagnetic ratio ($2\pi\times$ 3.243 kHz/G for ^{3}He).

When the particle is placed into a magnetic field, the magnetic moment experiences a torque:

$$\frac{d\vec{M}}{dt} = \gamma \vec{M} \times \vec{H}\,. \tag{5.21}$$

The motion precesses around the magnetic field $\vec{H}$, and we can now consider the system in a rotating frame that rotates at the same frequency $\vec{\omega}$ as the precession. The evolution of the magnetic moment then becomes

$$\frac{\delta\vec{M}}{\delta t} = \gamma \vec{M} \times \left(\vec{H} - \frac{\vec{\omega}}{\gamma}\right)\,, \tag{5.22}$$

and the magnetic field $\vec{H}$ can be replaced with an effective field $\vec{H}_{\rm e} = \vec{H} - \frac{\vec{\omega}}{\gamma}$.

When the NMR measurement is performed, the magnetic field is oriented parallel to the beamline $\vec{H} = H_z\hat{k}$. If the frequency is chosen such that $\omega = \gamma H_0$, the motion of the magnetic moment will vanish. This frequency in a static field is known as the Larmour frequency ω_0. An oscillating RF field $\vec{H}_1 = H_1\cos(\omega t)\hat{i} + H_1\sin(\omega t)\hat{j}$ with a frequency of 91 kHz is then applied perpendicular to the holding field. The effective field can be expressed as

$$\vec{H}_{\rm e} = \left(H_z - \frac{\omega_0}{\gamma}\right)\hat{k} + H_1\hat{i}'\,, \tag{5.23}$$

and the average ^{3}He magnetic moment will align itself with this effective field.

During the NMR measurement, the holding field is swept from 25 G to 32 G through resonance, $\frac{\omega_0}{\gamma}$ = 28.06 G, and back, and the ^{3}He spins follow the effective field. As the field is swept, the spins go from being aligned to anti-aligned with respect to the main holding field, i.e, a spin flip occurs. At resonance, the motion of the spins induces an electromotive force that generates a signal in a pair of pick-up coils placed on both sides of the target chamber. The amplitude of the detected signal is proportional to the transverse

magnetization $M_{\rm T}$:

$$S(t) = M_{\rm T}\frac{\left(\vec{H}_{\rm e}\right)_{\perp}}{|\vec{H}_{\rm e}|} = \frac{M_{\rm T}H_1}{\sqrt{(H(t)-H_0)^2+H_1^2}}\,, \tag{5.24}$$

where H_0 is the holding field at resonance, and $H(t)$ is

$$H(t) = \begin{cases} \alpha t + \beta & \text{if } t < t_{\rm sweep} \\ \beta - \alpha t & \text{if } t_{\rm sweep} < t < 2t_{\rm sweep} \end{cases} \tag{5.25}$$

with α = 1.2 G/s is the sweep rate, β is the starting holding field value (25 G) and $t_{\rm sweep}$ (5.8$\bar{3}$ s) is the length of the sweep through resonance. A typical NMR measurement is shown in Fig. 5.14.

The NMR signal can be fit to Eq. (5.24) with a linear background included. The signal amplitude from the fit is extracted and is proportional to the polarization of the ^{3}He, $P_{\rm He} = k_{\rm NMR}S_{\rm He}$. The constant of proportionality $k_{\rm NMR}$ is dependent on the cell position, density, geometry and the responsiveness of the pick-up coils and related electronics [86]. The NMR constant is determined by calibrating the ^{3}He signal against the thermal polarization of protons in water.

AFP Condition

The holding field sweep must satisfy the AFP conditions to limit the polarization loss during the measurement. The AFP condition requires that the holding field changes slowly enough (adiabatic) so the ^{3}He spins will follow the magnetic field while it is swept, but fast enough so that the spins will not relax during the sweep. These conditions are expressed by:

$$\frac{1}{T_{1\rm r}} \ll \frac{1}{H_1}\frac{dH}{dt} \ll \gamma H_1\,, \tag{5.26}$$

where $T_{1\rm r} \approx$ 435 s [86] is the ^{3}He relaxation rate in the rotating frame, and the magnitude of the RF field is about 90 mG. Hence, the above conditions for ^{3}He are easily met.

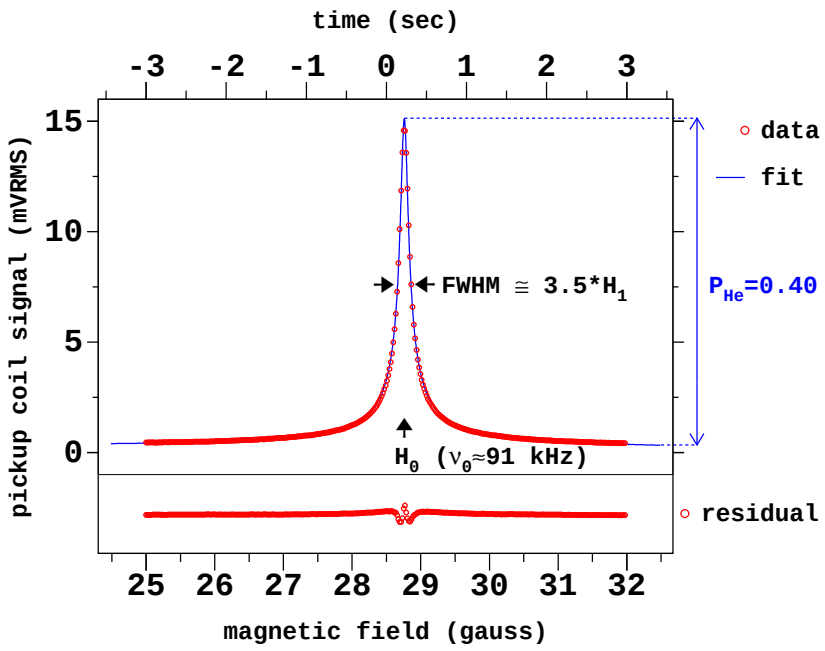

FIG. 5.14: A typical ^{3}He NMR AFP spectrum. Provided by [79].

Water Calibration

The ^{3}He NMR signal is calibrated with a water cell that has similar geometry to the ^{3}He cell. The thermal polarization of water follows the Boltzmann distribution:

$$P_{\rm th} = \tanh \frac{\mu_{\rm p} B}{kT}\,, \tag{5.27}$$

where $\mu_{\rm p}$ = 2.793$\mu_{\rm N}$ is the proton's magnetic moment in nuclear magnetons (3.152 $\times$ 10^{-14} MeV T^{-1}), B is the magnetic field, k is Boltzmann's constant (8.617 $\times$ 10^{-11} MeV K^{-1}) and T is the temperature of the water in Kelvin. At room temperature 295 K and the resonance field, the thermal polarization of water is only $\approx$ 7.40 $\times$ 10^{-9}, so hundreds of measurements are averaged together in order to increase the signal-to-noise ratio. The average value is then used for the calibration.

For the water NMR measurements, the field is swept from 18 to 25 G with the

resonance at 21.37 G, since the gyromagnetic ratio for protons is $2\pi\times$ 4.257 kHz G^{-1}. The RF frequency is the same as that used for the ^{3}He NMR. Since the thermal relaxation time for water is approximately 3 s, which is the same order of magnitude as the length of time that the field is swept, the proton spins relax during the sweep. This affects both the amplitude and shape of the AFP signal, and the signal is now dependent on the speed and direction of the field sweep. The amplitude of the water signal is extracted based on fits to the Bloch equations [85] instead of Eq. (5.24). The constant of proportionality is then related to the ratio of the thermal polarization of protons in water and the water signal amplitude $S_{\rm w}$.

The dominant source of systematic uncertainty in $k_{\rm NMR}$ involves the calculation of the magnetic flux through the pick-up coils. The uncertainty from the flux is mostly due to the measurements in the cell and coil positions relative to each other and results in an uncertainty of $\sim$ 2.0%.

EPR Polarimetry

In the presence of a magnetic field, the Rb F = 3 ground state splits into seven sublevels m_F = -3, -2, ..., 2, 3. The Zeeman splittings between the different sublevels are given by the electron paramagnetic resonance (EPR) frequency $\nu_{\rm EPR}$, which is proportional to the magnetic field:

$$\nu_{\rm EPR} = k_{\rm z} B\,, \tag{5.28}$$

with $k_{\rm z}$ = 0.466 MHz G^{-1}. The presence of the polarized ^{3}He nuclei generates an additional small magnetic field (100 mG) in addition to the main holding field. The EPR method of polarimetry measures the small increase in the Zeeman splittings due to the polarized ^{3}He. The EPR frequency can be decomposed into two parts; the first part ν_0 is proportional to the holding field, and the second $\delta\nu_{\rm EPR}$ is proportional to the ^{3}He polar-

ization:

$$\nu_{\rm EPR} = \nu_0 \pm \delta\nu_{\rm EPR}\,. \tag{5.29}$$

The sign indicates that the ^{3}He spin is either anti-parallel (+) or parallel ($-$) to the external magnetic field.

The small component $\delta\nu_{\rm EPR}$ is measured by applying a small RF field to excite the $m_F = -3$ to $m_F = -2$ transition of the ground state sublevels. This transition results in an increase in the number of $m_F = -2$ Rb atoms that can be pumped by the laser light. When these atoms decay back to the ground state, a corresponding increase occurs in the number of photons emitted, which can then be detected in a photodiode. Since the cell is illuminated with D1 light from the lasers, a D2[3] filter is used to instead detect the increase in D2 light. During the EPR measurement, the ^{3}He spins are flipped by sweeping the frequency through resonance while the resonance frequency is monitored. The change in EPR frequency is shown in Fig. 5.15 for a typical EPR measurement. Initially the ^{3}He spins will be aligned with the holding field, and after the spin flip, they are anti-aligned with the field. A precise measurement of the polarization can be obtained by measuring the frequency, and the polarization $P_{\rm He}$ is extracted from the change in EPR frequency:

$$\Delta\nu_{\rm EPR} = \frac{8\pi}{3}\frac{\mu_0}{4\pi}\left(\frac{d\nu}{dB}\right)\kappa_0\mu_{\rm He}\left[^3{\rm He}\right]P_{\rm He}\,, \tag{5.30}$$

where $\mu_{\rm He}$ = 1.155 $\times$ 10^{-13} MeV T^{-1} is the magnetic moment of ^{3}He, and κ_0 is a temperature dependent factor measured in Ref. [87]:

$$\kappa_0 = 4.52 + 0.00934T(^\circ C)\,. \tag{5.31}$$

The EPR calibration constant $k_{\rm EPR}$ is defined as

$$k_{\rm EPR} = \frac{8\pi}{3}\frac{\mu_0}{4\pi}\left(\frac{d\nu(F,\Delta m)}{dB}\right)\kappa_0\mu_{\rm He}\left[^3{\rm He}\right]\,, \tag{5.32}$$

[3]The energy splitting between the ground state $S_{1/2}$ and $P_{3/2}$ levels is referred to as the D2 line.

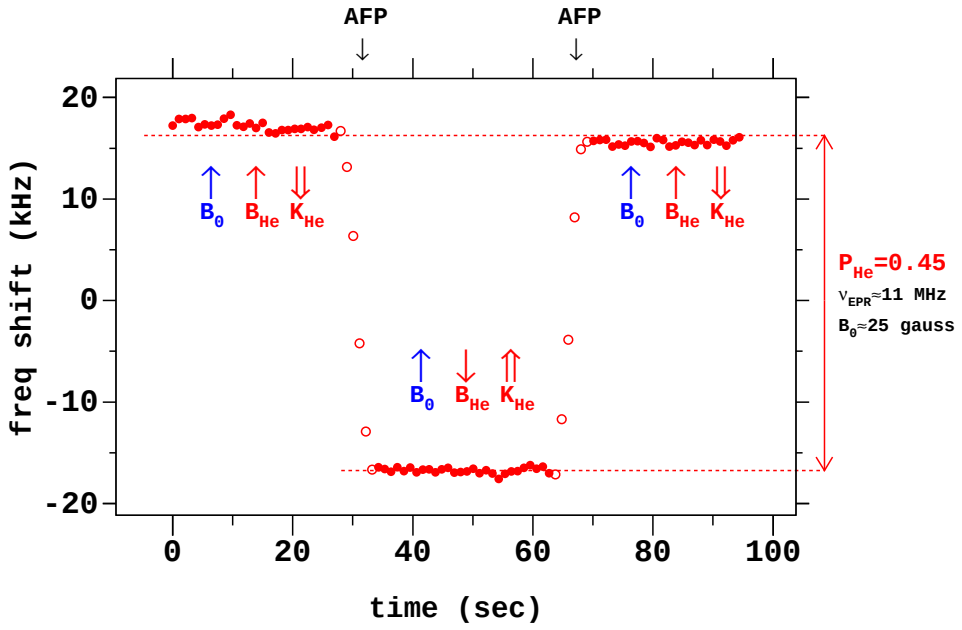

FIG. 5.15: A typical EPR resonance plotted versus time. Provided by [79].

and the derivative $\frac{d\nu(F,\Delta m)}{dB}$ for the $m_F = -3$ to $m_F = -2$ transition was obtained from Ref. [88]:

$$\frac{d\nu(3,-2\leftrightarrow -3)}{dB} = 0.4671 + 7.4\times 10^{-4}B\,, \tag{5.33}$$

where B is the magnetic field magnitude in G, and the derivative has units of MHz per G. The dominant systematic uncertainty from EPR is from κ_0 with a value of 1.5%. Of course, the EPR measurement provides the polarization in the pumping chamber, so the polarization gradient between the two chambers needs to be calculated to determine the target chamber polarization. The details for the determination of the polarization gradient are described in Ref. [84]. The effect for E97-110, which includes depolarization from the electron beam, was estimated to be a 5% relative difference between the pumping and target chamber polarizations using a 10 μA beam and a cell lifetime of 40 hr.

5.3.6 E97-110 Target Performance

During the experiment, NMR and EPR measurements were done back-to-back every 4–6 hours. The target polarimetry analysis is first performed for the individual measurements, and then a polarization for each run is determined by using linear interpolations between the measurements. In Fig. 5.16, the target polarization (interpolated for each run) is shown from the average of the NMR and EPR measurements [79]. The vertical dashed line divides the data between the two target cells used for the second period. The relative uncertainty on the target polarization is about 7.5%. This uncertainty is about a factor of two larger than normal due to a discrepancy between the two polarimeters. The discrepancy may be related to gradient effects at the target from the septum magnet. In this case, the EPR measurements are more reliable and have a total uncertainty $< 4\%$. The discrepancy between NMR and EPR is currently under investigation [79].

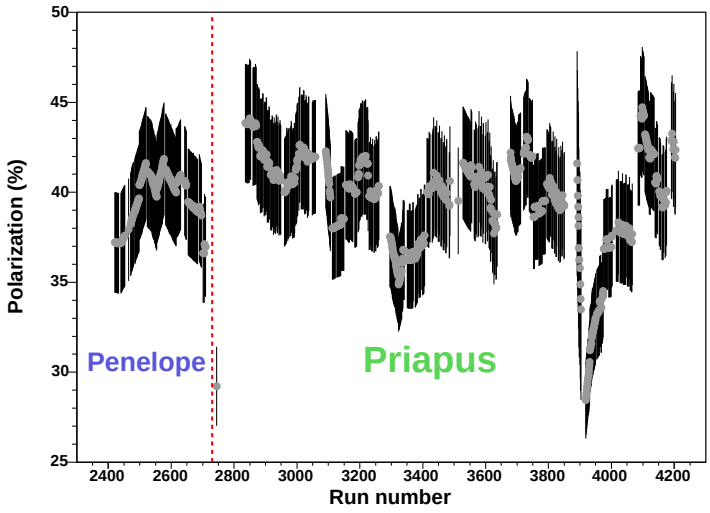

FIG. 5.16: The target polarization versus run number for E97-110. The error bars include the relative 7.5% uncertainty due to the discrepancy between the NMR and EPR results.

CHAPTER 6

The Hall A Spectrometers

In this chapter, the Hall A spectrometers and their detector packages are presented. The optimization of the spectrometer optics for experiment E97-110 is also discussed.

6.1 High Resolution Spectrometers

Hall A contains a nearly identical pair of magnetic spectrometers known as the high resolution spectrometers (HRS) [67]. Their main characteristics are summarized in Table 6.1. For the reminder of this document, the two spectrometers will be referred to as HRS-L and HRS-R. The spectrometers transport charged particles in a small range of momenta and scattering angles to their respective detector packages. Both HRSs contain three quadrupoles and a dipole magnet in a QQDQ configuration as illustrated in Fig. 6.1. The three superconducting quadrupoles referred to as Q1, Q2 and Q3 provide focusing: Q1 focuses in the vertical plane and Q2 and Q3 in the transverse plane.

The superconducting dipole has a vertical bend of 45°, which provides the momen-

tum resolution at the 10^{-4} level. The magnetic field in the dipole magnet determines the momentum of the electrons that reach the detector package. The spectrometer's central momentum is related to the magnetic field of the dipole by

$$P_0 = \sum_{i=1}^{3} \Gamma_i B_0^i, \tag{6.1}$$

where Γ_i are the spectrometer constants, and B_0 is the dipole magnetic field. These constants were determined for both HRSs over their full momentum range [89]. Table 6.2 provides the constants for the spectrometers.

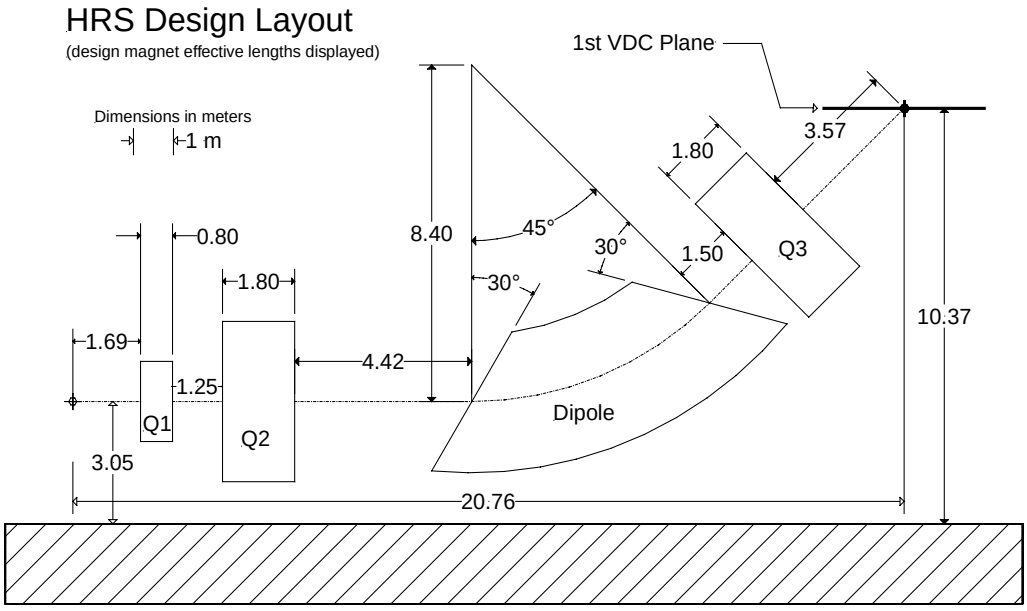

FIG. 6.1: Magnet configuration for the Hall A HRS spectrometers. In the diagram, all units are in meters, and the effective lengths of the magnets are displayed. Reproduced from [67].

Bending angle	45°
Optical length	23.4 m
Momentum range (HRS-L)	0.3 – 4.0 GeV/c
Momentum range (HRS-R)	0.3 – 3.2 GeV/c
Momentum resolution	1x10^{-4}
Dispersion at the focus (D)	12.4 m
Radial linear magnification (M)	–2.5
Angular Range (HRS-L)	12.5 – 150°
Angular Range (HRS-R)	12.5 – 130°
Angular acceptance (horizontal)	$\pm$ 30 mrad
Angular acceptance (vertical)	$\pm$ 60 mrad
Angular resolution (horizontal)	0.5 mrad
Angular resolution (vertical)	1.0 mrad
Solid angle at δ = 0, y_0 = 0	6 msr
Transverse length acceptance	$\pm$5 cm
Transverse position resolution	1 mm

TABLE 6.1: The characteristics [67] of the standard Hall A spectrometers.

	Γ_1 (MeV/T)	Γ_2 (MeV/T^2)	Γ_3 (MeV/T^3)
HRS-L	2702 $\pm$ 1	0	-1.6 $\pm$ 0.4
HRS-R	2698 $\pm$ 1	0	-1.6 $\pm$ 0.4

TABLE 6.2: The spectrometer constant coefficients for HRS-L and HRS-R.

6.2 Septum Magnets

A few experimental groups in Hall A were interested in forward angle measurements between 6° and 12.5°. However, the spectrometers have a minimum achievable lab angle of 12.5°. The main reason for this limitation is that Q1 cannot be moved closer to the beamline without hitting the beam pipe. A proposal was approved that added a superconducting dipole in front of each spectrometer to reach angles down to 6°. The schematic setup of the HRS with septum is shown in Fig. 6.2

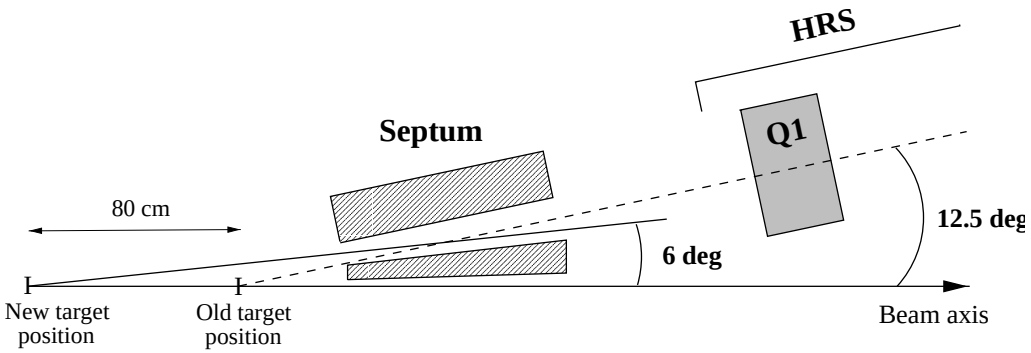

FIG. 6.2: A schematic diagram of the septum magnet + HRS spectrometer with the target moved 80 cm upstream.

Horizontal-bending septum magnets [62] were designed and fabricated for experiment E94-107, Hypernuclear Spectroscopy [90]. They were designed so that the performance of the HRS would not be degraded by the addition of the magnets. The goal was to have a general purpose device so particles with momenta up to 4 GeV/c and angles between 6° and 12.5° were detectable in the spectrometers. The HRS + septum spectrometer would have a 4.7 msr angular acceptance and momentum resolution $< 2\text{x}10^{-4}$.

The target was moved 80.0 cm upstream to accommodate the new magnets. With the septum magnet + HRS spectrometer the target appears situated on the optical axis of the two spectrometers. In Table 6.3 the dimensions of the septum magnets are summarized.

Length	88.0 cm
Height of the gap	25.0 cm
Width of gap (entrance)	10.4 cm
Width of gap (exit)	18.4 cm
Angular acceptance	4.7 msr
Magnetic length	84.0 cm

TABLE 6.3: Dimensions of the septum magnets [91].

For experiment E97-110, we commissioned the HRS-R septum magnet at central

scattering angles of 6° and 9°. Since the HRS-L septum was unavailable, the left spectrometer instead detected scattered electrons from a carbon foil target. This target was placed $\sim$ 90.0 cm downstream from the target location for the HRS-R + septum spectrometer. The data from HRS-L was used to monitor false asymmetries and the beam luminosity. The reminder of this document will only address data from HRS-R.

6.3 Detector Package

The detector packages for the two spectrometers were almost identical during E97-110 and were utilized for electron detection. Here only the HRS-R package will be discussed. The configuration is shown in Fig. 6.3. A pair of vertical drift chambers determine the particle trajectory for the target reconstruction and, coupled with the dipole, provides the momentum resolution. Then the particles pass through a pair of plastic scintillator planes, which form the trigger for the data acquisition. Particle identification (PID) is provided by a gas Čerenkov sandwiched between the scintillator planes and a two-layer electromagnetic calorimeter. The main difference between the HRS-L and HRS-R packages is that in the second layer of HRS-R calorimeter, the blocks are oriented parallel to the particle tracks, whereas in the HRS-L calorimeter the blocks in the second layer are oriented perpendicular to the tracks as shown in Fig. 6.5.

6.3.1 Vertical Drift Chambers

The vertical drift chambers (VDC) [92] provide tracking information that result in good position and angular resolution. Each spectrometer contains two chambers with two wire planes in a standard UV configuration, which are inclined at an angle of 45° with

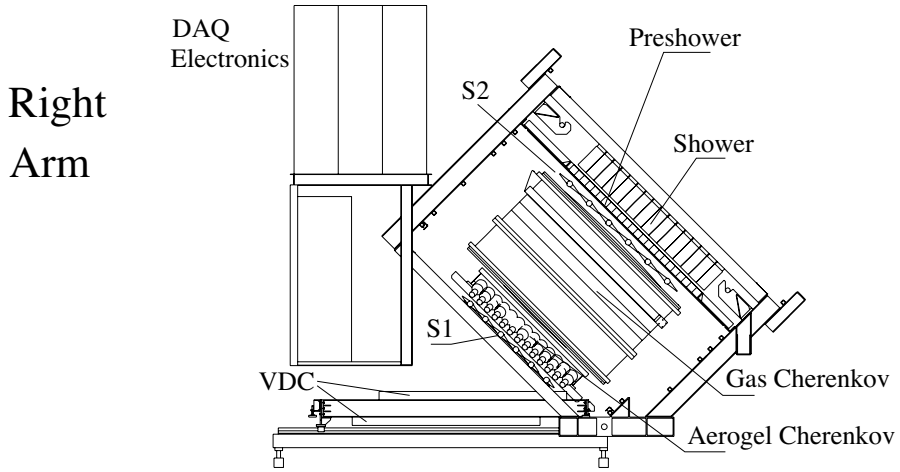

FIG. 6.3: Detector package for HRS-R. Note the aerogel Čerenkov was not used or present in the detector stack during E97-110. Reproduced from [67].

respect to the dispersive and non-dispersive directions. In the UV configuration, the wires of each successive plane are orthogonal to each other [67]. The first wire plane that the particles traverse is located at the spectrometer focal plane. The distance between like wire planes is 335 mm as shown in Fig. 6.4, and each plane contains 368 active sense wires.

For the VDCs, the process of ionization is utilized where the incident particle collides with gas molecules creating electron-ion pairs. An electric field is applied in the chamber with gold-plated Mylar planes powered at -4.0 kV. The chambers are filled with a 62/38 gas mixture of argon and ethane. The argon provides the ionizing medium, and the ethane absorbs the produced photons from ionization. The gas continuously flows at 5 liters per hour per chamber to provide a homogeneous dry gas environment. The ionized electrons drift along the electric field lines. When the electron is near a wire, the electron

accelerates due to the radial electric field, which then can produce many secondary ionizations. The net result of the avalanche of electrons produces a detectable signal (hit) on the wire.

By design, electrons that traverse the VDCs with a nominal angle of 45° will fire between four to six wires (cluster) per plane providing accurate reconstruction of the electron's trajectory. At the extreme angle of 52°, three wires will still fire. The trajectory is extracted by using timing information from the time-to-digital converters (TDCs) to determine the drift distances for each wire in a cluster. The cross-over point of the track is then determined by a linear fit of drift distances versus wire position. Finally the track positions and angles are extracted from the data. The position and angular resolution in the focal plane are approximately 100 μm and 0.5 mrad, respectively.

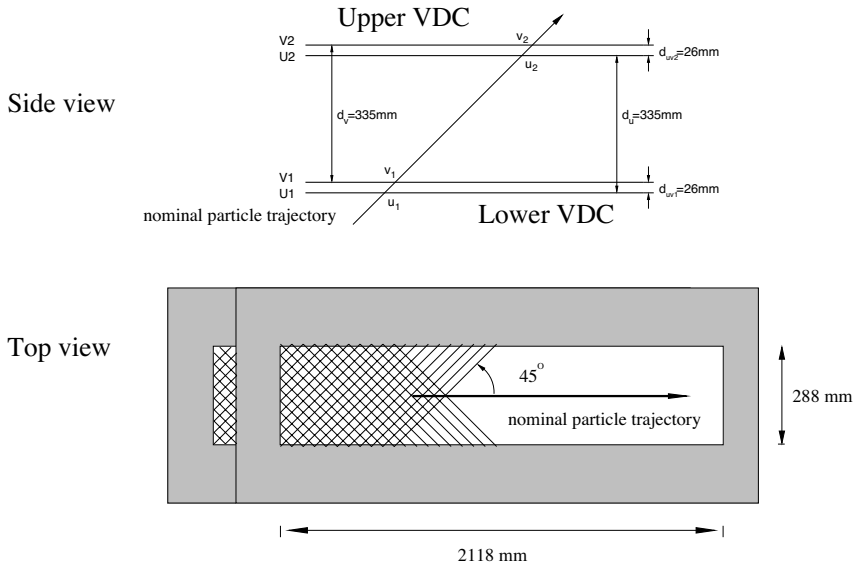

FIG. 6.4: Schematic diagram of the Hall A vertical drift chambers. Reproduced from [67].

6.3.2 Scintillators

The HRS-R spectrometer contains two plastic scintillator planes (S_1 and S_2) separated by 2 m to trigger the data acquisition. Each plane has six 5 mm thick paddles, and each paddle is viewed by two photomultipliers (PMT), one at each end. The edges of two adjacent paddles overlap to avoid gaps between the paddles. The timing resolution for each plane is about 0.3 ns.

The criteria for the main trigger is as follows:

- The left and right PMTs on a paddle of S_1 both fire.
- The left and right PMTs on a paddle of S_2 both fire.
- The track is reasonably close to 45°.

The third requirement implies that if an event triggers paddle n on S_1, then it must trigger paddle n or $n \pm 1$ on S_2. The main trigger for the right spectrometer is referred to as T_1. A secondary trigger, T_2, is used to measure the scintillator efficiency. The T_2 trigger is exclusive to T_1 and formed by requiring one of the scintillator planes to have fired and a signal was detected by the Čerenkov detector. These are possibly good events that one of the trigger planes failed to detect.

The triggers are then sent to the trigger supervisor (TS), which determines if the data acquisition (DAQ) should record the event. When the event rate is high, the DAQ system cannot record all the events. The fraction of events recorded by the DAQ is represented by a quantity called the livetime LT or deadtime $DT = 1 - LT$. Deadtime comes mostly from computer data processing and can be decreased by prescaling the events with a prescale factor ps at the TS; for every ps events, only one is sent to the DAQ system.

Electronic deadtime is also present due to the response of the detectors. However, this is negligible compared to the computer deadtime.

The livetime is event type and helicity dependent and is determined by dividing the total number of triggers accepted by the DAQ system $T_{\rm i}^{\rm acc}$ by the number of triggers $T_{\rm i}$ recorded by scalers:

$$LT_{\rm i}^{\pm} = \frac{ps_{\rm i} T_{\rm i}^{\rm acc,\pm}}{T_{\rm i}}, \tag{6.2}$$

where i = 1 or 2 is the event type, $ps_{\rm i}$ is the prescale factor for event type i and $\pm$ denotes the helicity.

The speed of the particles β can also be measured by using the time-of-flight between S_1 and S_2.

6.3.3 Gas Čerenkov Detector

The gas Čerenkov detector [93] is used for particle identification. For E97-110, the Čerenkov separated electrons from other negatively charged particles such as pions. The detector is based on the detection of Čerenkov light, which is produced when a particle is traveling faster than the speed of light in a medium. The threshold for production of Čerenkov light is

$$\beta \geq \frac{1}{n}, \tag{6.3}$$

where n is the index of refraction of the medium. The threshold's dependency on the particle's velocity, makes this a very effective method to distinguish between particles with different masses. Since electrons and pions have a sizable mass difference, the index

of refraction can be chosen so that only electrons will trigger the detector over the desired momentum range.

The gas Čerenkov is mounted between the two scintillator planes and filled with atmospheric pressure CO_2 with an index of refraction of 1.0004. The threshold momentum $P_{\rm th}$ for different particle species can be calculated from:

$$P_{\rm th} = \frac{mc}{\sqrt{n^2-1}}, \tag{6.4}$$

where m is the particle's mass. The electron threshold is 18 MeV/c; whereas, the threshold for pions is 4.87 GeV/c, which is well above the momentum range (0.4 GeV/c to 3.2 GeV/c) for this experiment.

The HRS-R Čerenkov detector has a pathlength of 150 cm and contains ten spherical mirrors that reflect the Čerenkov radiation onto a set of ten PMTs. The signals from the PMTs are then sent to analog-to-digital converters (ADC) and summed. The sum represents the total measured light produced by the particle.

Unfortunately pions can cause a sizable background by knocking out electrons from material before reaching the detector. These electrons, known as δ-electrons, may produce Čerenkov light and hence contribute to the ADC signal. These events are removed with the aid of a lead-glass calorimeter.

6.3.4 Electromagnetic Calorimeter

The electromagnetic calorimeter utilizes pair production and *bremsstrahlung* radiation, which is the emission of radiation from scattering in the electric field of a nucleus. When a high energy particle traverses a dense material, an electromagnetic cascade of photons and electron-positron pairs is generated. The light emitted from the cascade can

then be detected by PMTs.

The HRS-L and HRS-R calorimeters consist of two segmented layers as shown in Fig. 6.5. The particles enter the detector through the bottom of the figure. The first layer is oriented perpendicular to the particle trajectories and composed of 48 (24 x 2), 10 cm x 10 cm x 35 cm lead-glass blocks; whereas the second layer is oriented parallel to the trajectories and composed of 80 (16 x 5), 15 cm x 15cm x 35 cm lead-glass blocks. Each block is viewed by a PMT. The HRS-R shower detector is a total absorption calorimeter, since it is sufficiently thick to contain the cascade for the spectrometer's momentum range.

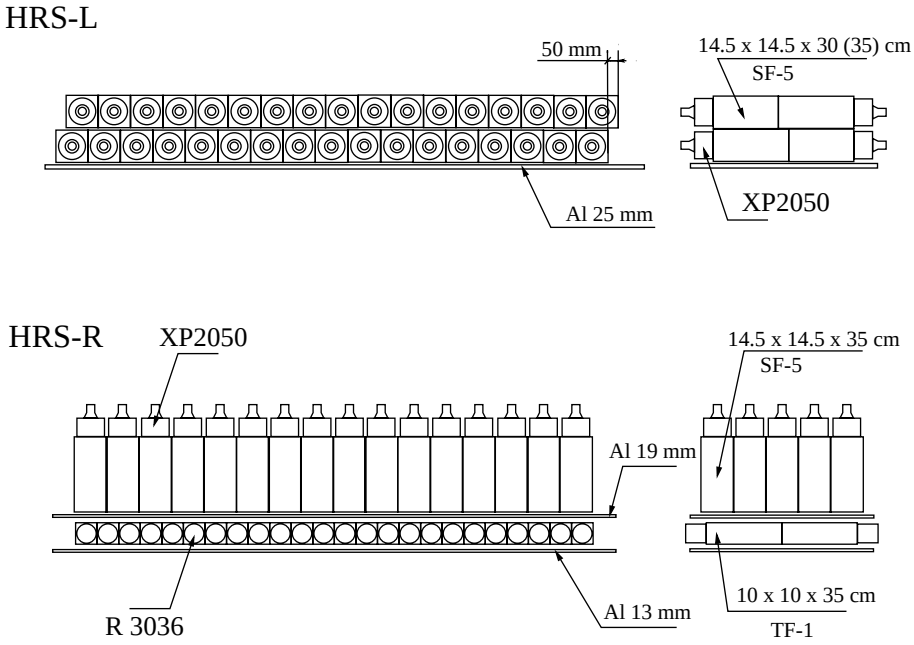

FIG. 6.5: The electromagnetic calorimeter in the HRS-L (top) and HRS-R (bottom). Reproduced from [67].

6.4 Spectrometer Optics

The target coordinates of the detected particles are reconstructed from the focal plane coordinates with a set of optics matrix elements. These matrix elements have been tested and shown to be stable over the full momentum range of both spectrometers. The addition of the septum magnet to HRS-R required a careful study to determine the changes to the optical properties of the spectrometer. To this end, optics calibration data were acquired over a large range of the right spectrometer's momentum range for both angles. This section describes the calibration procedure used to determine the optics matrix elements for experiment E97-110.

6.4.1 Coordinate Systems

In this section, an overview of the target and focal plane coordinates will be presented. For a detailed description of the Hall A coordinate systems refer to Ref. [94]. When an event is detected by the VDCs, two angular and two spatial coordinates are measured. The particle's position and the tangent of the angle made by its trajectory projected onto the dispersive axis are given by $x_{\rm det}$ and $\theta_{\rm det}$ respectively. Analogous quantities projected onto the non-dispersive axis are given by $y_{\rm det}$ and $\phi_{\rm det}$ respectively. Focal plane coordinates are calculated by correcting for detector offsets from the ideal central ray of the spectrometer. These coordinates are then used to determine the target coordinates and relative momentum ($\theta_{\rm tg}$, $\phi_{\rm tg}$, $y_{\rm tg}$, and δ) of the particle by using the optics matrix elements. δ is defined as

$$\delta = \frac{P - P_0}{P_0} \tag{6.5}$$

where P is the particle's measured momentum and P_0 is the spectrometer central momen-

tum.

Figure 6.6 shows a diagram of the target coordinate system (TCS) for the left spectrometer. The z-axis is defined by a line passing through the midpoint of the central sieve slit hole. The z-axis is perpendicular to the sieve slit surface and points toward it. The sieve slit is a 5 mm thick tungsten block used in the calibration of the optics matrix elements. When the spectrometer and sieve slit offsets are zero, the z-axis passes through the hall center, and this point is the origin of the TCS. In this ideal case, L is the distance from the hall center to the midpoint of the sieve slit central hole. D is the horizontal offset of the spectrometer from the hall center. The $y_{\rm tg}$ axis is parallel to the sieve surface in the transverse plane, while the $x_{\rm tg}$ axis points vertically down in the dispersive plane. The tangent of the in-plane angle and out-of-plane angle with respect to the central trajectory are given by $\phi_{\rm tg}$ and $\theta_{\rm tg}$ respectively, and Θ_0 is the central angle of the spectrometer.

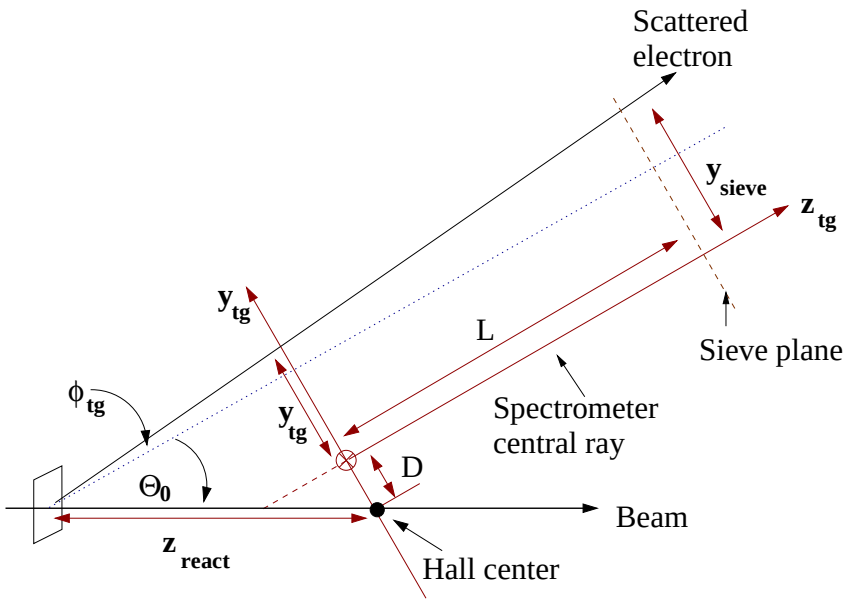

FIG. 6.6: Target coordinate system for electron scattering from a thin foil target. The $x_{\rm tg}$ coordinate is not shown, since it is the vertical displacement and points into the page.

6.4.2 Optimization Method

The optics matrix elements link the focal plane and target coordinates. The relationship between the coordinates is shown in Eq. (6.6) for the first-order approximation without the septum magnet.

$$\begin{bmatrix} \delta \\ \theta \\ y \\ \phi \end{bmatrix}_{\rm tg} = \begin{bmatrix} \langle\delta|x\rangle & \langle\delta|\theta\rangle & 0 & 0 \\ \langle\theta|x\rangle & \langle\theta|\theta\rangle & 0 & 0 \\ 0 & 0 & \langle y|y\rangle & \langle y|\phi\rangle \\ 0 & 0 & \langle\phi|y\rangle & \langle\phi|\phi\rangle \end{bmatrix} \begin{bmatrix} x \\ \theta \\ y \\ \phi \end{bmatrix}_{\rm fp} \tag{6.6}$$

The mid-plane symmetry of the spectrometers requires the null (zero) matrix elements. However the addition of the septum magnet breaks mid-plane symmetry, and the full matrix, Eq. (6.7), was optimized up to fourth order for E97-110.

$$\begin{bmatrix} \delta \\ \theta \\ y \\ \phi \end{bmatrix}_{\rm tg} = \begin{bmatrix} \langle\delta|x\rangle & \langle\delta|\theta\rangle & \langle\delta|y\rangle & \langle\delta|\phi\rangle \\ \langle\theta|x\rangle & \langle\theta|\theta\rangle & \langle\theta|y\rangle & \langle\theta|\phi\rangle \\ \langle y|x\rangle & \langle y|\theta\rangle & \langle y|y\rangle & \langle y|\phi\rangle \\ \langle\phi|x\rangle & \langle\phi|\theta\rangle & \langle\phi|y\rangle & \langle\phi|\phi\rangle \end{bmatrix} \begin{bmatrix} x \\ \theta \\ y \\ \phi \end{bmatrix}_{\rm fp} \tag{6.7}$$

For each of the target variables, a tensor (a set of matrix elements for a target quantity) exists: Y_{jkl}, T_{jkl}, P_{jkl}, D_{jkl}. These tensors are polynomials in $x_{\rm fp}$ and relate the two coordinate systems. For example, the relationship for $\theta_{\rm tg}$ is given by

$$\theta_{\rm tg} = \sum_{j,k,l} T_{jkl} \theta_{\rm fp}^{j} y_{\rm fp}^{k} \phi_{\rm fp}^{l} \tag{6.8}$$

$$T_{jkl} = \sum_{i=0}^{m} C_i x_{\rm fp}^{i} \tag{6.9}$$

where the C_i are the optics matrix elements for the corresponding target coordinate. Similar expressions exist for $\phi_{\rm tg}$, $y_{\rm tg}$, and δ. The indices indicate the power of the focal plane variables. The matrix elements are determined by χ^2 minimization of the aberration functions,

$$\Delta(W) = \sum_s \left[\frac{W - W^0}{\sigma_W^s}\right]^2, \tag{6.10}$$

where W is $\theta_{\rm tg}$, $\phi_{\rm tg}$, $y_{\rm tg}$, or δ. This process compares the reconstructed events (W) to the nominal target foil and sieve slit positions (W^0), which are known from the experiment's surveys.

Eqs. (6.11)–(6.13) give the interaction position along the beam, known as $z_{\rm react}$, and the horizontal and vertical sieve slit positions, $y_{\rm sieve}$ and $x_{\rm sieve}$. These variables are determined from the reconstructed target quantities and are uniquely determined for a set of foil targets and a sieve slit.

$$z_{\rm react} = -(y_{\rm tg} + D)\frac{\cos(\tan^{-1}\phi_{\rm tg})}{\sin(\Theta_0 + \tan^{-1}\phi_{\rm tg})} + x_{\rm beam}\cot(\Theta_0 + \tan^{-1}\phi_{\rm tg}) \tag{6.11}$$

$$x_{\rm sieve} = x_{\rm tg} + L\theta_{\rm tg} \tag{6.12}$$

$$y_{\rm sieve} = y_{\rm tg} + L\phi_{\rm tg} \tag{6.13}$$

The TCS vertical position $x_{\rm tg}$ is determined from the vertical beam position ($y_{\rm beam}$), spectrometer vertical offset, $\theta_{\rm tg}$, and $z_{\rm react}$.

6.4.3 Experimental Technique

Required Data

The optimization procedure is performed on a set of data that covers the entire acceptance of the spectrometer in $\phi_{\rm tg}$, $\theta_{\rm tg}$, $y_{\rm tg}$, and δ. The required data includes:

- A five step scan of the ^{12}C elastic peak that covers the $\pm$ 4.5% spectrometer momentum acceptance.
- A set of thin ^{12}C foils that cover the $y_{\rm tg}$ acceptance.
- A sieve slit collimator with well defined horizontal and vertical positions that cover the angular acceptance of the spectrometer.

For E97-110, the acceptance of $z_{\rm react}$ was $\pm$ 20 cm. Typically nine target foils are used to acquire optics data, but at 6° and 9°, fewer foils were used (3 and 5) due to the reduced resolution at small angles. The carbon foils used for E97-110 had a thickness of 10 mils (0.0254 cm). For elastic electron scattering from carbon, a scan (across the focal plane) of the elastic peak was performed at relative momenta of +3%, +2%, 0%, –2%, and –4%. Due to the lack of statistics, +4% was not used.

Figure 6.7 shows a diagram of the thin sieve slit used to take collimator data. The sieve has 49 holes that are arranged in a grid pattern (7 x 7). Two of the holes are 2.7 mm in diameter, and the remaining holes are 1.4 mm in diameter. The large holes are used to determine the orientation of the image at the spectrometer focal plane. Compared with the standard spectrometer sieve slit, the horizontal distance between sieve slit holes increases further away from the beamline. The four columns closest to the beamline are spaced 0.48 cm apart. The spacing after the fourth column increases so that the columns are then 0.6 cm apart. The vertical spacing between the holes is 1.3 cm.

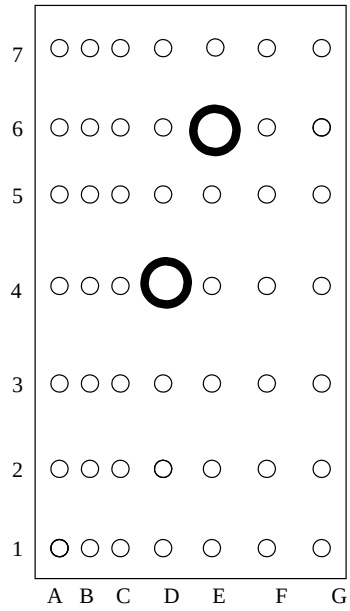

FIG. 6.7: Geometric confi guration of the thin sieve slit used during E97-110. The labels on the rows and columns are for convenience during the optimization procedure. Column A is closest to the beamline.

The beam energies and foil locations are given in Table 6.4 for the optics data acquired at 6° and 9°. The sign convention used for the foil locations is negative for a foil located upstream from the hall center and positive for a foil located downstream. A 20 cm downstream foil was not used at 6° due to the lack of acceptance at this location. At 9°, data were taken with the ± 20 cm foils, however, these foils were not included in the optimization due to a lack of statistics. The 9°, 3.319 GeV data were not acquired at the elastic setting due to the momentum limitation of the right spectrometer. Quasielastic data were acquired with a thicker sieve slit to avoid elastic events that scatter through part of the collimator and clear the spectrometer acceptance at lower momentum.

Survey Requirements

Determination of the ideal $z_{\rm react}$ for each foil, $x_{\rm sieve}$, and $y_{\rm sieve}$ positions for each hole require precise knowledge of the target position, spectrometer displacement from its

Angle	Beam Energies (GeV)	Foil Locations (cm)
6°	1.096, 2.134, 2.844	–20, 0, +10
9°	1.147, 2.235, 3.319	–20, –10, 0, +10, +20

TABLE 6.4: Optics data acquired for E97-110.

Angle	Sieve	L (mm)	Horizontal Offset (mm)	Vertical Offset (mm)
6°	Thin	799.8	0.1	2.0
9°	Thin	798.9	0.3	1.8
9°	Thick	798.6	–0.4	2.0

TABLE 6.5: Sieve slit position and horizontal and vertical offsets from the central hole's ideal position.

ideal position, the position of the sieve slit central hole, and location of the beam position monitors (BPM). These positions and their offsets from nominal positions are determined from survey information [95].

Typically the horizontal spectrometer offset is an important correction that needs to be made in order to determine the nominal sieve slit positions. For the experiment, the septum magnet was tuned to center the $y_{\rm tg}$ position, so the spectrometer offset was unimportant.

The sieve slit survey information is used to calculate the offsets in $x_{\rm sieve}$ and $y_{\rm sieve}$ from their ideal positions for the midpoint of the central hole. The offsets and distance from the hall center to the central hole, L, are given in Table 6.5. The horizontal and vertical positions of the sieve slit holes are then determined from these offsets and the distances between the rows and columns given in the previous section.

During E97-110, there were five target positions: the polarized ^{3}He cell, a single ^{12}C foil, a ^{12}C multi-foil, empty, and reference cell. Only the polarized and reference

Cell	Target	Δx (mm)	Δz (mm)
Penelope	Polarized ^{3}He	0.3	–1.0
	Single ^{12}C	0.1	–0.7
	Multi-foil ^{12}C	0.0	–0.6
	Reference Cell	–0.3	0.2
Priapus	Polarized ^{3}He	0.2	–1.3
	Single ^{12}C	0.2	–1.1
	Multi-foil ^{12}C	0.2	–1.0
	Reference Cell	0.1	–0.4

TABLE 6.6: The target position offsets from the hall center. The carbon foil offsets are determined by linear interpolation, and the offsets for the target cells are from the target survey.

cell positions were surveyed. The positions of the other targets were determined from the survey numbers and from the target ladder specifications. After the target positions were determined, a linear interpolation between the polarized and reference cells was used to determine the foil position offsets from the hall center. The offsets are given in Table 6.6. Only the offset along the beamline, Δz, is important in the optimization process, since this offset determines the nominal position for each of the carbon foils. The vertical offset, Δy, was effectively zeroed during the target survey.

The beam position is determined by the BPMs, which are calibrated with the superharps [67]. The superharp and BPM survey information are used in the BPM calibration procedure. The details of the calibration can be found in Ref. [96]. For each event, the horizontal and vertical beam positions ($x_{\rm beam}$ and $y_{\rm beam}$) are recorded. In the optimization, the beam positions are used to calculate the nominal target coordinates.

6.4.4 Optimization Routine

The optics matrix elements are determined by a C++ optimization routine referred to as OPTIMIZE++. In this section, I will provide a brief overview of the procedure used to perform the optics calibration. A more detailed user manual can be found in Ref. [94].

Algorithm

OPTIMIZE++ provides the user the ability to test a current database or to optimize the matrix elements. The general procedure to perform the optimization involves the following steps:

- Analyze the raw data with the initial database.
- Select events for optimization.
- Generate an input data file for the optimization.
- Optimize the desired quantity.
- Analyze the raw data with the optimized database.
- Use the diagnostic tools to test the target reconstruction.

The above procedure usually requires multiple iterations and has to be followed for each of the quantities requiring optimization. For E97-110, the focal plane offsets, $\phi_{\rm tg}$, $\theta_{\rm tg}$, $y_{\rm tg}$, and kinematically corrected momentum ($\delta p_{\rm kin}$) were optimized. ESPACE [97] was used to analyze the raw data, however the new ROOT/C++ Hall A Analyzer [98] can also be used. The event selection and diagnostic tests were performed with the use of PAW [99].

Septum Magnet Related Procedural Changes

A few details of the procedure were modified to address specific concerns of optimization with the septum magnet. Since there were only three carbon foils to constrain the $y_{\rm tg}$ acceptance, the matrix elements dependence on $\phi_{\rm fp}$ was kept below fourth order. This helped to ensure that the target variables were reliably reconstructed within the spectrometer acceptance. For this experiment, individual sieve holes were optimized instead of entire columns, which is what was done in the past. This increased the number of constraints from a possible seven columns to 49 holes for each foil. The angular optimization is typically performed for $\phi_{\rm tg}$ and $\theta_{\rm tg}$ together. However with the increase in the number of constraints, their simultaneous optimization was not possible, so the angles were optimized independently.

Early in the optimization procedure, the $x_{\rm tg}$ coordinate calculated within ESPACE was found to be defective. Though the initial matrix elements reconstructed the target coordinates reasonably well, $x_{\rm tg}$ is more sensitive to discrepancies in the reconstruction at small angles. Since the nominal $\theta_{\rm tg}$ angle is calculated from this coordinate in OPTIMIZE++, the $\theta_{\rm tg}$ reconstruction was deficient. In the left hand-side of Fig. 6.8, the $x_{\rm sieve}$ positions are clearly shifted above the horizontal lines. The nominal sieve slit positions are shown by the grid lines. To improve the out-of-plane angular reconstruction, OPTIMIZE++ was modified by adding an $x_{\rm tg}$ calculation [100], which is based on the survey information. This $x_{\rm tg}$ calculation is given by Eq. (6.14),

$$x_{\rm tg} = -\theta_{\rm tg}\frac{z_{\rm react}\cos\Theta_0}{\cos(\tan^{-1}\phi_{\rm tg})} - y_{\rm beam}, \tag{6.14}$$

where $\theta_{\rm tg}$ and $\phi_{\rm tg}$ are the nominal angles from a specific sieve slit hole for a given foil. The calculated values for $x_{\rm tg}$ are used by adding a flag when OPTIMIZE++ is run. This

modification helped resolve the deficient $\theta_{\rm tg}$ reconstruction. Fig. 6.8 shows the sieve slit reconstruction for the central foil using $x_{\rm tg}$ calculated from ESPACE and from Eq. (6.14) in OPTIMIZE++. Compared to Fig. 6.7, the sieve images are rotated clock-wise by 180°.

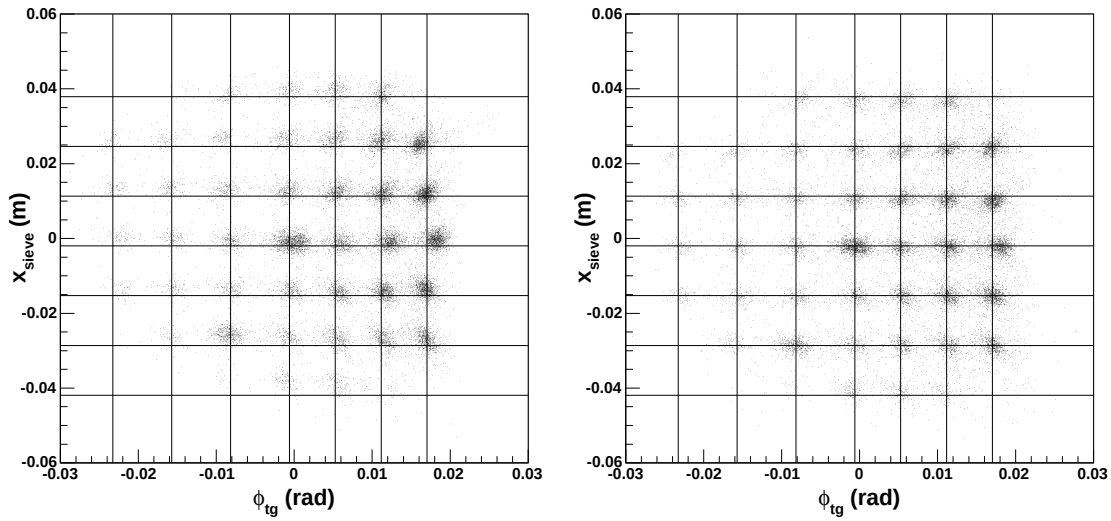

FIG. 6.8: Reconstructed sieve slit coordinates for the central ^{12}C foil using $x_{\rm tg}$ in the optimization calculated from ESPACE (left) and Eq. (6.14) (right). The grid lines represent the nominal sieve slit positions. When $x_{\rm tg}$ is used from ESPACE, the $x_{\rm sieve}$ positions are shifted above the nominal lines. The calculation for $x_{\rm tg}$ using Eq. (6.14) centers the data with respect to the nominal positions.

Typically a tight cut on the elastic peak is used to help eliminate punch-through events from the sieve slit. However, events from the upstream foils passed through a pair of NMR coils that were located upstream along $z_{\rm react}$. This caused the scattered electrons to lose enough energy so that their momentum was no longer in the elastic peak. The $x_{\rm fp}$ distributions for the upstream and central foils with a cut on the sieve slit central hole are shown in Fig. 6.9. In the first order approximation, $x_{\rm fp}$ is directly related to the momentum distribution at the target. In order to obtain reasonable reconstruction for the upstream foil and minimize punch-through events, a tight cut on the sieve holes was used

with a loose momentum cut. A list of momentum cuts to select events for OPTIMIZE++ is given in Table 6.7.

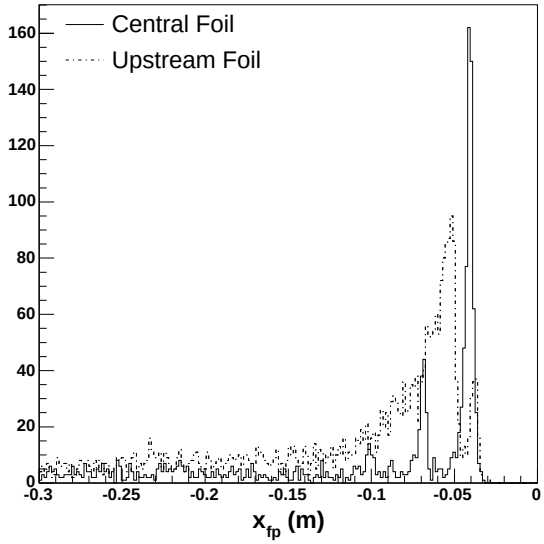

FIG. 6.9: The $x_{\rm fp}$ distribution is shown for the –20.0 cm upstream foil (dashed line) and for the central foil (solid line) with a cut on the sieve slit central hole. Both foils should have a sharp elastic peak at –0.04 m. However since the events from the upstream foil pass through a pair of NMR coils, the scattered electrons have lost energy so that their momentum appears between the elastic peak and the ^{12}C first excited state (–0.07 m).

6.4.5 Optimization for E97-110

For each set of optics data in Table 6.4, the focal plane offsets were optimized first, then the angles, $y_{\rm tg}$, and finally δ. After the the optimization was completed, the raw data were replayed with the new matrix elements, and the target reconstruction was tested with the aid of PAW. Typically after the first iteration of optimization the target reconstruction was good. Occasionally a second iteration was performed with improved cuts or by correcting errors in the identification of sieve slit holes. The target reconstruction for

Angle	Beam Energy (GeV)	Momentum Cut (GeV/c)
6°	1.096	1.050 – 1.100
	2.134	2.100 – 2.140
	2.844	2.825 – 2.860
9°	1.147	1.090 – 1.149
	2.235	2.216 – 2.240

TABLE 6.7: Momentum cuts used to select events for OPTIMIZE++ for the different beam energies and angles.

the 2.134 GeV data, after the optimization was completed, is shown in figure 6.10 for all three ^{12}C foils. The grid lines show the nominal sieve slit and foil positions from the survey reports. More details about the optimization for E97-110 are available in Ref. [101].

When the 1.096 and 2.844 GeV data were replayed with the new matrix elements, $y_{\rm tg}$ and $\phi_{\rm tg}$ were shifted with respect to their nominal positions. The septum magnet saturation effect is the cause of the shifts and is discussed in Appendix A. At these energies, the shifts were removed by optimizing the optics data.

For the 9° optics data, the same procedure was followed except the order of $x_{\rm fp}$ was kept below fourth order, since data were acquired with only three delta settings. Also the 3.319 GeV, 9° data were not optimized since elastic data could not be acquired at this energy. After optimization, the target reconstruction for the 9° data was comparable to the reconstruction at 6°. The optics matrix elements for all the energies at 6° and 9° can be found in [102].

The optimized momentum spectrum for 2.134 GeV is shown in Fig. 6.11. The design value of the spectrometer momentum resolution is 1 x 10^{-4} FWHM, and when multiple scattering from the scattering chamber windows and spectrometer entrance are included the resolution is 2.5 x 10^{-4} [67]. For E97-110, electrons from the upstream foil passing through the NMR coils results in significant loss of momentum resolution at low energies

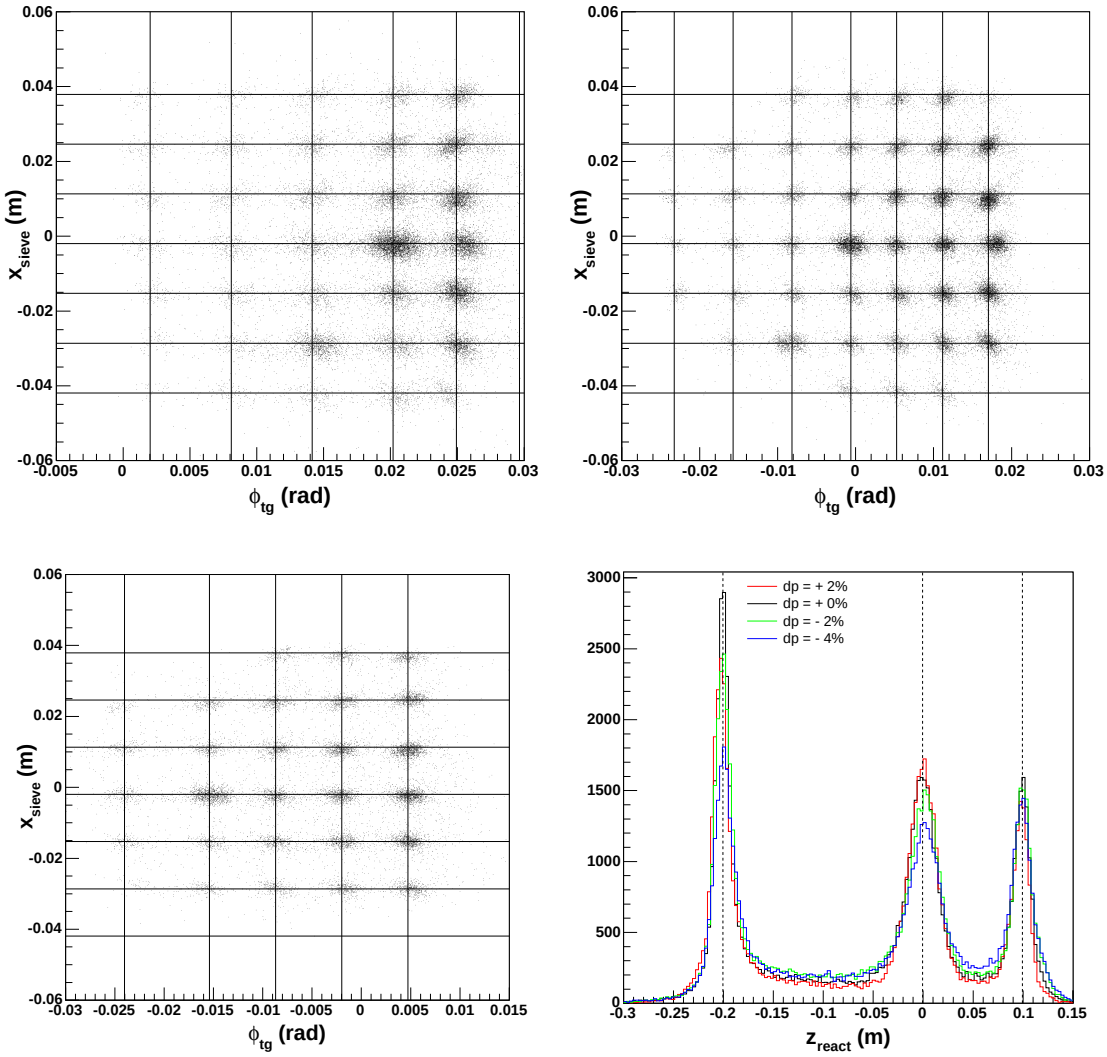

FIG. 6.10: Reconstructed sieve slit image for 2.134 GeV, 6° data. Upstream ^{12}C foil at $z_{\rm react}$ = –20.0 cm (top left), central foil at 0.0 cm (top right), downstream foil at 10.0 cm (bottom left), and $z_{\rm react}$ for all delta settings (bottom right). The lines represent the nominal sieve slit hole and foil positions.

and small angles. For example at 2.134 GeV, the upstream foil resolution was $\sim$ 60% larger compared to the central and downstream foils. In addition, the scattering chamber was filled with 1 atm of ^{4}He gas. The effect of scattering from ^{4}He on the momentum resolution was not studied since it has a negligible effect. In Table 6.8, the average momentum resolution of the right spectrometer at the optimized energies is shown.

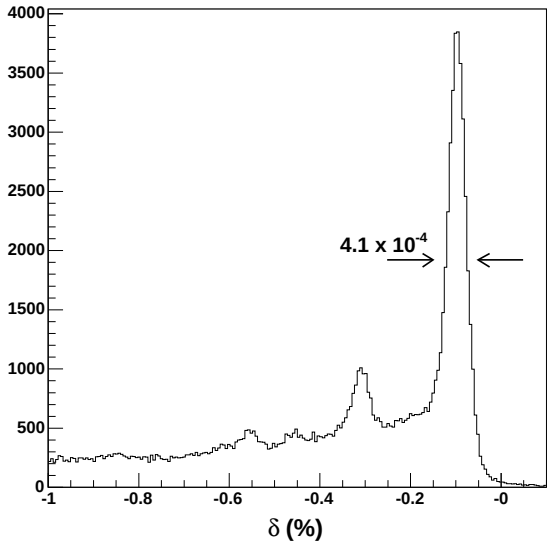

FIG. 6.11: The momentum of the scattered electron for all three carbon foils with a FWHM of 4.1 x 10^{-4} at δ = – 0.1%. The beam energy was 2.134 GeV, and the scattering angle was 6°.

Angle (deg.)	Energy (GeV)	δ Resolution $\langle$FWHM$\rangle$
6	1.096	8.8 x 10^{-4}
	2.134	4.4 x 10^{-4}
	2.844	4.2 x 10^{-4}
9	1.147	8.5 x 10^{-4}
	2.235	5.2 x 10^{-4}

TABLE 6.8: The momentum resolution of the right HRS with the septum magnet for E97-110. The values listed are the averages from the momentum scans for each energy.

Appendix A discusses the reconstruction issues that were seen after the optimization was completed. These issues include the $\phi_{\rm tg}$ shift for the central sieve-slit row, the 3.319 GeV, 9° data, and the septum magnet saturation effect.

6.5 Spectrometer Angle

From the sieve-slit surveys, the spectrometer central angle passing through the sieve-slit's central hole is determined by

$$\tan\Theta_0 = \frac{x}{z}\,, \tag{6.15}$$

where z is the position along the beamline, and x is the position transverse to the beamline in the horizontal plane. These positions are measured relative to the center of the target. Table 6.9 provides the central angles for the 6° and 9° data. There were two surveys for the 9°: one before (pre) and one after (post) the data taking. The uncertainty on the angles is due to a 0.5 mm uncertainty on the survey results.

Nominal Angle	Survey Angle
6° (pre)	$5.99^\circ \pm 0.04^\circ$
9° (pre)	$8.98^\circ \pm 0.04^\circ$
9° (post)	$9.01^\circ \pm 0.04^\circ$

TABLE 6.9: The spectrometer central angle from sieve-slit surveys.

6.6 Collimators

For E97-110, a set of collimators were used to block events coming from the target's glass windows. Traditionally software cuts on the reconstructed target variables have been used to remove these events. However due to the small scattering angles, the transverse position acceptance is about a factor of two smaller and the resolution is a factor of two worse (compared to 12.5°). The transverse position $y_{\rm tg} \approx z_{\rm react} \sin\Theta_0$, so a 40 cm long target is only 4 cm long in $y_{\rm tg}$. In addition, the cross section from scattering off the glass creates a sizable contamination to the physics of interest. Figure 6.12 shows a $z_{\rm react}$ nitrogen spectrum with and without the target collimators in place. Without the collimators, a significant contamination from the glass windows penetrates into the nitrogen events, which cannot be removed by acceptance cuts.

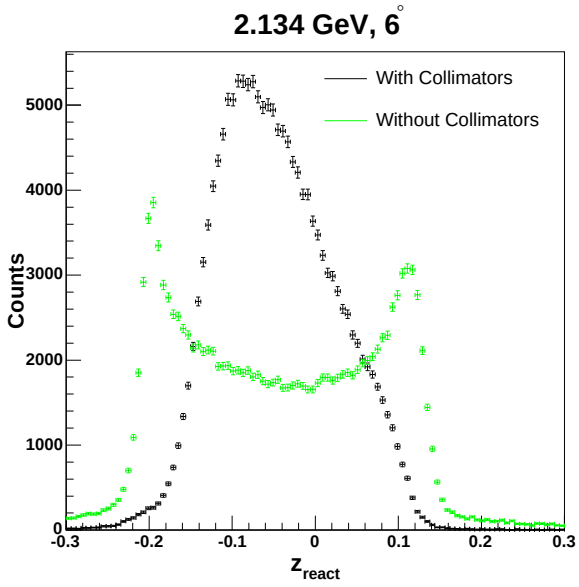

FIG. 6.12: Comparison of $z_{\rm react}$ with (black) and without (green) target collimators.

For the experiment, three sets of collimators were used:

- BRI6 - 6° data with the ice cone cell.
- BRS6 - 6° data with the standard cell.
- BRS9 - 9° data with the standard cell.

Each set of collimators consisted of an upstream (U) and downstream (D) collimator. The upstream collimator cuts events from the upstream window and the downstream from the downstream window. With the collimators in place the effective target length is approximately cut in half to 20 cm. Fig. 6.13 shows the layout of the three sets of collimators with respect to the center of the target. Table 6.10 provides the positions of the upstream and downstream collimators for the second run period. The positions are measured from the center of the target as defined in Section 6.5. Negative x values indicate the collimator was located to the right of the beamline. For the 9° data, a survey was performed before and after the data were taken. The two surveys agree with each other to 0.7 mm.

In addition to the target collimators, a collimator was placed around the sieve slit to shield the septum entrance from stray events. These stray events come from the beam on its way toward the beam dump. The collimator around the sieve slit was a 3 cm thick piece of tungsten. Table 6.11 gives the location z of the collimator's downstream face along the beamline and the height and width of the collimator aperture for 6° and 9°.

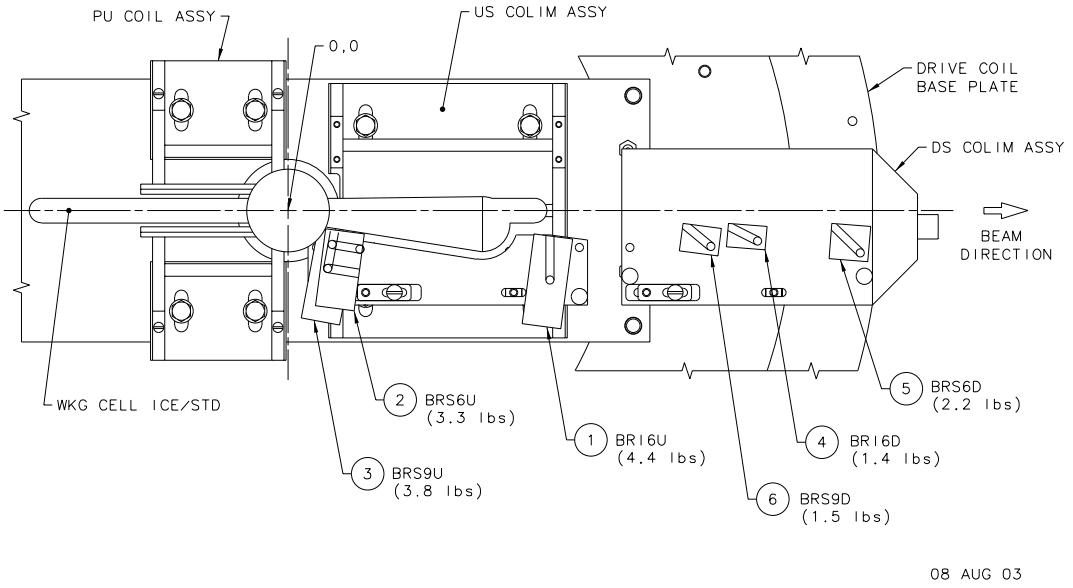

FIG. 6.13: Schematic of target collimator locations with respect to the target.

Description	z (mm)	x (mm)
Pre 6° survey		
BRS6U upstream beam left corner	29.2	-13.8
BRS6U downstream beam left corner	59.1	-18.0
BRS6D upstream beam right corner	417.4	-37.0
BRS6D downstream beam left corner	447.5	-39.4
Pre 9° survey		
BRS9U upstream beam left corner	22.3	-13.2
BRS9U downstream beam left corner	51.8	-18.9
BRS9D upstream beam right corner	301.0	-31.3
BRS9D downstream beam left corner	330.8	-35.3
Post 9° survey		
BRS9U upstream beam left corner	23.0	-12.6
BRS9U downstream beam left corner	52.5	-18.4
BRS9D upstream beam right corner	301.6	-31.3
BRS9D downstream beam left corner	331.5	-35.4

TABLE 6.10: The 6° and 9° target collimator positions from survey results.

Angle	z (mm)	$L_{\rm coll}$ (mm)	Height (mm)	Width (mm)
6°	828.5	833.1	99.4	55.1
9°	823.2	833.4	99.7	55.6

TABLE 6.11: Sieve-slit collimator location and aperture size. $L_{\rm coll}$ is the distance from the hall center to the center of the sieve-slit aperture's downstream face along the spectrometer's central ray.

CHAPTER 7

Analysis

For experiment E97-110, asymmetries and cross sections were measured for polarized electron scattering from polarized ^{3}He. In this chapter, the inelastic ^{3}He asymmetry and unpolarized cross-section analyses for the second run period are discussed. The selection of good events and data quality checks are reviewed. Sources of dilution and corrections to the physics data are also presented.

7.1 Asymmetries and Cross Sections

The longitudinal and transverse physics asymmetries are calculated by taking the ratio of the difference in polarized cross sections to their sum. The expressions are given by

$$A_{\parallel} = \frac{\frac{d^2\sigma^{\downarrow\Uparrow}}{dE'd\Omega} - \frac{d^2\sigma^{\uparrow\Uparrow}}{dE'd\Omega}}{\frac{d^2\sigma^{\downarrow\Uparrow}}{dE'd\Omega} + \frac{d^2\sigma^{\uparrow\Uparrow}}{dE'd\Omega}}, \tag{7.1}$$

and

$$A_{\perp} = \frac{\frac{d^2\sigma^{\downarrow\Rightarrow}}{dE'd\Omega} - \frac{d^2\sigma^{\uparrow\Rightarrow}}{dE'd\Omega}}{\frac{d^2\sigma^{\downarrow\Rightarrow}}{dE'd\Omega} + \frac{d^2\sigma^{\uparrow\Rightarrow}}{dE'd\Omega}}, \tag{7.2}$$

where $\uparrow$ and $\downarrow$ refer to the electron spin, pointing either parallel or anti-parallel to the beamline, and $\Uparrow$ designates that the target is polarized along the electron beam propagation. For the transverse case, $\Rightarrow$ indicates that the target is polarized perpendicular to the beamline.

The physics asymmetries are calculated from the raw experimental asymmetries given by the following equation:

$$A_{\parallel,\perp}^{\rm exp} = \pm \frac{A_{\parallel,\perp}^{\rm raw}}{f P_{\rm t} P_{\rm b}} \,, \tag{7.3}$$

where f is the dilution factor due to the small amount of nitrogen gas in the target cell and $P_{\rm t}$ and $P_{\rm b}$ are the target and beam polarizations respectively. The sign on the right hand side of Eq. (7.3) depends on the configuration of the insertable half-wave plate (IHWP) and the target spin direction. The raw asymmetries are calculated from the number of events within the chosen acceptance and detector cuts using the following expression:

$$A_{\rm raw} = \frac{\frac{N^+}{LT^+Q^+} - \frac{N^-}{LT^-Q^-}}{\frac{N^+}{LT^+Q^+} + \frac{N^-}{LT^-Q^-}} \,, \tag{7.4}$$

where $N^{\pm}$, $Q^{\pm}$ and $LT^{\pm}$ are the number of accepted events, the total charge and the correction for the computer deadtime with beam helicity $\pm$ 1. The '$+$' helicity state does not necessarily represent an electron with spin parallel to the direction of its propagation. The sign convention for the asymmetries is discussed in Section 8.1.1. The charge and deadtime corrections are calculated and applied for each run and will be discussed further in Sections 7.2.3 and 7.2.4.

Finally, the Born asymmetries are calculated by applying external and internal radiative corrections:

$$A_{\parallel,\perp}^{\rm Born} = A_{\parallel,\perp}^{\rm exp} + \Delta A_{\rm RC}^{\rm ext} + \Delta A_{\rm RC}^{\rm int} \,. \tag{7.5}$$

The unpolarized raw cross sections are determined by the following:

$$\sigma_0^{\rm raw} = \frac{d\sigma^{\rm raw}}{d\Omega dE'} = \frac{ps_1 N}{N_{\rm in}\rho LT\epsilon_{\rm det}} \frac{1}{\Delta\Omega\Delta E'\Delta Z}\,, \tag{7.6}$$

where:

- N is the number of scattered electrons detected within the chosen acceptance and detector cuts.
- ps_1 is the prescale factor for event type T_1.
- $N_{\rm in} = Q/e$ is the number of incident electrons determined by the charge measured with the BCMs.
- ρ is the target density.
- LT is the livetime correction for all helicity states.
- $\epsilon_{\rm det}$ is the product of all hardware and software detector efficiencies.
- $\Delta\Omega$, $\Delta E'$ and ΔZ are the solid angle acceptance, momentum acceptance for each spectrometer setting and the target length seen by the spectrometer.

The experimental cross section is determined by subtracting the nitrogen contribution:

$$\sigma_0^{\rm exp} = \sigma_0^{\rm raw} - \frac{\rho_{\rm N}}{\rho_{\rm He} + \rho_{\rm N}}\sigma_{\rm N}\,, \tag{7.7}$$

where $\rho_{\rm N}$ and $\rho_{\rm He}$ are the atomic densities of nitrogen and ^{3}He, respectively, inside the polarized cell, and the nitrogen cross section is $\sigma_{\rm N}$. The unpolarized Born cross sections are determined after external and internal radiative corrections have been applied:

$$\sigma^{\rm Born} = \sigma_0^{\rm exp} + \Delta\sigma_{\rm RC}^{\rm ext} + \Delta\sigma_{\rm RC}^{\rm int}\,. \tag{7.8}$$

Then the polarized cross section differences is calculated by taking the product of the experimental asymmetries and unpolarized cross sections:

$$\Delta\sigma^{\rm exp}_{\parallel,\perp} = 2 \cdot A^{\rm exp}_{\parallel,\perp} \cdot \sigma^{\rm exp}_{0} \,. \tag{7.9}$$

When the radiative corrections are applied, the cross section difference is expressed as

$$\Delta\sigma^{\rm Born}_{\parallel,\perp} = \Delta\sigma^{\rm exp}_{\parallel,\perp} + \delta(\Delta\sigma_{\parallel,\perp})^{\rm ext} + \delta(\Delta\sigma_{\parallel,\perp})^{\rm int} \,. \tag{7.10}$$

Before the radiative corrections are applied, the elastic radiative tail is subtracted, which has a sizable contribution for our kinematics at 6° and 9°.

For the analysis presented here, radiative corrections were only applied to the cross section differences. So the presented asymmetry and unpolarized cross sections are not radiatively corrected.

7.2 Data Analysis Quality Checks

7.2.1 Detectors

For the cross section analysis, the efficiencies of the various detectors are studied in detail. In these studies, the detector cuts are optimized to distinguish good electrons from background events. The background is mostly comprised of negatively charged pions and low-energy electrons. The detector cuts involve the VDCs, scintillators, Čerenkov and total shower calorimeter, and each cut has a software efficiency associated with it. Since these efficiencies are in most cases helicity independent, they can be safely ignored in the asymmetry analysis.

VDC: One-track Efficiency

The hardware efficiency of the drift chambers is approximately 100% [67], and hence, its inefficiency is neligible. A good electron should have only one track in the detector, but multi-track events can occur when several particles pass through the wire chambers simultaneously or if there are noisy wires. When this occurs, the analysis software can find more than one possible trajectory, and distinguishing between a good and bad event becomes difficult. In the cross section analysis, only events with one-track are kept, which results in an inefficiency that needs to be corrected. The one-track efficiency is defined as

$$\epsilon_1 = \frac{N_1}{\sum_i N_i}, \tag{7.11}$$

with i = 0, 1, 2, ... is the number of tracks[1]. The efficiency is determined by using the same cuts that are used in the cross section analysis. For the analysis, only the events from the main trigger are kept. In addition, PID cuts were chosen to reject greater than 99% of the background while keeping the electron efficiency higher than 99%. For E97-110, the total rate was typically between 4 kHz and 250 kHz, which resulted in a large number of events having multiple tracks for some kinematics. This especially occurred for the elastic and quasielastic kinematics as well as for the nitrogen data.

The 1-track efficiency is shown if Fig. 7.1. The elastic and quasielastic kinematics are pointed out, which have typical efficiencies greater than 90%. For the inelastic data, the efficiency is greater than 95% and 96% for the 6° and 9° data respectively. For this analysis, we have corrected the cross sections for 75% of events that are removed by the 1-track cut, since there is a good chance at least one of the tracks came from a good electron. The full amount of the correction is then used for the systematic uncertainty on

[1]The analysis software is capable of reconstructing several tracks.

this correction. Analysis is ongoing to determine how many of the multi-track events are good [103], which will reduce this systematic uncertainty.

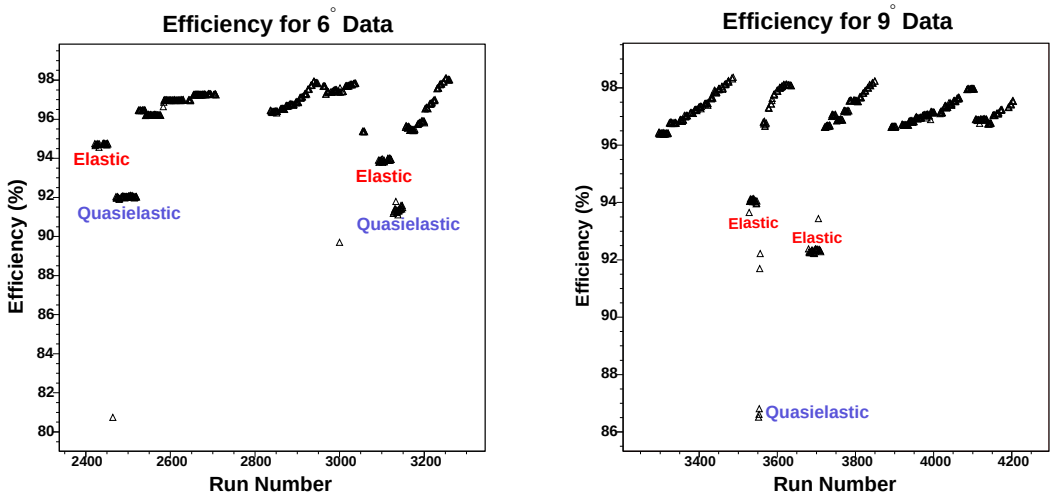

FIG. 7.1: The 1-track efficiency per run for the 6° (left) and 9° (right) data.

Scintillator Efficiency

As discussed in Section 6.3.2, the spectrometer detector package contains two scintillators planes that are used to form the data acquisition system's trigger. Two trigger types were used during the experiment that are considered good events: the main T_1 and the secondary triggers T_2. Only the main triggers are used in the analysis, whereas the secondary triggers are used to determine the hardware efficiency of the scintillators. The scintillator efficiency ϵ_{trig} is given by

$$\epsilon_{\text{trig}} = \frac{T_1}{T_1 + T_2}\,. \tag{7.12}$$

In most cases, the efficiency is greater than 99.4% as shown in Fig. 7.2 and excluding the T_2 events has a negligible impact.

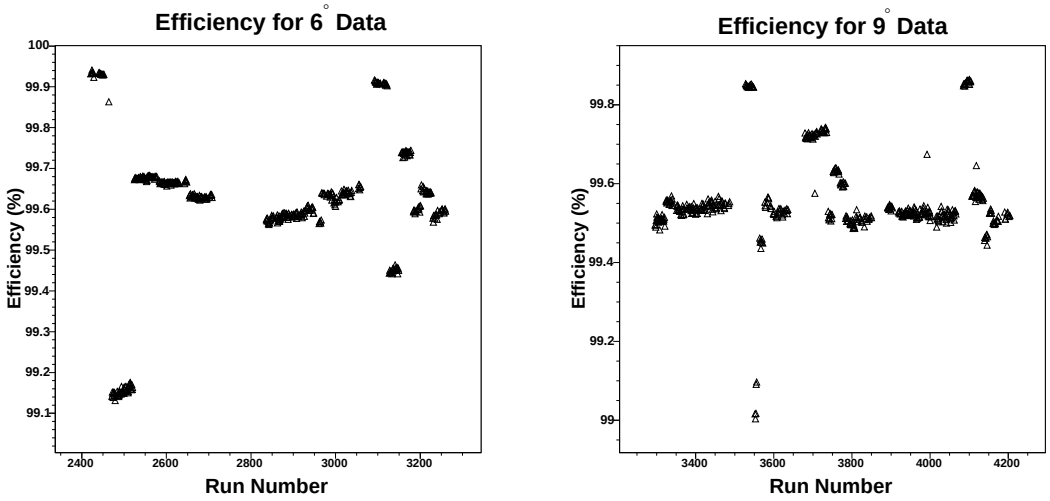

FIG. 7.2: The scintillator efficiency per run for the 6° (left) and 9° (right) data.

PID Efficiency

The Čerenkov and electromagnetic calorimeter detectors are typically referred to as particle identification detectors (PID). The majority of pions can be removed with a cut on the Čerenkov, since pions cannot directly trigger this detector. The detector calibration and efficiency determination are discussed in Refs. [63, 103]. From these analyses, ϵ_{det} $>$ 99.85% (99.67%) and the electron cut efficiency was better than 99.26% (99.66%) for the 6° (9°) data.

A two-dimensional cut on the shower and preshower from the calorimeter removes the low-energy knock-out electrons caused by pions. The calibration and efficiency study are detailed in Ref. [104]. For the total shower calorimeter, detection efficiency was greater than 99.76% and the cut efficiency was chosen to be larger than 99% for both the 6° and 9° data.

The PID cuts used for the asymmetry analysis are summarized in Ref [105]. Similar cuts were chosen for the cross section analysis based on the efficiency study for the

Čerenkov and electromagnetic calorimeter detectors.

7.2.2 Acceptance Cuts

The geometrical, or acceptance, cuts are placed on the target reconstructed variables: $\theta_{\rm tg}$, $\phi_{\rm tg}$, $y_{\rm tg}$ and δ, which are the event's out-of-plane angle, in-plane angle, transverse position and the relative momentum respectively. For the asymmetry analysis, loose geometrical cuts were used to remove any misreconstructed events on the edge of the acceptance. For E97-110, a set of collimators were used to block events coming from the windows; however, this required cuts at the collimator locations to remove events that passed through the collimators' edges.

In Appendix B, a summary of the acceptance cuts used in the asymmetry and cross section analysis is provided. For the cross section analysis, a detailed study of the spectrometer acceptance was carried out and is also described in the appendix. For the analysis presented in this document, only the positive half of the $\theta_{\rm tg}$ acceptance was kept due to background issues. A sharp peak is present at -26 mrads in $\theta_{\rm tg}$, which is easily removed by subtracting the empty reference cell yield from the ^{3}He yield. However a depression is left in place of the peak after the subtraction has been performed (see Section B.3.1). The difference between the unpolarized cross sections for the full $\theta_{\rm tg}$ acceptance and the positive half is 4–5% and 2–3% for the 6° and 9° data, respectively. For all kinematics, the cross section for $\theta_{\rm tg} > 0$ mrads is larger than the cross section for the full $\theta_{\rm tg}$ acceptance.

7.2.3 Charge Asymmetry

Significantly different amounts of charge can occur in each helicity state, which results in a charge asymmetry:

$$A_{\mathrm{Q}} = \frac{Q^{+} - Q^{-}}{Q^{+} + Q^{-}}. \tag{7.13}$$

where $Q^{\pm}$ is the accumulated charge for each helicity state, and the charge is given by the beam current monitors (BCM). Charge asymmetry is typically caused by sources in the accelerator injector, such as imperfections in the Pockels cell or half-wave plate.

When the cross section or asymmetry is calculated, the charge asymmetry is corrected by normalizing the charge for each helicity state independently as applied in Eq. (7.4). An independent data acquisition system (DAQ) and feedback system was used to to monitor the charge asymmetry and adjust the Pockels cell voltage to minimize the asymmetry (see Section 5.1.3). The feedback system updated every two minutes during experiment E97-110.

Before the physics asymmetries were calculated, the helicity-gated charges and the charge asymmetry were calculated for each run. The 6° and 9° charge asymmetries are shown in Figures 7.3 and 7.4 respectively. For each energy, the charge asymmetry in parts per million[2] (ppm) is plotted versus run number. The runs were also separated by their target orientation: black open circles for parallel kinematics and red squares for perpendicular. The average charge asymmetry for each energy was typically less than 200 ppm in both target orientations.

There are a few systematic effects seen in the plots. Usually the first run after the beam half-waveplate was either inserted or removed has a larger charge asymmetry than the runs following it from the same setting. For each half-waveplate change, the HAPPEx

[2]The unit parts per million denotes one particle of a given substance for every 999,999 other particles.

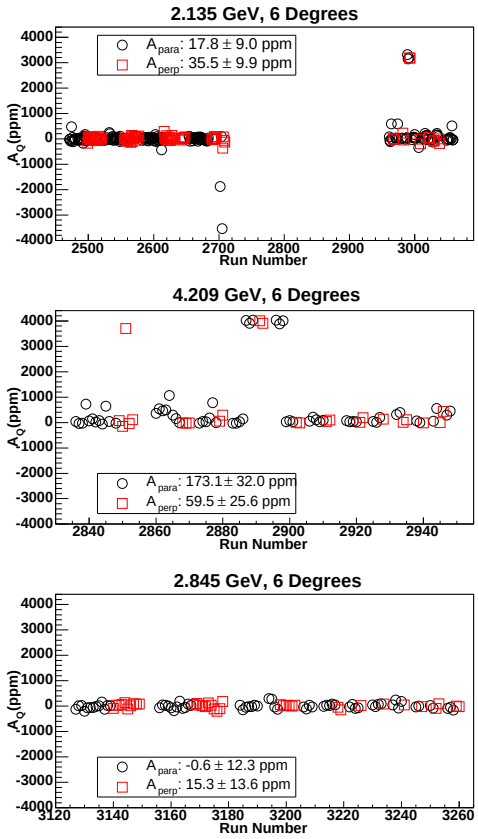

FIG. 7.3: Charge asymmetry (in ppm) for 6° data.

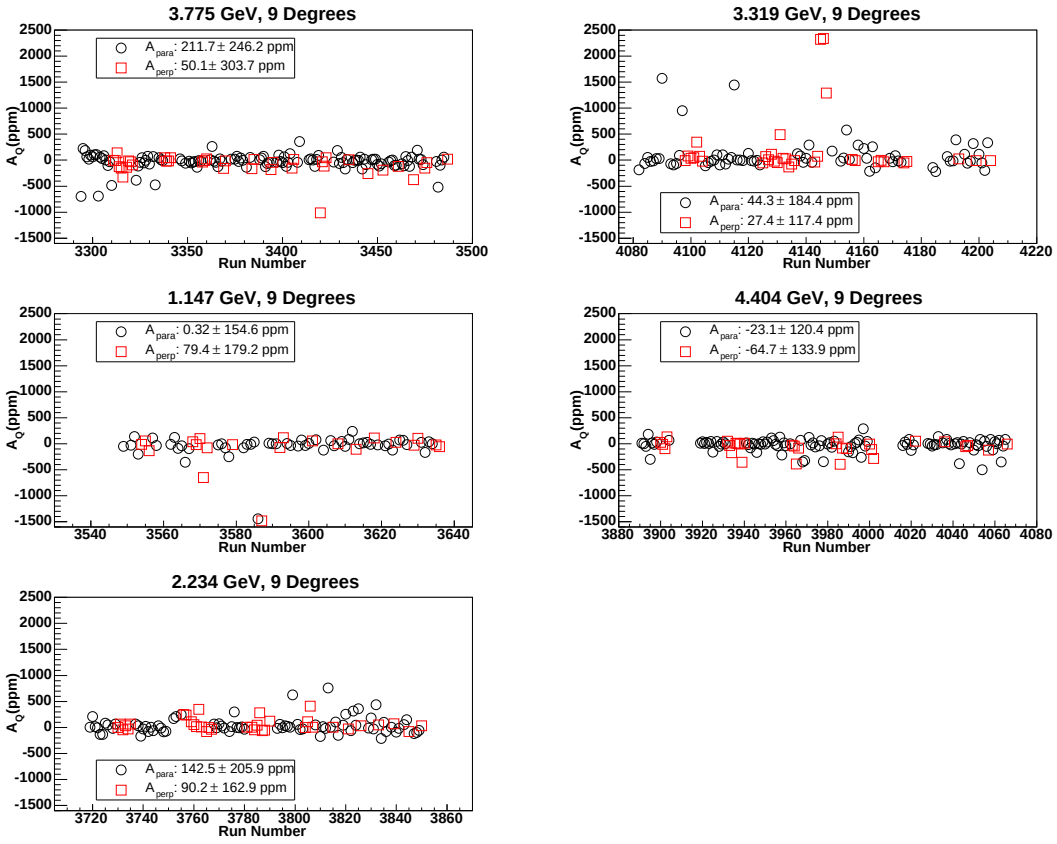

FIG. 7.4: Charge asymmetry for 9° data.

DAQ was restarted. Since the rates were high for the spectrometer DAQ, the duration of most production runs was less than 15 minutes, whereas the charge asymmetry feedback system updated every two minutes. The slow response from the feedback system compared to the relatively short production run time period is the suspected cause for the larger charge asymmetry after the half-waveplate change. The charge asymmetry usually converged below 200 ppm after the first run.

For the second run period, the charge asymmetry feedback system failed to converge three times: twice at 6° (2.135 GeV and 4.209 GeV), and once at 9° (3.319 GeV). The feedback was fixed, but about fifteen runs were affected with charge asymmetries between 3000 and 4000 ppm. Since the asymmetry was measured, it can easily be corrected. The corrected asymmetries were compared to asymmetries with small charge asymmetry corrections and found to have good agreement after the corrections. A lists of runs for the second run period where the charge asymmetry was greater than 900 ppm can be found in [105].

7.2.4 Livetime Correction

Livetime corrections need to be applied when extracting asymmetries and cross sections from the raw data. This quantity should be helicity independent, and if so, the livetime is divided out in Eq. (7.4). However there are circumstances where the livetime can become helicity dependent [106]:

- The physics asymmetry is large and the deadtime increases rapidly with the DAQ rate.
- Large charge asymmetry.
- The event size is different between the two helicity states.

- The deadtime fluctuates during the run, and the average effect does not cancel out.

The livetime correction was checked by calculating a livetime asymmetry for each run:

$$A_{\rm LT} = \frac{LT^+ - LT^-}{LT^+ + LT^-}. \tag{7.14}$$

As in the case of the charge asymmetry, the livetime asymmetries are typically less than 200 ppm. For nine runs, the asymmetry was over 1000 ppm. A few of these runs had either the DAQ rate too high, which resulted in high deadtime, or the time duration of the run was only a few minutes long. However there are four runs at 9° that have no apparent reason for a large livetime asymmetry. For these runs, the event size asymmetry between the two helicity states was checked and found to be smaller than the livetime asymmetry by at least an order of magnitude. The neighboring runs from the same kinematics have much smaller livetime asymmetries. A lists of runs for the second run period where the livetime asymmetry was greater than 900 ppm is available in Ref. [105]. The four runs mentioned above were included in the preliminary analysis.

7.2.5 Dilution

When the raw asymmetries and cross sections are formed, they need to be corrected for contamination from unpolarized material in the target cells. The two main sources of dilution arise from nitrogen inside the cell and the glass container. The polarized ^{3}He cells contain about 1% nitrogen[3] mixed with ^{3}He gas, which is used to quench unwanted photon emissions that can cause depolarization. The nitrogen, though a small amount, contributes significantly to the unpolarized cross section and causes a dilution to

[3]The ratio of the number density of nitrogen to the total number density of nitrogen plus ^{3}He gas is about 1%.

the asymmetry. The reason for this is that the nitrogen cross section is larger than the ^{3}He cross section at the same kinematic.

In the inelastic scattering region, events from the nitrogen contamination cannot be isolated from the ^{3}He events using detector or acceptance cuts. The nitrogen dilution is instead determined with data taken with a reference cell filled with nitrogen gas. For E97-110, nitrogen data were taken at almost every kinematic. The nitrogen dilution factors were determined for each kinematic at 6° and 9°. Details of the analysis can be found in [107]. The same acceptance cuts as discussed in Appendix B were used in the dilution analysis.

The N_2 dilution factor is defined as:

$$f_{N_2} = 1 - \left[\frac{Y_{N_2} - Y_{\rm empty}}{Y_{^3{\rm He}} - Y_{\rm empty}}\right] \frac{\rho_{\rm pol}}{\rho_{\rm ref}}, \tag{7.15}$$

where Y_{N_2}, $Y_{\rm empty}$ and $Y_{^3{\rm He}}$ are the yields from the nitrogen reference cell, empty reference cell and polarized ^{3}He runs respectively. The nitrogen densities in the polarized ^{3}He cell and reference cell are given by $\rho_{\rm pol}$ and $\rho_{\rm ref}$. Here the nitrogen density is the number of nitrogen atoms per unit volume. The yields for each target are calculated by:

$$Y = \frac{ps_1 N}{QLT\epsilon_{\rm det}}, \tag{7.16}$$

where N is the number of events after all cuts have been applied, ps_1 is the prescale factor for trigger $T1$, Q is the charge, LT is the $T1$ livetime, and $\epsilon_{\rm det}$ is the combined detector efficiency from all the detectors. Only the VDC one-track efficiency was corrected in the yield calculations. This is a reasonable approximation, since all the other detector efficiencies should be similar for different targets at the same momentum setting; hence they will factorize out of the dilution factor. However, the one-track efficiency is dependent on which target is in the electron beam.

Figure 7.5 shows the nitrogen dilution factors for the eight beam energies at 6° and 9°. The dilution factors were found to be between 0.87 and 0.94 with an uncertainty less than 0.3%.

Since collimators were used to remove the target windows from the acceptance, the dilution from the glass contamination should be small. However due to a two step process, the contamination from the glass actually increases significantly with decreasing spectrometer momenta. This effect was studied prior to the experimental run period [108] and involves the beam pipe entrance window to the scattering chamber. When the beam passes through the window a non-Gaussian halo occurs due to nuclear scattering. The halo then rescatters off the glass wall of the target cell.

Experiment E97-110 was particularly sensitive to this effect due to the small scattering angles. The glass contamination was partially reduced by decreasing the thickness of the beryllium entrance window to 5 mils (0.0127 cm). The remaining effect was measured by taking empty reference cell runs for most momentum settings. The dilution factor from the glass is defined as follows:

$$f_{\rm glass} = 1 - \frac{Y_{\rm empty}}{Y_{^3{\rm He}} - (Y_{\rm N_2} - Y_{\rm empty})\frac{\rho_{\rm pol}}{\rho_{\rm ref}}}, \tag{7.17}$$

where the yields and densities are defined the same as in Eq. (7.15). Figure 7.6 shows the contamination from the glass for the eight beam energies at 6° and 9°. The dilution factor dropped to 0.67 for the lowest momentum settings at 6°; whereas it dropped to 0.45 for the lowest momentum setting at 9°. If the 1.147 GeV, 9° data are excluded, which were taken for radiative corrections, then the glass dilution for the 9° data is better than 0.78. The glass dilution factor is included in Eq. (7.3) as an additional factor in the denominator.

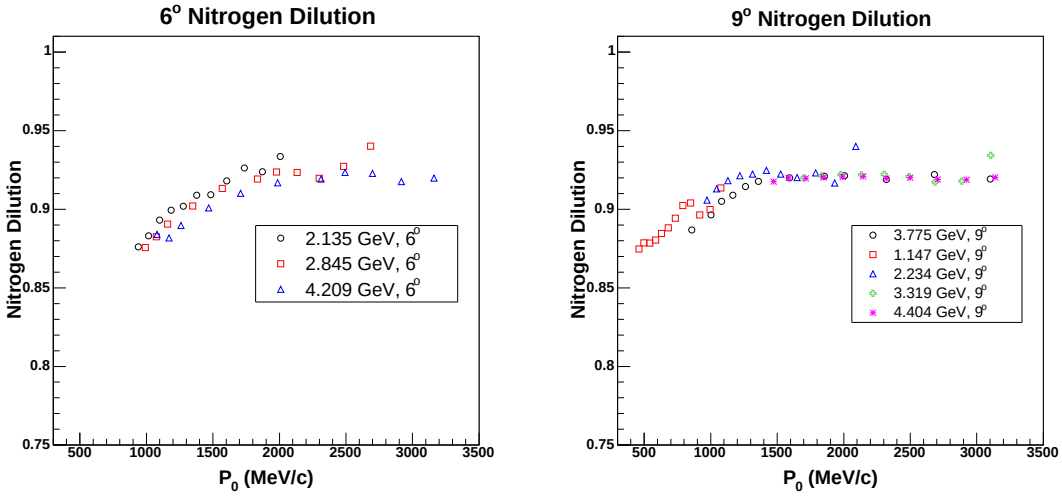

FIG. 7.5: Nitrogen dilution factors for the 6° (left) and 9° (right) data.

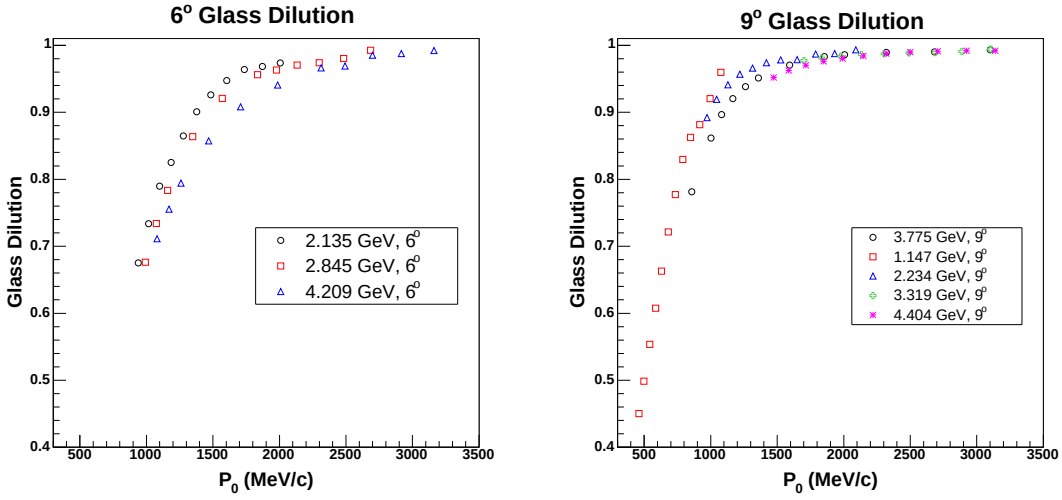

FIG. 7.6: Glass dilution factors for the 6° (left) and 9° (right) data.

7.2.6 False Asymmetry

Energy Label	Kinematic
1	2.135 GeV, 6°
2	2.845 GeV, 6°
3	4.209 GeV, 6°
4	1.147 GeV, 9°
5	2.234 GeV, 9°
6	3.319 GeV, 9°
7	3.775 GeV, 9°
8	4.404 GeV, 9°

TABLE 7.1: Kinematic correspondence to the energy labels in Figure 7.7.

The false asymmetry from the electron beam was checked by using unpolarized data from the empty and nitrogen reference cell runs. Additional data from the carbon foils target were not included in this analysis. For each momentum setting, good electrons were selected by applying the same PID and acceptance cuts that were used for the polarized ^{3}He data. Figure 7.7 shows the average false asymmetry for the eight beam energies at 6° and 9°. The energy label correspondence to the kinematic setting is give in Table 7.1. The average false asymmetry is small and consistent with zero. Since the correction is small, the total average value will be used as part of the systematic uncertainty on the results.

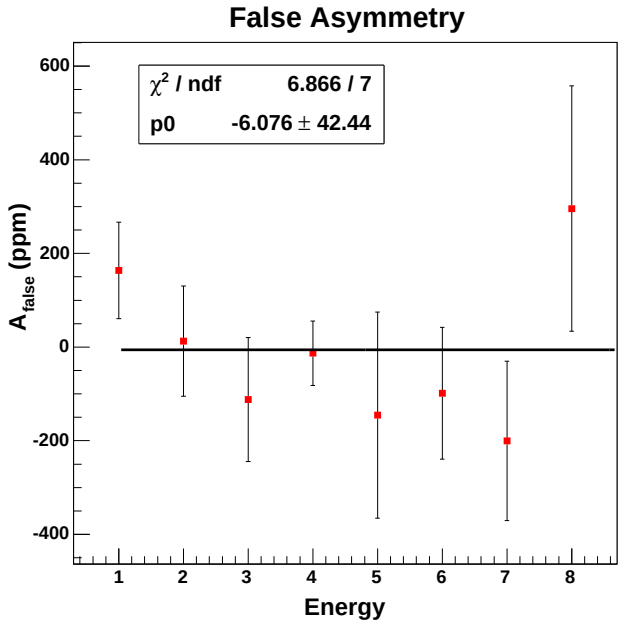

FIG. 7.7: False asymmetry from empty and nitrogen reference cell data.

CHAPTER 8

Results and Conclusions

In this chapter, preliminary results for the inelastic ^{3}He asymmetries, unpolarized cross sections and polarized cross-section differences are presented. After radiative corrections, the spin-dependent structure functions are extracted, and finally the generalized GDH integral is discussed.

8.1 Asymmetry Results

8.1.1 Asymmetry Sign Convention

As discussed in Section 7.1, the sign on the right hand side of Eq. (7.3) depends on the configuration of the IHWP and the target spin direction. The status of the IHWP is either 'IN' if it is inserted or 'OUT if retracted.' The relative sign of the beam polarization is determined from the Møller measurements. If during the Møller measurement the IHWP is 'IN', then the sign from Møller should be multiplied by -1. Then for each polarized ^{3}He run, the sign should be multiplied by $+1$ if the IHWP is 'OUT', and -1

if the IHWP is 'IN'. The absolute sign is determined by measuring a known longitudinal and transverse asymmetry. The longitudinal sign is measured using elastic electron scattering off of polarized ^{3}He, and the transverse sign is determined by using the $\Delta(1232)$ resonance, which has a large transverse asymmetry.

The target polarization sign depends on the direction that the target spin is pointing. Since ^{3}He has a negative magnetic moment, the ^{3}He spin points in the opposite direction to the target holding field. For the most part, the neutron spin points in the same direction as the ^{3}He nuclear spin. As mentioned previously, the target was either longitudinally or transversely polarized. This results in four possible target orientations: 0°, 90°, $180^\circ$and 270°. For experiment E97-110, the 90° configuration was not used, since the target half-wave plates could not be aligned for the longitudinal and transverse lasers at the same time. Based on the above information, we obtain the following sign conventions for the target polarization:

- 0°: longitudinal field points toward the Hall A beam dump, target spin = -1.
- 90°: transverse field points toward RHRS, target spin = -1.
- 180°: longitudinal field points toward the Møller polarimeter, target spin = $+1$.
- 270°: transverse field points toward LHRS, target spin = $+1$.

8.1.2 Inelastic ^{3}He Asymmetries

Following the analysis outlined in Section 7.2, the longitudinal and transverse asymmetries were formed for the 6° and 9° data. The beam and target polarizations were obtained from [74, 79]. The physics asymmetries without radiative corrections are shown

in Figures 8.1 and 8.2 versus the invariant mass W. The parallel configuration is represented with black open circles and perpendicular with red open squares. The quasielastic region is located around W = 938 MeV. As W approaches the $\Delta(1232)$ region, both asymmetries cross-over near the pion production threshold. In the Δ region, the perpendicular asymmetry is typically smaller than the parallel asymmetry. Beyond the Δ resonance, the transverse asymmetries are small and consistent with zero. The parallel asymmetries, however, appear larger with increasing invariant mass. For incident beam energies near 4 GeV at 9°, the asymmetry continues to grow with W. This behavior could be influenced by elastic radiative tails that have not been subtracted from the data. The parallel asymmetries at the Δ peak appear to have a moderate dependence on the momentum transfer Q^2 and increase with smaller Q^2. On the other hand, the transverse asymmetries become larger with increasing Q^2.

8.1.3 Target Cell Comparison

For the second run period, the first four momentum settings for the 2.135 GeV, 6° data were taken with the polarized ^{3}He cell Penelope. After a week of running, the cell ruptured and was replaced with the cell Priapus. The Penelope data were taken with a W up to 1400 MeV, then the remaining the data were taken with Priapus. As a check, data were acquired for two momentum settings that overlapped the data taken with Penelope at low W. Figure 8.3 shows the 2.135 GeV data where the two cells have overlapping data. The red triangles represent the data taken with Priapus, whereas the blue circles show the Penelope data. The Penelope and Priapus data sets agree well within the statistical uncertainties. In addition, the transition at 1400 MeV between the two cells is smooth. This agreement helps demonstrate that the various systematics are reasonably understood.

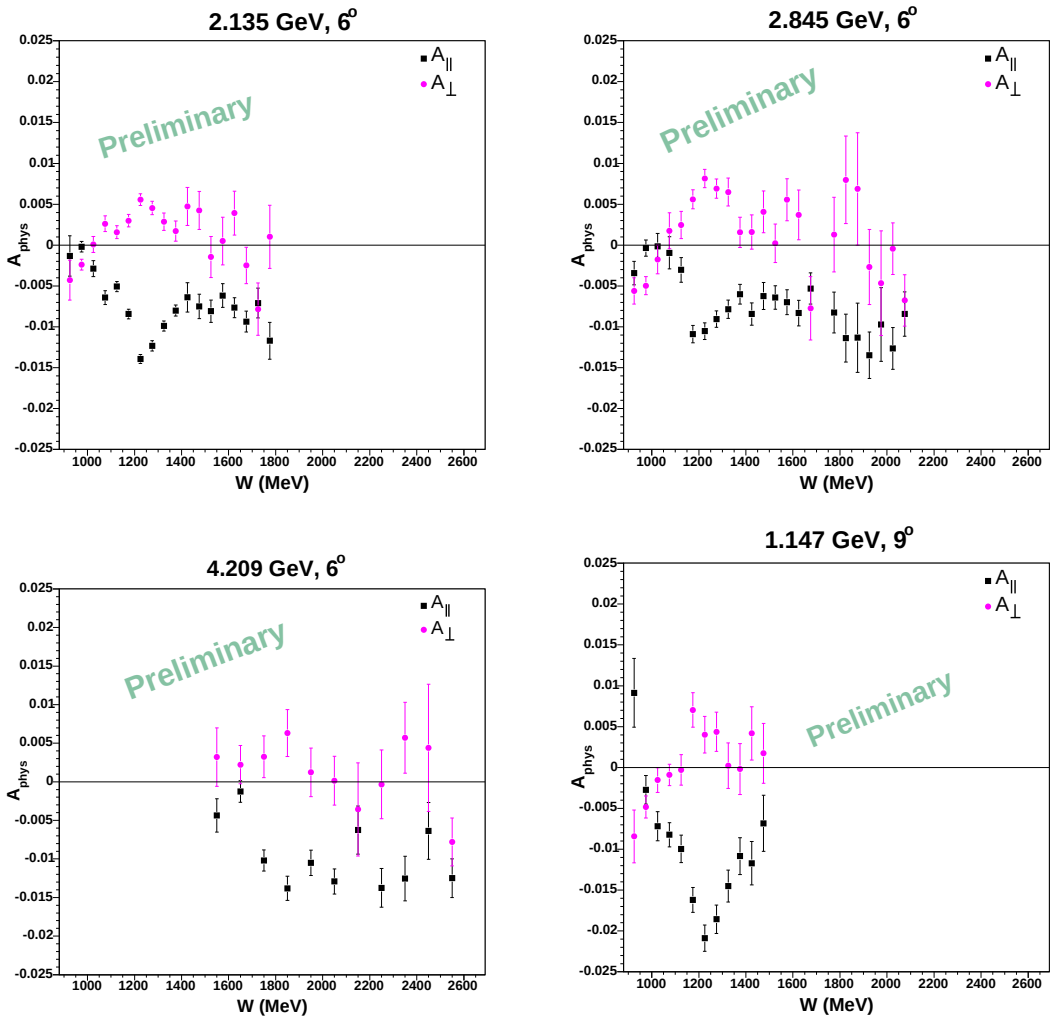

FIG. 8.1: E97-110 asymmetries for three incident energies at 6° and one at 9°.

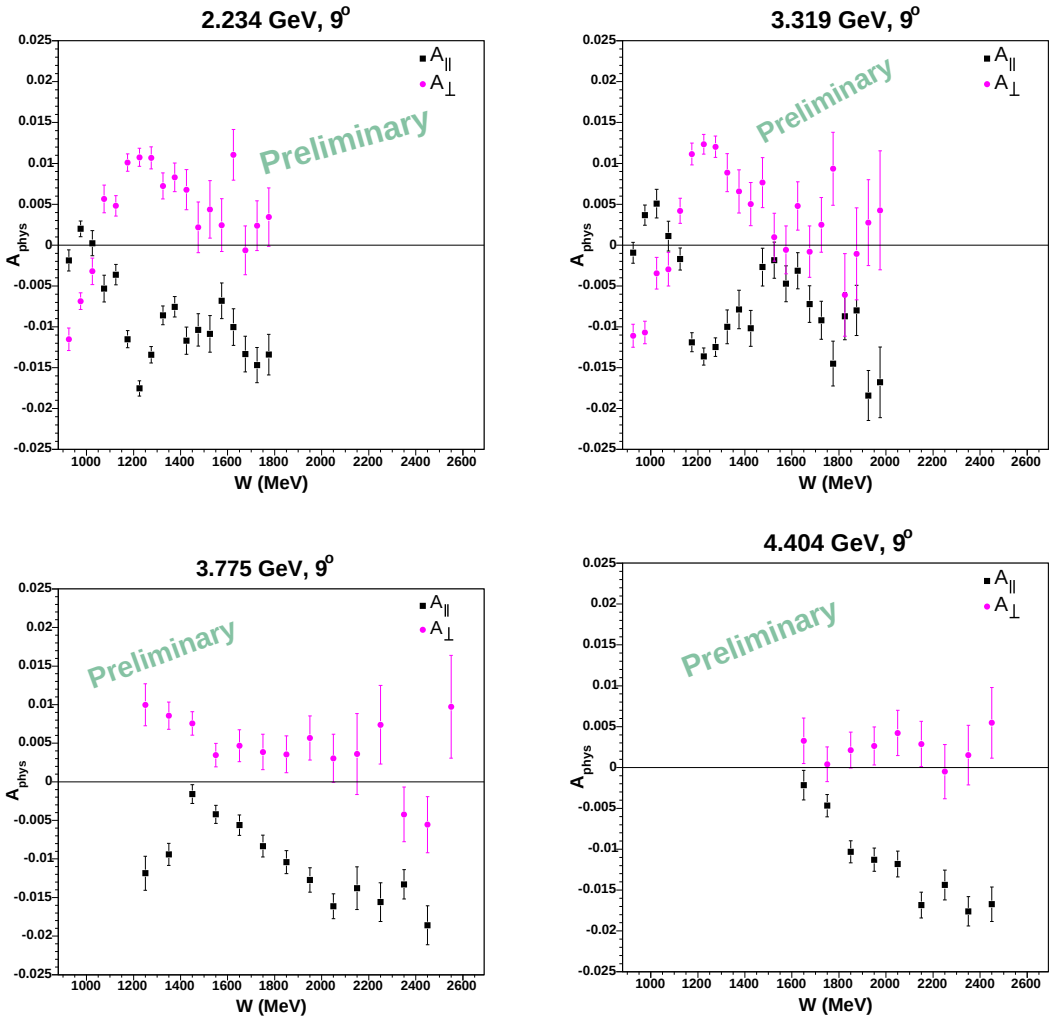

FIG. 8.2: E97-110 asymmetries for four incident energies at 9°.

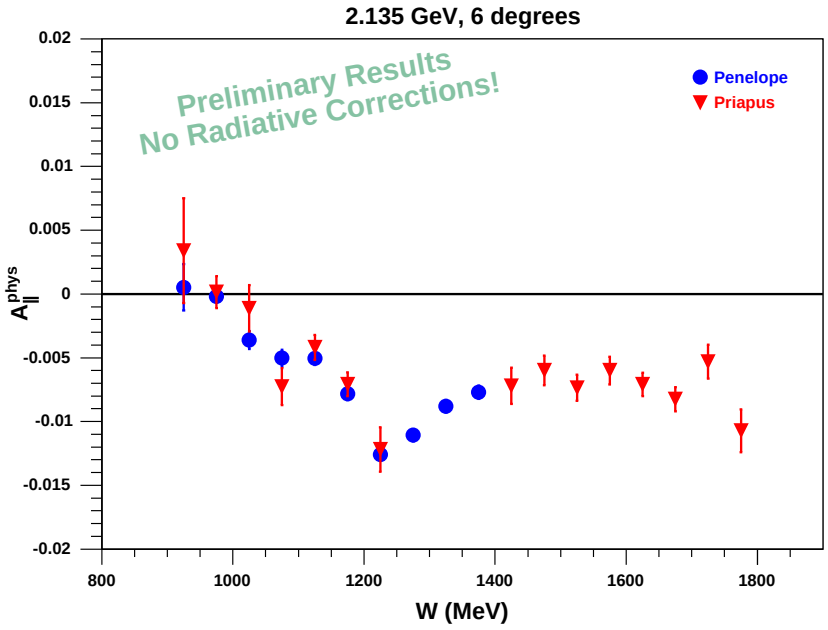

FIG. 8.3: Asymmetry comparison between target cells Penelope and Priapus.

8.1.4 PID Cut Study

A systematic study was performed to check the effect of the chosen PID cuts. This was accomplished by plotting the asymmetries with and without the PID cuts applied. For the low beam energies at 6°, not many pions are produced, so the PID cuts show little effect for these energies. For the 4.209 GeV data, the number of pions produced increased, and a larger effect can be seen in the asymmetries. At 9°, the longitudinal asymmetries for the 2.234 GeV data already show sizable differences at large W. For the transverse asymmetries a smaller difference is seen with the various PID cuts. This study indicates that for some kinematics the pions have a sizable asymmetry. More details on

the PID cut study are available in [105].

8.1.5 Pion Asymmetry

Unfortunately, even with good PID cuts, a small number of pions remain and contaminate the electron asymmetry. The pion contamination can be evaluated by using Eq. (7.3). In this analysis, the same cuts are used as applied on the electron asymmetries, except a cut on events is made that are not detected by the Cerenkov. The pion asymmetries are corrected for nitrogen dilution, glass dilution and beam and target polarizations.

The ratio of the number of pions to electrons is an important quantity that can be used to estimate the pion contamination. At low W or ν, the majority of the events are electrons; hence, this ratio is very small. As the invariant mass increases, the production of pions substantially increases and the ratio can become greater than one. In the large W region, the PID cuts typically reduce the pion to electron ratio by a factor of 10^4. Using this factor, the pion contamination to the electron asymmetry can be calculated by the following [73]:

$$\Delta A^{\mathrm{e}} = 10^{-4} A^{\pi}, \tag{8.1}$$

where A^{π} is the pion asymmetry and ΔA^{e} is the variation of the electron asymmetry due to pions. The pion asymmetry is suppressed for the maximum pion asymmetry of 20% to the level of 20 ppm. In the low W region, the suppression factor is larger than 10^4 due to the small number of pions; hence, the pion contamination is small for all kinematics.

8.1.6 Statistical and Systematic Uncertainty

The statistical uncertainty on the asymmetry is discussed in Appendix C for the case when the data is prescaled. The main sources of systematic uncertainty on the asymme-

tries are the beam and target polarization, contributing a relative error of $\sim$ 4% and 7.5% respectively. The measured false asymmetry is small and has a negligible contribution to the overall uncertainty. Due to the good pion rejection factor, the contribution from pion contamination is also small. The systematics on the charge and livetime corrections still need to be determined when these corrections are large.

The uncertainty on the dilution factors is small compared to the polarimetry, since they are measured directly from our data. The largest source of uncertainty in the nitrogen yields and cross sections is due to the 1-track efficiency. However the nitrogen cross section is suppressed in Eq. (7.7) by the density ratio ($\sim$ 2%). For most of our kinematics, the ^{3}He cross section uncertainty due to the 1-track efficiency correction for the nitrogen data is less than 1%

8.2 Unpolarized Cross sections

The unpolarized ^{3}He cross sections were generated following the steps in Section 7.1, and the acceptance cuts discussed in Appendix B were applied in the analysis. For previous experiments, the extracted cross sections represent an average over the solid angle defined by the acceptance cuts and spectrometer versus either the invariant mass or energy transfer. Then a finite acceptance correction is applied afterwards. Typically this correction is less than 2% in the resonance and DIS regions [10]. For experiment E97-110, this effect was expected to be larger because of the small angles. The acceptance and especially the cross section change dramatically over the solid angle.

The particle's scattering angle is calculated from Eq. (8.2),

$$\cos\theta_{\rm sc} = \frac{\cos\theta_0 + \phi_{\rm tg}\sin\theta_0}{\sqrt{1+\theta_{\rm tg}^2+\phi_{\rm tg}^2}}, \tag{8.2}$$

where θ_0 is the central angle of the spectrometer: 6° or 9°. For this analysis, the variation of the cross section with solid angle was handled by calculating the cross section for different bins in ϕ_{tg} for each bin in ν. The scattering angle changes by about 3° across the ϕ_{tg} acceptance. The second order dependence for $\theta_{\rm tg}$ results in a 0.5° variation in the scattering angle across the ϕ_{tg} acceptance. For this analysis, the variation in the acceptance with respect to $\theta_{\rm tg}$ was neglected but will be checked for the final analysis. The cross section variation with respect to $\phi_{\rm tg}$ is shown in Fig. 8.4 for the 2.135, 6° and 2.234 GeV, 9° data. Each of the ϕ_{tg} bins represents 6 mrad. Clearly the cross section has a strong dependence

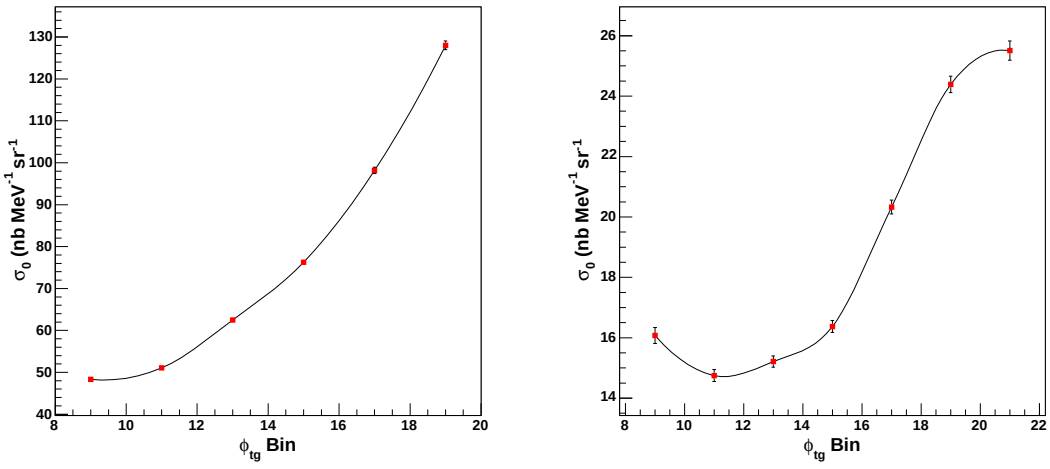

FIG. 8.4: E97-110 unpolarized cross section (ν = 1055 MeV) versus $\phi_{\rm tg}$ for the 2.135 GeV, 6° and 2.234 GeV, 9° data.

on the scattering angle at 6°, whereas, the dependence at 9° is less significant. After the generation of the cross sections, a bin-centering correction was applied to determine the central value of the cross-section within a given bin [109]. The following assumptions were used:

- The acceptance's angular dependence is described locally by a quadratic shape within

$\pm$ 1 bin.

- The cross section is also assumed to have quadratic dependence within $\pm$ 1 bin.

The bin centering was a less than 1% correction.

8.3 Experimental Cross Sections

The nitrogen cross sections were determined using the same procedure and then subtracted from the raw cross sections using Eq. (7.7). The nitrogen cross sections and ^{3}He experimental cross sections are shown in Fig. 8.5 for the 1.147 GeV and 2.234 GeV, 9° data. The nitrogen correction has a $5-12$% effect depending on the kinematics, which is in agreement with nitrogen dilution study discussed in Section 7.2.5.

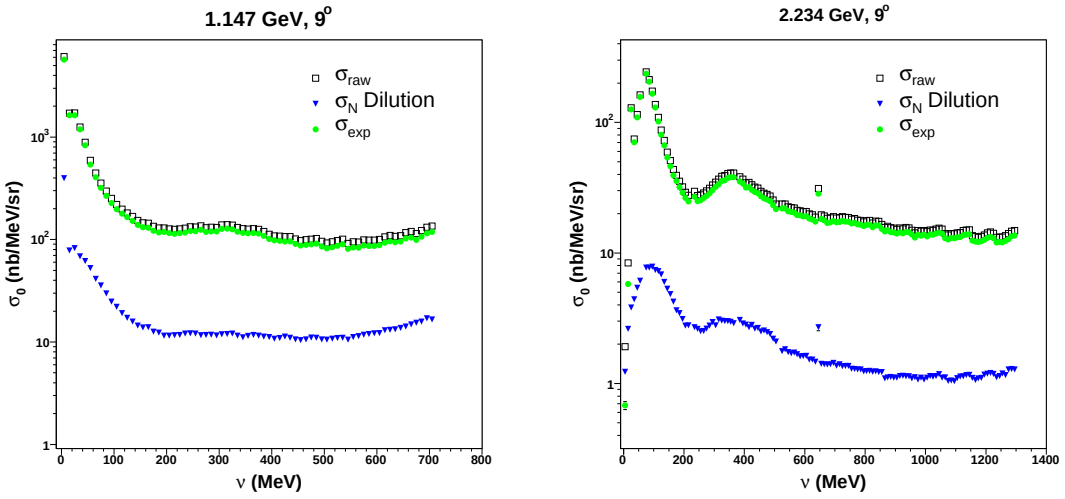

FIG. 8.5: E97-110 unpolarized ^{3}He cross section for the 1.147 GeV and 2.234 GeV, 9° data.

Before the cross-section differences are formed, the cross sections were interpolated to the same angle as the asymmetries for each beam energy. In most cases, the scatter-

ing angle of the asymmetry was between $\phi_{\rm tg}$ bins 13 and 15 from Fig. 8.4. The rare exceptions were for the elastic settings that have a strong dependence on the angle. For each ν bin, a linear interpolation was performed between the relevant $\phi_{\rm tg}$ bins to obtain the cross section that matched the asymmetry at the same angle. The uncertainty on the interpolation was determined by

$$\delta\sigma_{\rm int} = \sqrt{K^2\left(\delta\sigma_1^{\rm exp}\right)^2 + M^2\left(\delta\sigma_2^{\rm exp}\right)^2}\,, \tag{8.3}$$

where $\delta\sigma_1^{\rm exp}$ and $\delta\sigma_2^{\rm exp}$ are the cross-section uncertainties for two adjacent $\phi_{\rm tg}$ bins. The proportionality factors are then defined:

$$K = \frac{x - x_2}{x_1 - x_2} \tag{8.4}$$

and

$$M = \frac{x_1 - x}{x_1 - x_2} \tag{8.5}$$

where the angle being interpolated is x between angles x_1 and x_2 of the adjacent $\phi_{\rm tg}$ bins.

The angle interpolated cross sections are shown in Figs. 8.6 and 8.7 versus W for the eight incident beam energies without radiative corrections. The statistical uncertainties are shown on the points, and the systematic uncertainties are given by the grey band below each plot. For energies at 3 GeV and below, the strong quasielastic peak is seen at 938 MeV. The $\Delta(1232)$ is also seen. For the lowest two beam energies, the Δ is swamped by the quasielastic peak. Above the Δ region, the other resonances cannot be seen. For higher beam energies, the elastic radiative tail begins to grow at $W \geq 2.2$ GeV.

The unpolarized cross sections presented show discontinuities between momentum settings and other structures. These are particularly noticeable for the 4 GeV data sets. A study was conducted to investigate these $3-15\%$ effects, however, the study was unsuccessful in solving these problems. Except for the 3.775 GeV data set, the discontinuities

are $\leq 5\%$ but are systematically larger at higher incident energies. For the 3.775 GeV, 9° data, there is a 15% discrepancy between 1.4 GeV and 1.6 GeV when compared with the neighboring momentum settings. The large effects for this energy are possibly related to the septum saturation effect discussed in Section A.3 and need to be investigated further. The preliminary indication from this study is that these effects may not be acceptance-related and could be related to spectrometer optics, detector efficiencies, or backgrounds. Until these issues are resolved a $3-15\%$ systematic uncertainty will be applied on the cross section results, the actual value depends on the incident energy and momentum setting.

In Table 8.1, the estimate of the systematic uncertainty on the unpolarized cross sections is given. The uncertainty on the nitrogen dilution is primarily from the one-track efficiency; hence, the larger uncertainties correspond to low W and lower incident energies. The uncertainty from the acceptance is included in the uncertainty due to the discontinuities and other effects mentioned above. The density, charge and PID detec-

Source	Systematic Uncertainty		
Target density	2.0%		
Acceptance/Effects	5.0% (6°)	5.0% (9°)	15.0% (3.775 GeV, 9°)
VDC efficiency	3.0% (6°)	2.5% (9°)	
Charge	1.0%		
PID Detector and Cut effs.	$< 1.0\%$		
$\delta\sigma_{\rm raw}$	6.4% (6°)	6.2% (9°)	15.5% (3.775 GeV, 9°)
Nitrogen dilution	0.2–0.5%		
$\delta\sigma_{\rm exp}$	6.5% (6°)	6.3% (9°)	15.5% (3.775 GeV, 9°)

TABLE 8.1: Systematic uncertainties for the unpolarized cross sections. The 15% acceptance uncertainty for the 3.775 GeV, 9° only applies between 1.4 GeV and 1.6 GeV at this energy.

tor/cut efficiencies represent global systematic uncertainties for all kinematics. The VDC efficiency varies between 2% and 5% (4%) for the 6° (9°) data, whereas, the table shows

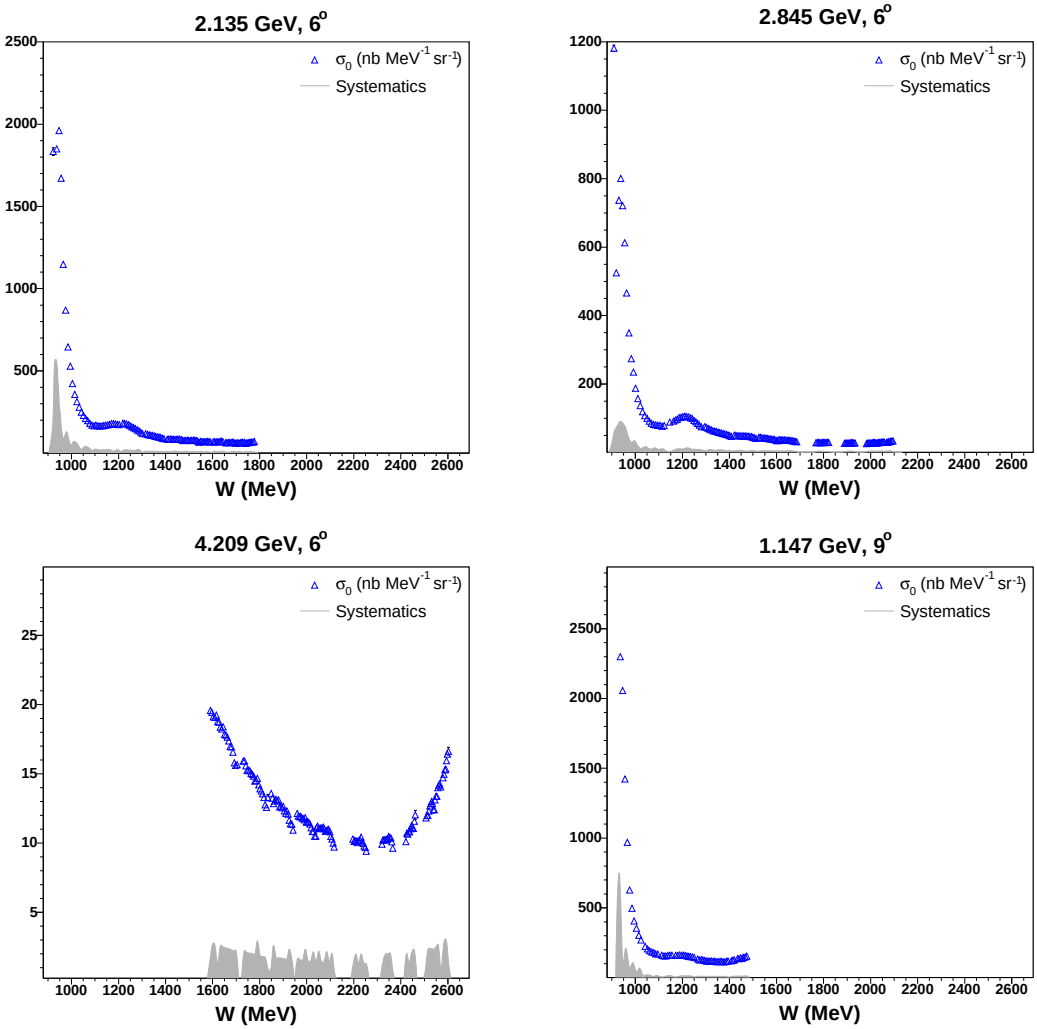

FIG. 8.6: Preliminary unpolarized cross sections for the three incident energies at 6° and 1.147 GeV at 9°.

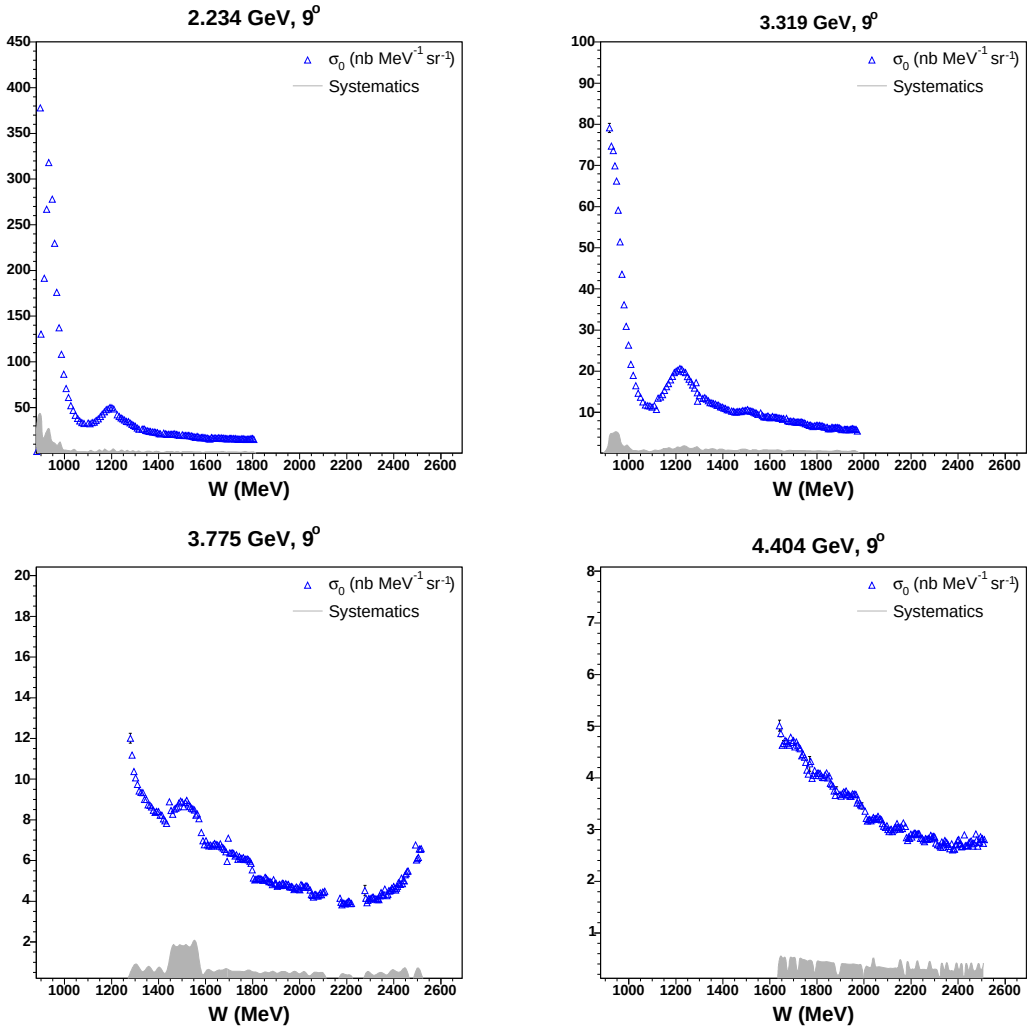

FIG. 8.7: Preliminary unpolarized cross sections for the incident energies at 9°.

representative values for the uncertainty due to the multi-track events. The systematic uncertainty shown in the figures have this variation included.

The uncertainties presented in Table 8.1 are preliminary and will be improved with further study. The expected uncertainty for the VDC one-track efficiency will be $\sim 1\%$, and the acceptance is expected to be known to 3% or better. With these improvements, the experimental cross section systematic uncertainty will be approximately $4-5\%$ for all incident energies.

8.4 Radiative Corrections

Before scattering from the target, the incident electron loses energy by passing through materials. The main processes by which this happens are bremsstrahlung and ionization (Landau straggling). Hence, the electron energy at the reaction vertex is less than that of the incident electron that entered the hall. After scattering, the electron also passes through material that results in energy loss before it is detected. This means that the electron energy at the vertex is higher than what is actually detected. The external radiative corrections are calculated to determine the measured cross sections at the true kinematics of the reaction. Internal radiative corrections are also taken into account for internal bremsstrahlung, vertex corrections and the vacuum polarization.

In Fig. 8.8 the scattered electron energy ($E_{\rm p}$) is plotted versus the incident energy ($E_{\rm s}$). The plot depicts where the eight incident energies lie in this plane. The 6° settings are shown with plus signs; whereas, the 9° are represented by the open circles. For each of the energies and associated momentum settings, a triangle is formed and bounded by a line representing elastic scattering. Lines are also shown for the pion threshold and the major resonances with the yellow band depicting the Δ region.

We can consider one of the incident energies such as 2.845 GeV, shown by the magenta plus symbols. The vertical band represents the spectrometer settings where events are detected. When the electron radiates photons, events fall into these regions from distant points on the plane. The value of the energy $E_{\rm s}$ ($E_{\rm p}$) is reduced before (after) scattering due to radiation and causes events to move horizontally (vertically) into the detected region. Therefore radiative corrections need to be considered from the entire triangle area. However, the points nearby the detected region contribute the most to the radiative corrections.

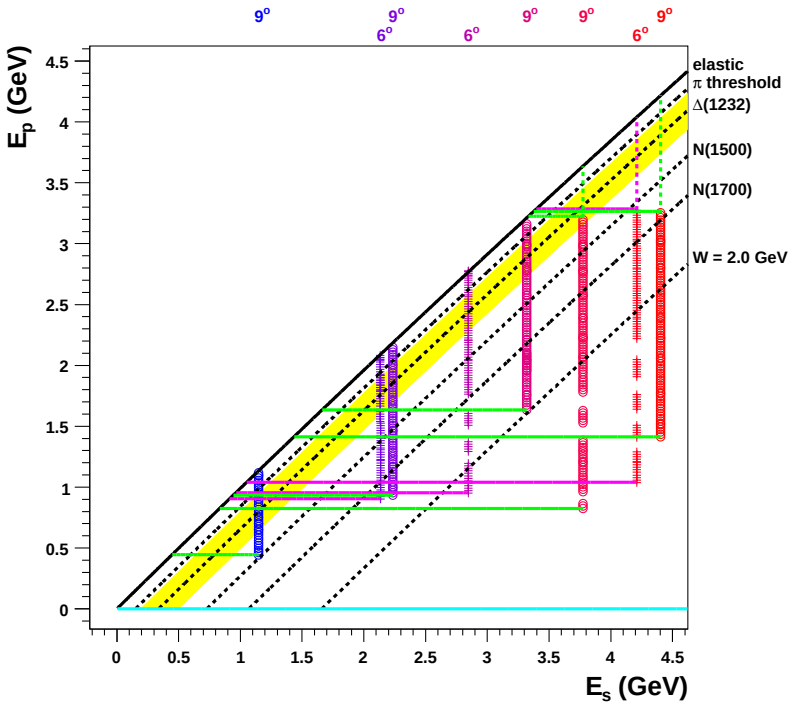

FIG. 8.8: Kinematic region that contributes to the radiative corrections. Provided by [79].

For the unpolarized cross section, the external and internal radiative corrections are determined by using Mo and Tsai's formalism [110] with the program RADCOR.F [111]. For the external part of the polarized cross-section differences, Mo and Tsai's formalism

is also used, since the surrounding materials are unpolarized. The formalism of Akushevich [112] is used for the internal corrections in the program POLRAD [113]. In the RADCOR.F code, the 'Energy Peaking Approximation' is used, since the primary contributions come from the vertical and horizontal contours along constant $E_{\rm s}$ and $E_{\rm p}$. This approximation allows us to reduce the two dimensional integration over all incident beam energies and over all final electron energies (consistent with a given $E_{\rm s}$ and $E_{\rm p}$) to two one dimensional line integrals. In the case of the internal corrections, the full integration is performed within POLRAD.

The objective of the radiative corrections is to determine the Born cross section $\sigma_{\rm Born}$ in the first-order diagram of Fig. 2.1. When this cross section is radiated, the experimental cross section $\sigma_{\rm exp}$ is produced. The process to extract $\sigma_{\rm Born}$ is iterative. Since the Born cross section is unknown, either cross section models or data are used as an initial guess. An integral over the energy spectrum is performed and a radiated cross section is produced. The difference between the radiated and initial experimental cross section is applied to the input cross section. Then another iteration is performed. Typically after a handful of cycles the procedure converges to the Born cross section.

Before the radiative corrections are applied, the elastic radiative tail must be subtracted from the experimental cross section. This tail is created when the electron emits a photon before elastically scattering from the target nucleus. The scattering process occurs at lower initial energy, which corresponds to a larger cross section. The radiative tail can result in a large rising tail at large ν. These tails can be seen in the 4.209 GeV and 3.775 GeV data in Figs. 8.6 and 8.7.

The final error on the cross sections is determined by combining the error on the

radiative corrections with the uncertainty from the experimental cross sections $\delta\sigma_{\rm exp}$:

$$(\delta\sigma_{\rm Born}) = (\delta\sigma_{\rm exp})^2 + (\delta\sigma_{\rm RC})^2 \ , \tag{8.6}$$

where $\delta\sigma_{\rm RC}$ is the cross-section uncertainty from the error on the radiative corrections. The systematic uncertainty due to the radiative tail subtraction also needs to be included in the final cross-section uncertainty.

A summary of the radiation lengths before and after scattering is available in Ref [114]. A first pass extraction of the radiative corrections has been performed [79], though the systematic uncertainty from the corrections has not been determined. We expect the systematic uncertainty on the radiative corrections to be within $10-20\%$ from past experience. Except for the 2.135 GeV, 6° and 1.147 GeV, 9° data, our own data was used as the initial guess for the radiative corretions. For the 2.135 GeV data, a model was built by scaling the the 1.147 GeV cross sections to 6°. However a model was not created to perform the radiative corrections for the 1.147 GeV data. Eventhough radiative corrections were extracted for this data, the Born cross-section differences should be viewed as suspect at best. A thorough systematic study of the radiative corrections is ongoing.

8.5 Polarized Cross-section Differences

The polarized cross-section differences are generated from the experimental cross sections and parallel and transverse asymmetries by using Eq. (7.9). The systematic uncertainties come from the uncertainties on the experimental cross sections, beam polarization (3.5%) and target polarization (7.5%). The beam polarization uncertainty also includes an estimate from the bleedthrough uncertainty. The cross-section differences are shown in Figs. 8.9 and 8.10 with radiative corrections applied. The inner (outer) error

bars represent the statistical (total) uncertainties. However, the total uncertainties do not include the uncertainty from the radiative corrections. The parallel configuration is represented by the open red squares, while the perpendicular is shown by the solid black circles. The size of the radiative corrections are shown for the parallel and transverse data by the dashed red and black curves respectively. For the lowest energies, the large contribution from the quasielastic region is seen. Below an incident energy of 3.3 GeV, the Δ resonance can again be seen around 1232 MeV. Beyond the Δ, the transverse cross-section difference is small and close to zero; whereas, the parallel cross-section difference is small but clearly non-zero.

The uncertainty on the target polarization is still preliminary. The final uncertainty is expected to be $\sim$ 4%, which will improve the systematic uncertainty on the cross-section differences to the 7% level versus the preliminary value of $10-17$%.

8.6 ^{3}He Spin Structure Functions g_1 and g_2

The spin structure functions are formed from the polarized cross sections differences from the following expressions:

$$g_1 = \frac{MQ^2}{4\alpha^2}\frac{y}{(1-y)(2-y)}\left[\Delta\sigma_{\parallel} + \tan\frac{\theta}{2}\Delta\sigma_{\perp}\right] \tag{8.7}$$

$$g_2 = \frac{MQ^2}{4\alpha^2}\frac{y^2}{2(1-y)(2-y)}\left[-\Delta\sigma_{\parallel} + \frac{1+(1-y)\cos\theta}{(1-y)\sin\theta}\Delta\sigma_{\perp}\right], \tag{8.8}$$

where $y = \frac{\nu}{E}$.

The ^{3}He spin structure functions are plotted versus x, as measured at constant energy, in Figs. 8.11 and 8.12. The error bars depict the total uncertainties. For the Bjorken variable, the ^{3}He mass was used; hence, x = 1 corresponds to ^{3}He elastic scattering. Proceeding right to left along the horizontal axis, we encounter the quasielastic peak. The

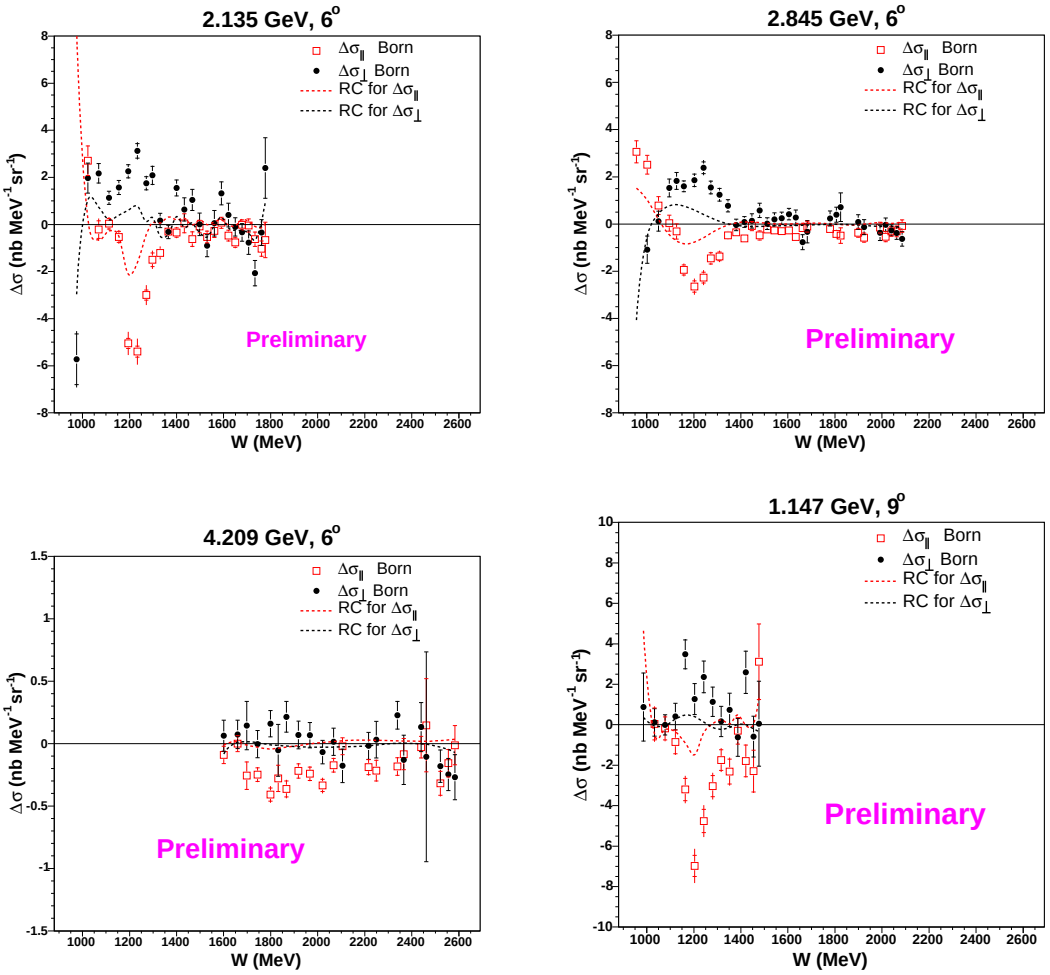

FIG. 8.9: Preliminary polarized cross-section differences for the three incident energies at 6° and 1.147 GeV at 9°. The inner (outer) error bars represent the statistical (total) uncertainty.

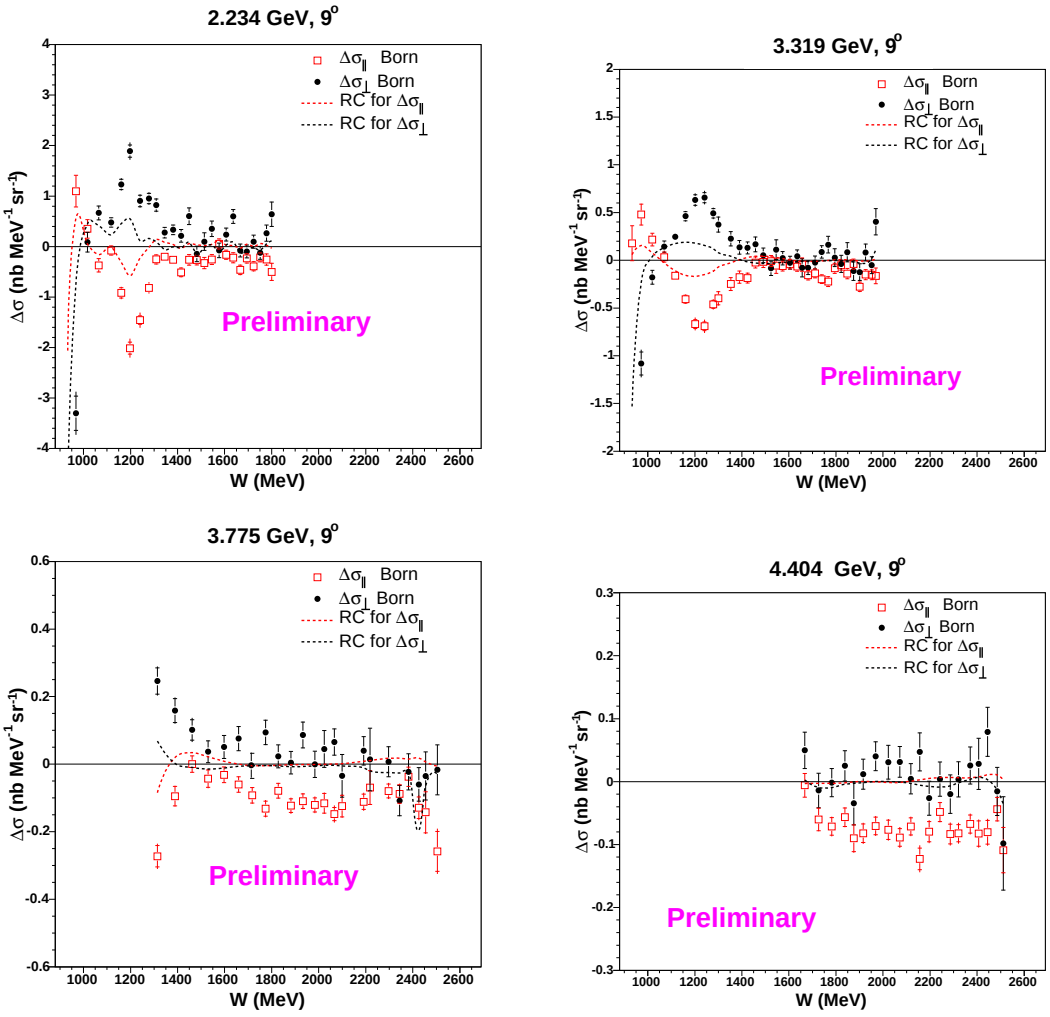

FIG. 8.10: Preliminary polarized cross-section differences for the incident energies at 9°. The inner (outer) error bars represent the statistical (total) uncertainty.

entire peak is not included in the plots, but from the included data, the quasielastic contribution is significant at these kinematics. Following the quasielastic, there is a crossover for both structure functions at the pion production threshold. At lower x, we find the $\Delta(1232)$ resonance and find that $g_1 \approx -g_2$. The Δ is primarily an M_{1+} transition, and further, the unpolarized cross section in this region is well described with only a transverse contribution. This implies that the longitudinal-transverse cross section σ_{LT} should be suppressed in the Δ region. If we refer back to Eq. (3.11), $\sigma_{LT} \propto (g_1 + g_2)$, and hence, a zero σ_{LT} would indicate an equal and opposite g_1 and g_2. For experiment E97-110, this is approximately seen in the data. This behavior was also seen in the E94-010 data between 0.1 GeV^2 and 0.9 GeV^2.

Beyond the Δ region, g_1 is non-zero and approximately flat, whereas, g_2 is consistent with zero but with large uncertainty. From Eqs. (8.7) and (8.8), we see that g_1 is dominated by the parallel kinematics, and g_2 is primarily from the transverse data. The contribution from $\Delta\sigma_\perp$ to g_1 is about 5% (8%) at 6° (9°), whereas, the parallel contribution to g_2 is about $2-5$% ($3-8$%) at 6° (9°).

8.7 Transverse-Transverse Cross Section σ_{TT}

The spin structure functions can also be expressed in terms of the virtual photoabsorption cross sections of Eqs. (3.11) and (3.12). Preliminary ^{3}He results for the generalized GDH integrand σ_{TT}/ν is shown in Figs. 8.13 and 8.14 as measured for the eight incident beam energies. The inner (outer) error bars represent the statistical (total) uncertainties. The $\Delta(1232)$ resonance has a significant negative contribution, which increases at lower Q^2. However, there is also some hint that the quasielastic contribution, which has the opposite sign, is sizable. This behavior can be seen for the 2.845 GeV and 3.319

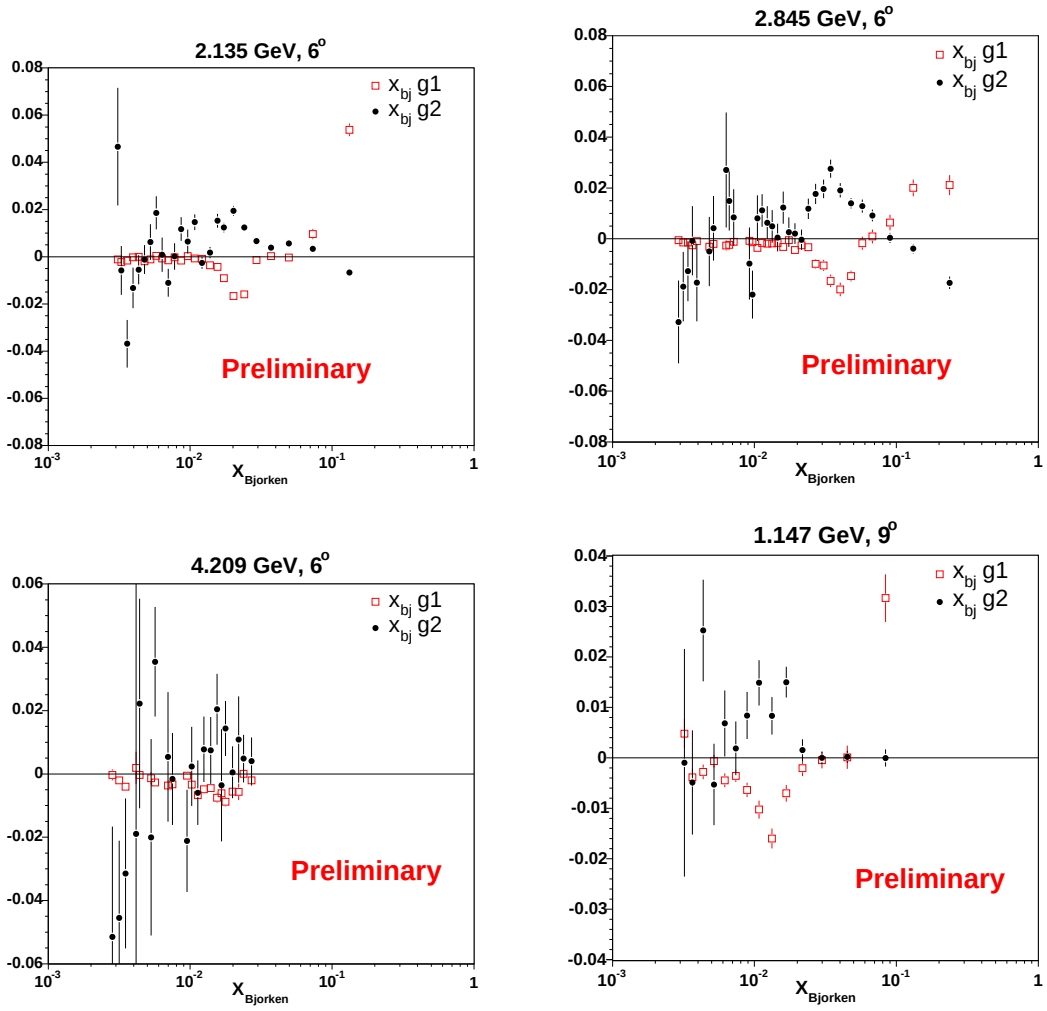

FIG. 8.11: Preliminary ^{3}He structure functions at constant energy for the 6° and 1.147 GeV, 9° data. The error bars represent the total uncertainty.

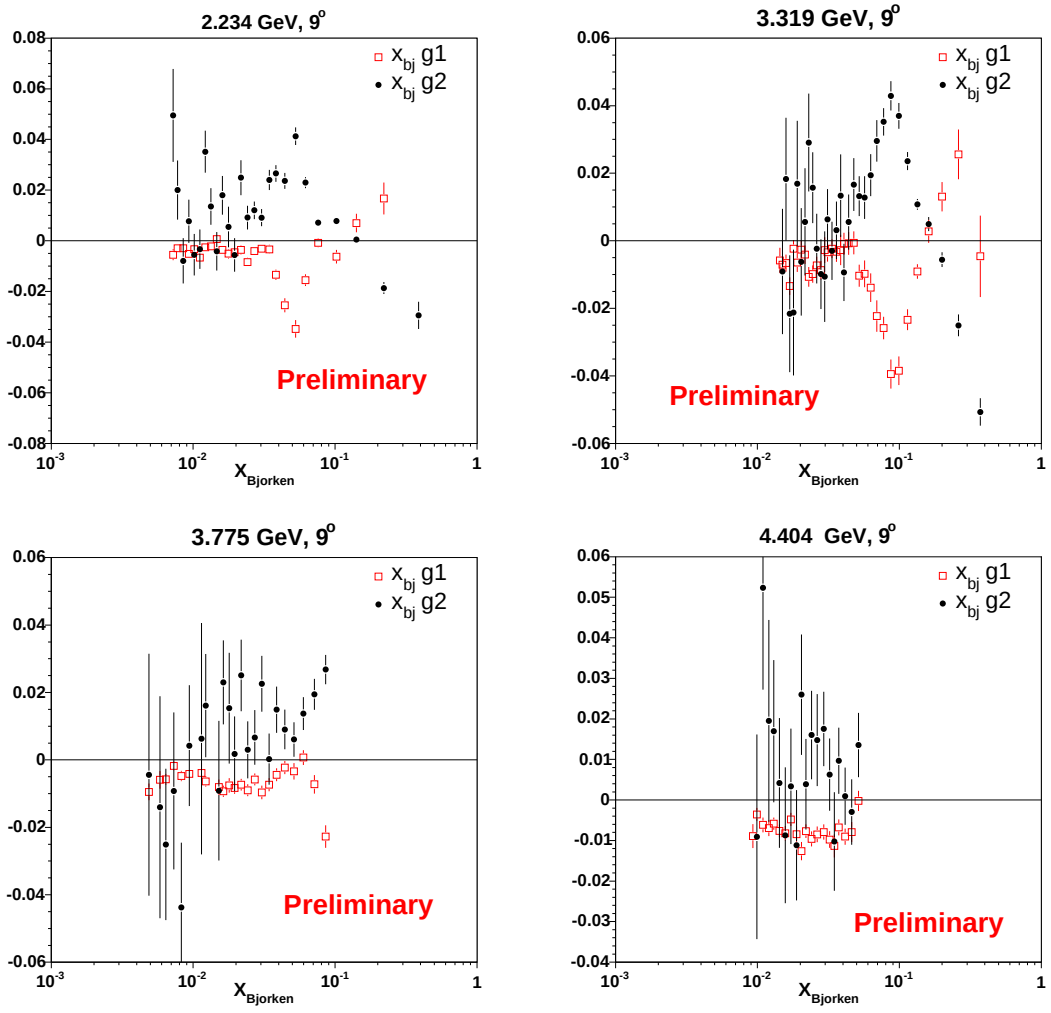

FIG. 8.12: Preliminary ^{3}He structure functions at constant energy for the 9° data. The error bars represent the total uncertainty.

GeV data. Beyond the Δ region, the integrand is small and approximately flat within the error bars.

Before the neutron generalized GDH integral can be extracted, a careful study needs to be conducted to separate the quasielastic contribution from the Δ region. This analysis is ongoing. Once the quasielastic part has been removed, the data will be interpolated to constant Q^2 and then the integration will be performed.

8.8 Extraction of Neutron Results from ^{3}He

In the ground state, the ^{3}He nucleus is primarily in an S state wave function, and the proton contribution to spin-dependent properties cancels due to the pairing of the two proton spins. This simplistic model is complicated by an admixture of the other states: S' and D. The neutron is also subject to binding effects within the nucleus and undergoes Fermi motion, which dampens out the resonance peaks. The ^{3}He wave function components and their nucleon spin configurations are shown in Fig. 8.15. Since the wave function is in an S state about 88% of the time, polarized ^{3}He provides an effective polarized neutron target.

In the DIS region, the spin structure functions can be extracted by using the effective polarization approach:

$$g_{1(2)}^{^3\mathrm{He}}(x) = 2p_\mathrm{p} g_{1(2)}^\mathrm{p}(x) + p_\mathrm{n} g_{1(2)}^\mathrm{n}(x)\,, \tag{8.9}$$

where p_p and p_n are the effective nucleon polarizations in ^{3}He and are given by [115]:

$$p_\mathrm{p} = -0.028 \pm 0.004 \tag{8.10}$$

$$p_\mathrm{n} = 0.86 \pm 0.02\,. \tag{8.11}$$

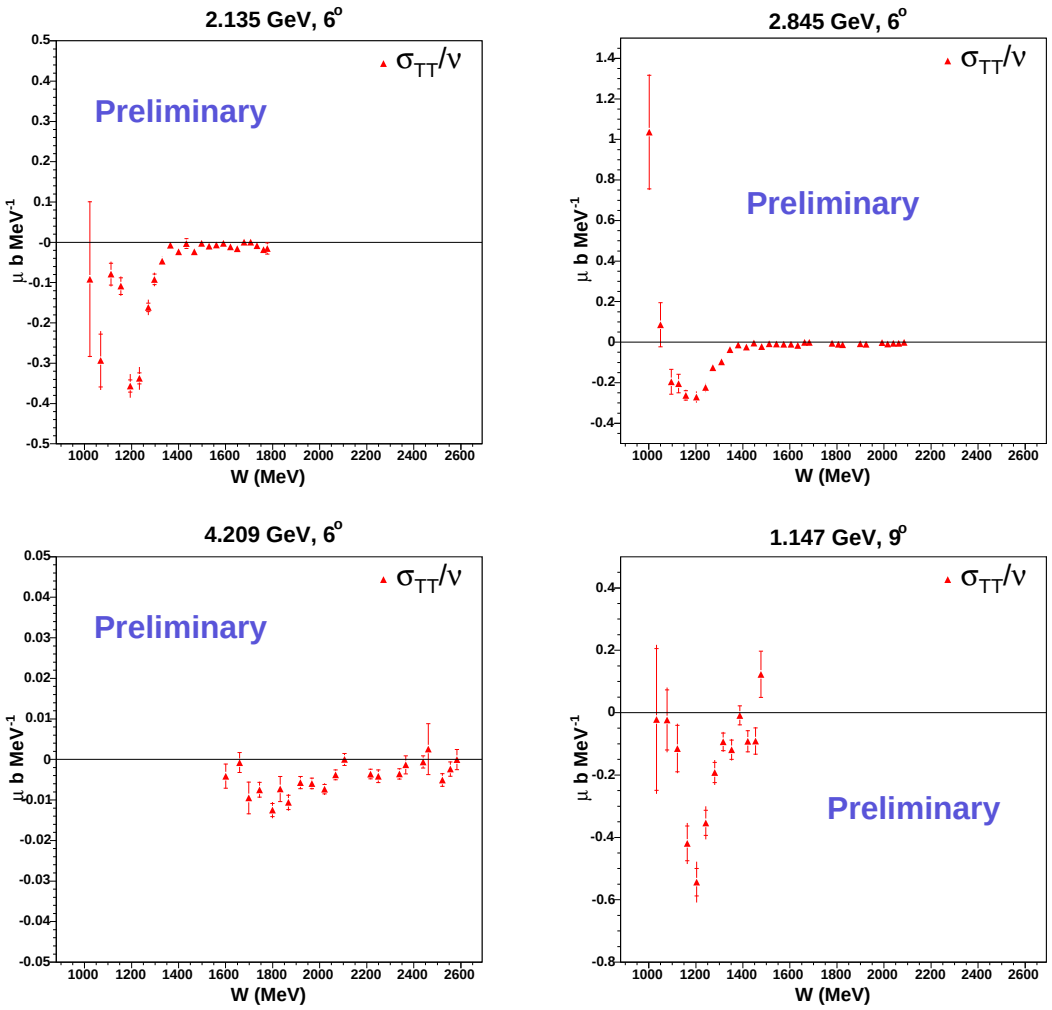

FIG. 8.13: Preliminary results for the ^{3}He GDH integrand measured at constant energy for the 6° and 1.147 GeV, 9° data. The inner (outer) error bars represent the statistical (total) uncertainty.

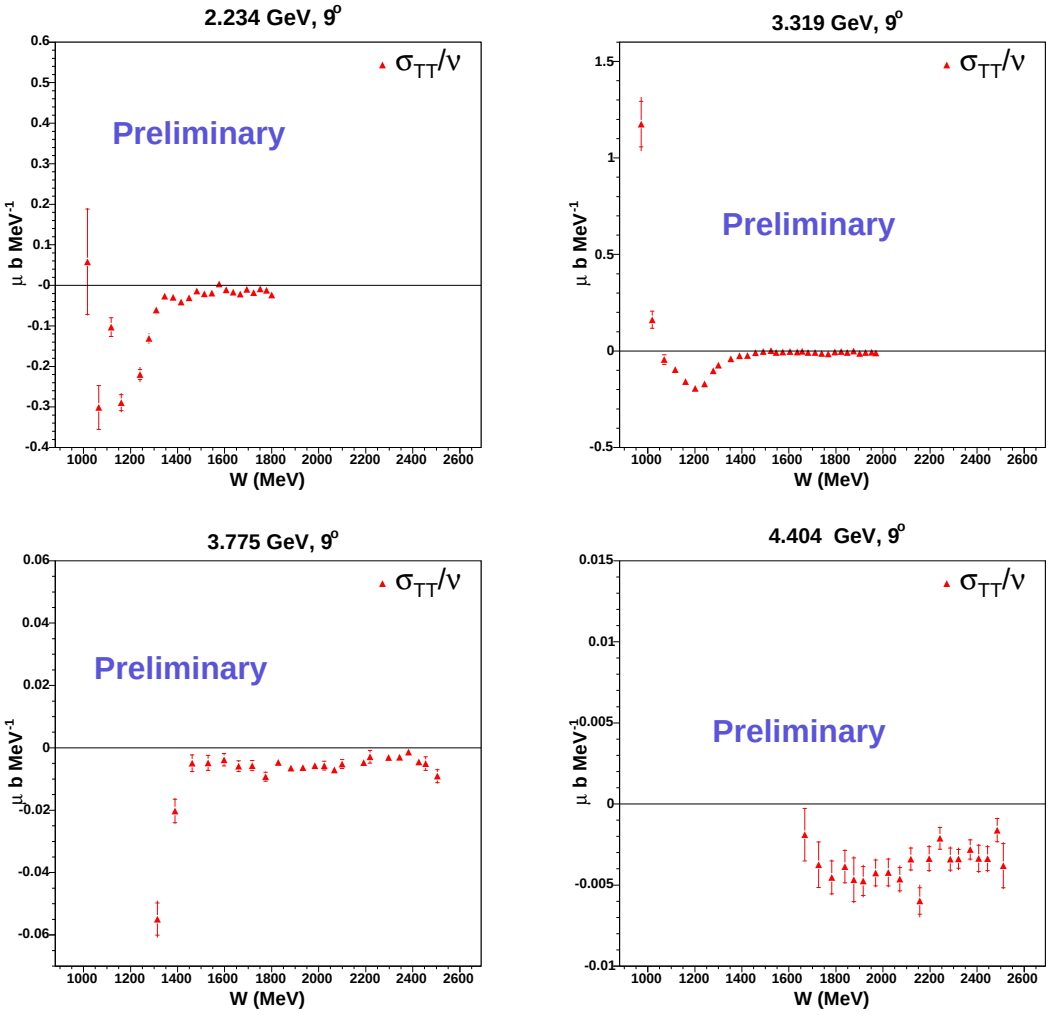

FIG. 8.14: Preliminary results for the ^{3}He GDH integrand measured at constant energy for the 9° data. The inner (outer) error bars represent the statistical (total) uncertainty.

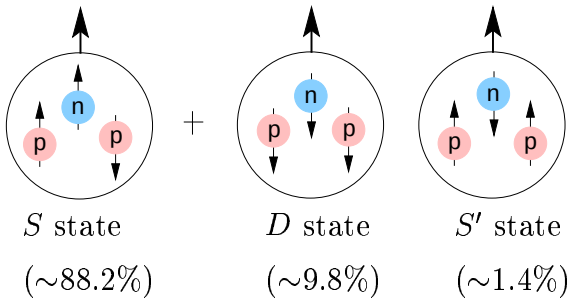

FIG. 8.15: The wave function components of the ^{3}He Nucleus.

In order to include Fermi motion and binding effects, a convolution approach involving the proton and neutron structure functions $g_{1(2)}^{p(n)}$ is used to obtain realistic nuclear structure functions $g_{1(2)}^{A}$. The formalism for the convolution method is available in Ref. [116]. In the DIS regime, it has been found that Eq. (8.9), which neglects Fermi motion and binding effects, shows reasonable agreement with the convolution approach to within 5%.

Scopetta *et al.* have also found that the same does not hold in the resonance region. In this region, Fermi motion significantly broadens and dampens out the resonance peaks compared to the free neutron case. Neither the approximation of Eq. (8.9) or the convolution approach provide reliable neutron results in the resonance region; hence, an alternative approach for the extraction of the neutron spin structure functions from ^{3}He is needed.

For experiment E97-110, we are interested in moments of the spin structure functions and sum rules, which are integrated quantities. Integrating Eq. (8.9) leads to:

$$I^{^3\mathrm{He}}(Q^2) = 2p_{\mathrm{p}}I^{\mathrm{p}}(Q^2) + p_{\mathrm{n}}I^{\mathrm{n}}(Q^2)\,, \tag{8.12}$$

where $I(Q^2)$ represents a sum rule or one of spin structure function moments. The extraction of the neutron integrals is valid in both the resonance and DIS regions [116] with an accuracy of 10% at Q^2 = 0.1 GeV^2. Above 0.5 GeV^2, the approach results in an error

of 5%. The authors have checked the extraction down to 0.01 GeV^2 and have concluded that the extraction from Eq.(8.12) should be reliable to the 10% level [117].

Theoretical work is ongoing [118] to include final state interactions and relativistic effects. In addition to these effects, meson exchange currents and the Δ excitation may play a relevant role.

8.9 Measurement of the GDH Integral

In Fig. 8.16 the expected quality of the results are shown for the neutron extended GDH integral. The vertical scale is normalized to the GDH sum rule at Q^2 = 0. The solid circles show the data from a previous experiment, E94-010 [57]. The statistical uncertainties are shown on the points, and the systematic uncertainties are given by the band at the top of the graph. In the magnified region, the open circles show the Q^2 range, and the dark band at the top of the graph indicates the final expected systematic uncertainty for the integral. The solid curve shows the phenomenological MAID model [54], and the dotted and dashed curves are predictions from Chiral Perturbation Theory [41, 42, 44]. The new data are expected to show a turn-over towards the GDH sum rule for the neutron. Once the quasielastic contribution has been removed, the neutron integral will be extracted from our data down to a Q^2 of 0.035 GeV^2 for the second run period.

8.10 Summary and Conclusions

Experiment E97-110 was conducted to map out the Q^2-evolution of the extended GDH sum rule for the neutron and ^{3}He at low Q^2 between 0.02 and 0.3 GeV^2. This integral is a powerful tool that can be used to study the nucleon spin structure over the full

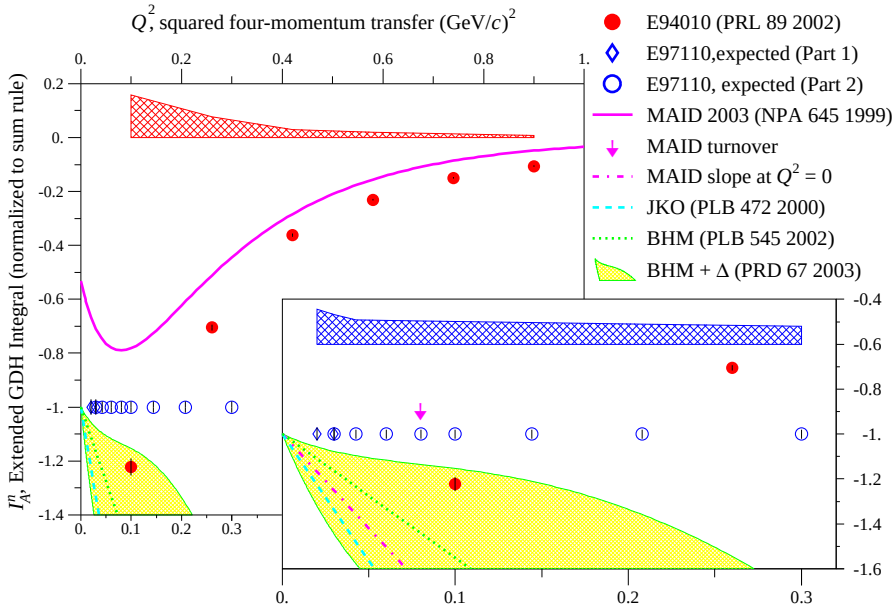

FIG. 8.16: The expected statistical and systematic uncertainties for the neutron GDH integral.

Q^2 range and provides us with a way to investigate the transition from hadronic to partonic degrees of freedom. This unique relation, valid at any momentum transfer (Q^2), can be used to make comparisons between theoretical predictions and experimental data. This experiment was dedicated to provide an important benchmark test of chiral perturbation theory predictions. From these data, the generalized GDH integral, moments of the spin structure functions and forward spin polarizabilities will all be extracted.

In this document, the preliminary analysis and results of the E97-110 ^{3}He data were presented. Both the g_1 and g_2 spin structure functions were calculated and presented. The data show that the quasielastic peak and Δ (1232) resonance have a large contribution for our kinematics as was also seen in the E94-010 data. The transverse-transverse cross section σ_{TT} was also extracted from our data. This data again shows that the quasielastic and Δ regions will have the largest contribution to the GDH integral. Once the quasielastic

contribution is removed from the data, the neutron GDH integral will be extracted. The lowest Q^2 point $\left(0.1\mathrm{GeV}^2\right)$ from E94-010 indicates that the integral falls below the real photon point. The extraction of the integral from our data is eagerly awaited to see if at lower Q^2 the integral turns around and approaches the GDH value at Q^2 = 0. Furthermore, the GDH integral and moments of the spin structure functions for ^{3}He will also be extracted.

APPENDIX A

Optics Reconstruction Issues

When the optimization was completed for the experiment, there were a few outstanding issues that had to be addressed. On close inspection of the sieve slit plots in Fig. 6.10, the central row is shifted toward positive $\phi_{\rm tg}$ (in the direction of the beamline) for the upstream and central foils. The second issue involves the 3.319 GeV data at 9°. Since elastic data is not available at this energy, the optimization process cannot be performed with a clean data set. The final issue is the septum magnet saturation effect. Below we will discuss solutions to these issues.

A.1 Fixing the $\phi_{\rm tg}$ Shift

At first when the $\phi_{\rm tg}$ shift in the central row was seen, the optimization was suspected to need further improvement. However further optimization by including higher order matrix elements only resulted in minor improvements. The shift might be caused by a separation between the septum magnet coils on the beamline side [119]. Since the

standard polynomials cannot reproduce the effect, the shift cannot be fixed within the standard framework of OPTIMIZE++.

A plot of the focal plane distribution for $\theta_{\rm fp}$ and $y_{\rm fp}$ is shown in Fig. A.1. A cut was placed on the central foil to produce this image. In the first order approximation, the plot represents an image of $\theta_{\rm tg}$ and $\phi_{\rm tg}$ in the focal plane. At positive $y_{\rm fp}$, there is small second order dependence on $\theta_{\rm fp}$, but at negative $y_{\rm fp}$, there is a much sharper dependence where the slope of the distribution changes sign at $\theta_{\rm fp}$ = 0. If the same distribution is viewed for the downstream and upstream foils, the dependence at negative $y_{\rm fp}$ changes such that the effect is weaker for the downstream foil and stronger for the upstream foil. This behavior is clearly seen in the target reconstruction, and there is almost no shift in $\phi_{\rm tg}$ for the downstream foil.

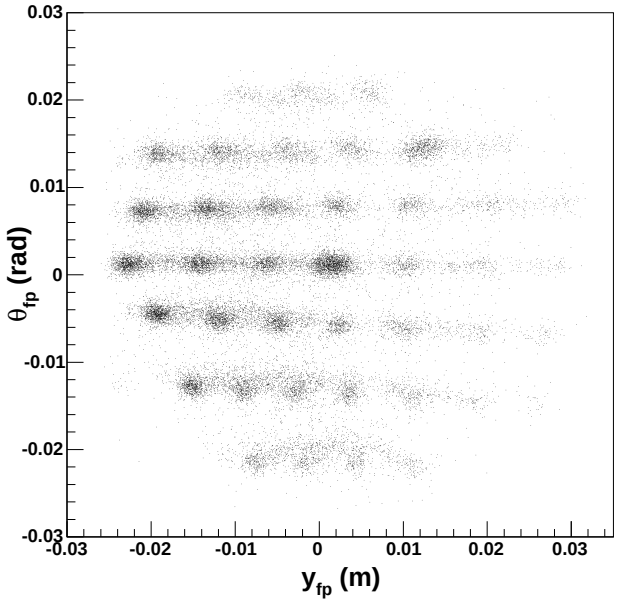

FIG. A.1: Focal plane distribution of $\theta_{\rm fp}$ and $y_{\rm fp}$ with a cut on $z_{\rm react}$ for the central foil. The beam energy is 2.134 GeV.

Since the $y_{\rm fp}$ dependence on $\theta_{\rm fp}$ changes across the focal plane, the standard poly-

nomials cannot adequately compensate for this effect. Since the shape of the focal plane distribution is V-shaped, absolute value terms of $\theta_{\rm fp}$ were added to the $\phi_{\rm tg}$ optimization. Eq. 6.8 was modified for $\phi_{\rm tg}$ by adding the absolute value terms to the standard terms in OPTIMIZE++, see Eqs. (A.1) and (A.2),

$$\phi^{\rm a}_{\rm tg} = \sum_{j,k,l} PTA_{jkl} \left|\theta^j_{\rm fp}\right| y^k_{\rm fp} \phi^l_{\rm fp} \tag{A.1}$$

$$\phi^{\rm c}_{\rm tg} = \phi_{\rm tg} + \phi^{\rm a}_{\rm tg}, \tag{A.2}$$

where ϕ_{tg} is calculated from the standard matrix elements, and PTA_{jkl} corresponds to the tensor for the $\phi_{\rm tg}$ absolute value terms. The order of the focal plane variables in Eq. (A.1) was kept below second order.

For the absolute value terms to be effective, the standard $\phi_{\rm tg}$ matrix elements had to be reoptimized. The procedure followed was to revert to the initial database elements for $\phi_{\rm tg}$, optimize the absolute value terms, and then optimize the standard elements. The sieve slit image is shown in Fig. A.2 before and after optimization using the absolute value terms. The reconstruction for 2.844 GeV at 6° is shown in the top plots, and 2.235 GeV at 9° in the bottom plots.

The $\phi_{\rm tg}$ shift for most of the sieve slit holes was fixed, and the shift in the few remaining holes was reduced by at least a factor of two. A more complicated correction could be applied, but the effect of the remaining shift is expected to be a small systematic effect in the final cross section result. A thorough study of this effect on the cross section will be conducted in the future.

In the case of an extended target (such as the multi-foil target), $y_{\rm tg}$ varies with $\phi_{\rm tg}$ for a foil not located at the origin of the TCS. Due to this connection between the two

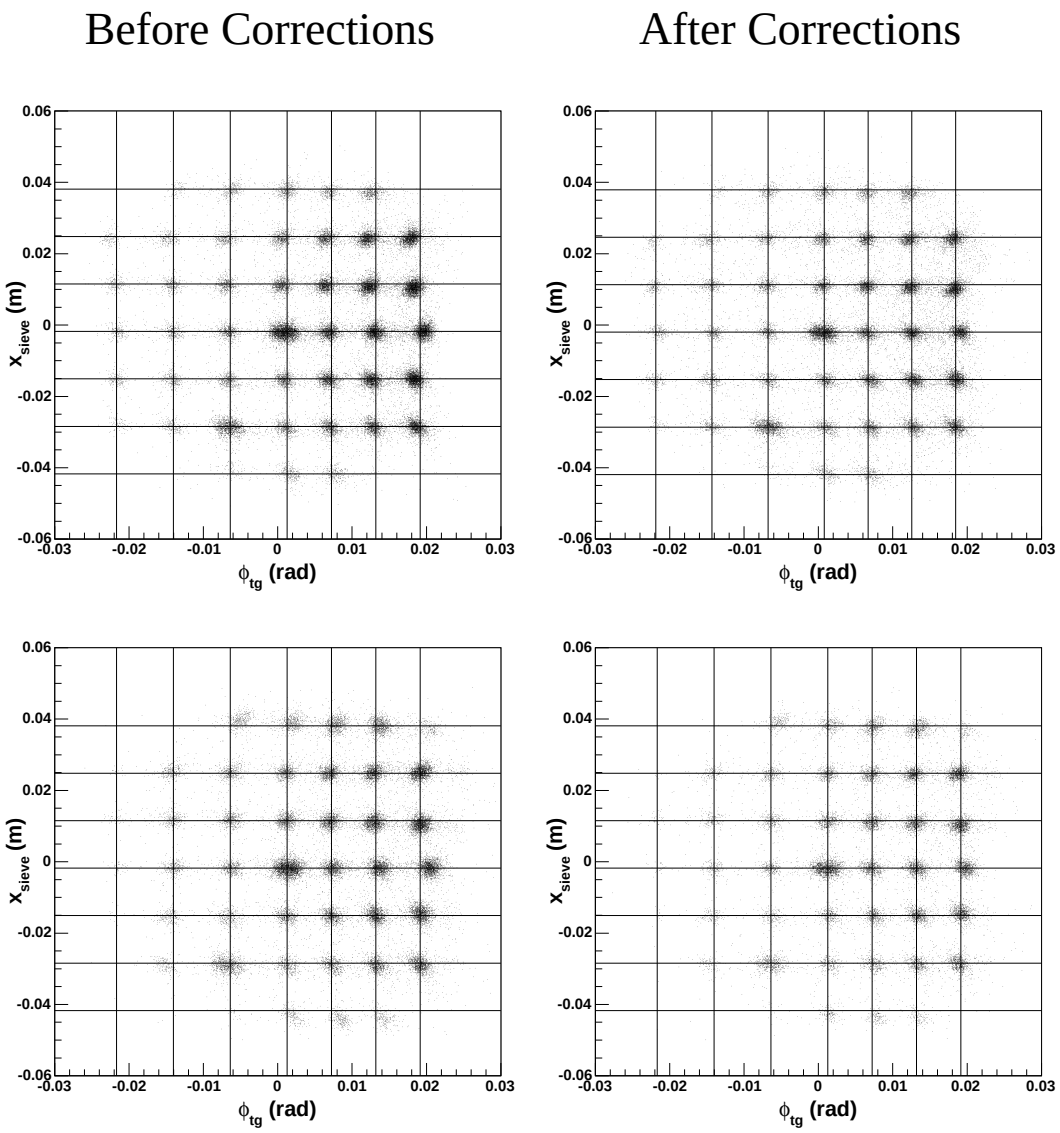

FIG. A.2: Angular reconstruction for the central foil before (left) and after (right) $\phi_{\rm tg}$ absolute value corrections. Top row shows 2.844 GeV, 6° data, and the bottom row shows 2.235, 9° data

variables, a similar shift is seen in $y_{\rm tg}$ for the central row. This is especially evident in the $z_{\rm react}$ spectra in Fig. 6.10. In particular the resolution of the central foil is a factor of two worse than the other foils. A similar correction using absolute value terms in the $y_{\rm tg}$ optimization yielded only minimal improvements in the $y_{\rm tg}$ reconstruction.

A.2 Target Reconstruction for 3.319 GeV

Since the 3.319 GeV optics data at 9° are not elastic, a clean data sample does not exist to do the optimization. In anticipation of this problem, the optics data were taken with a thicker sieve slit to avoid sieve slit punch-through events. The thick sieve slit has five columns and hence only 35 holes. The horizontal spacing of the three columns closest to the beamline is 0.9 cm apart. After the third column, the spacing increases so the columns are 1.2 cm apart. The vertical spacing between the holes is 1.8 cm and is the same for all the holes. Even with the thick sieve slit, the data contained punch-through events, so the optimization was not performed at 3.319 GeV.

The target reconstruction for 3.319 GeV was improved by adjusting a few matrix elements by hand in the 2.235 GeV database. First the spectrometer focal plane offsets for $\phi_{\rm fp}$ and $y_{\rm fp}$ were changed to center the sieve slit and $y_{\rm tg}$ spectra with respect to their nominal positions. Then the $\phi_{\rm tg}$ and $y_{\rm sieve}$ second order dependence on $x_{\rm sieve}$ was removed. The changes to the matrix elements for 3.319 GeV are given in [102]. The sieve slit image is shown in Fig. A.3 before and after the matrix elements were adjusted. After the corrections, the target reconstruction was found to be reasonable.

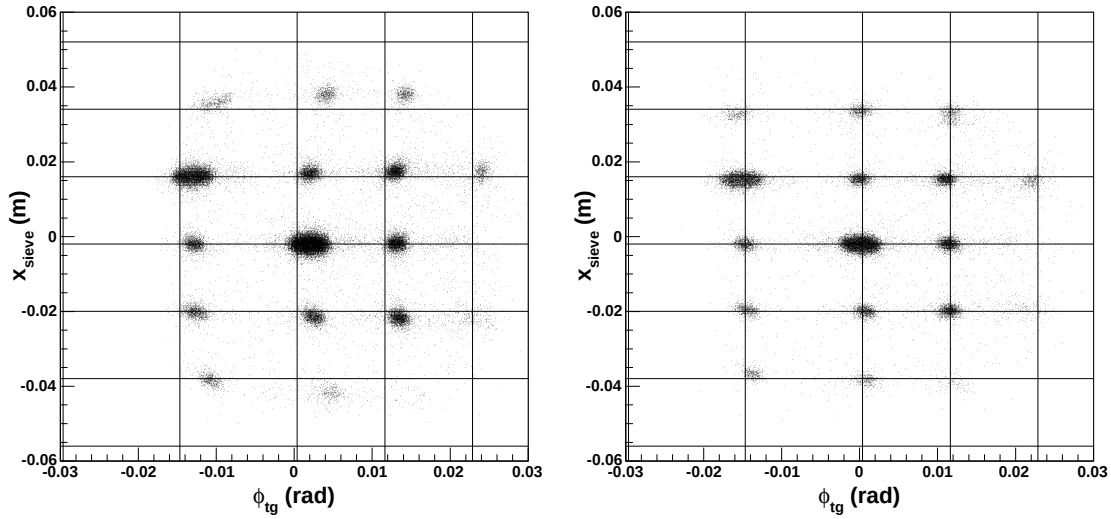

FIG. A.3: Angular reconstruction for the central foil before (left) and after (right) corrections to the matrix elements. The momentum of the spectrometer was at 3.046 GeV/c.

A.3 Septum Saturation Effect

When the 1.096 GeV and 2.844 GeV optics data were replayed with the 2.134 GeV matrix elements, ϕ_{tg} and y_{tg} were shifted with respect to their nominal positions. As mentioned in Section 6.4.5, these shifts are attributed to septum magnet saturation effects. These will be described along with a method to correct for the target coordinate shifts.

A.3.1 The Septum Magnet Tune

The septum bends particles scattered at small angles such as 6° into the spectrometer, which is located at 12.5°. A linear relationship exists for a dipole magnet's field and its bending angle. Additionally the magnet's current and field should also have a linear relationship. Since the septum's current was set independently from the spectrometer momentum, the determination of the relationship between the current and momentum was

crucial. At the beginning of the E97-110 summer run period, the septum magnet current was tuned with the spectrometer momentum. The tune was established by centering the central hole of the sieve slit at the focal plane. The conversion factor used to scale the septum magnet current with the spectrometer momentum at 6° was 92.58 A $(\mathrm{GeV}/c)^{-1}$.

The scaling factor at 9° can be determined by scaling the 6° factor by the ratio of the septum horizontal bending angles at 6° and 9°. The factor calculated for 9° was 128.19 A $(\mathrm{GeV}/c)^{-1}$. When the 9° tune was first established at 3.775 GeV, the conversion factor was found to be 131.94 A $(\mathrm{GeV}/c)^{-1}$. At this beam energy, the central foil y_{tg} position was monitored as the momentum of the spectrometer was decreased. When the central foil position deviated from zero by at least 1 mm, the septum magnet current was adjusted to recenter the foil position. In Fig. A.4, the conversion factor's dependence on the spectrometer momentum is plotted only for the points where the central foil's y_{tg} position was approximately zero. The data were fit to the exponential function given in Eq. (A.3).

$$CF_{\mathrm{sep}} = p_0 \exp(P_{\mathrm{cent}} p_1) + p_2 \tag{A.3}$$

P_{cent} is the central spectrometer momentum, and the fit parameters (p_0, p_1, and p_2) are shown at the top of the figure. The non-linearity of this curve represents the septum saturation effect. For the other beam energies at 9°, the septum magnet current was set based on these fit parameters.

A.3.2 Saturation at 6°

During the acquisition of the 6° data, the septum magnet current was believed to scale linearly with the spectrometer momentum. However this turned out not to be the

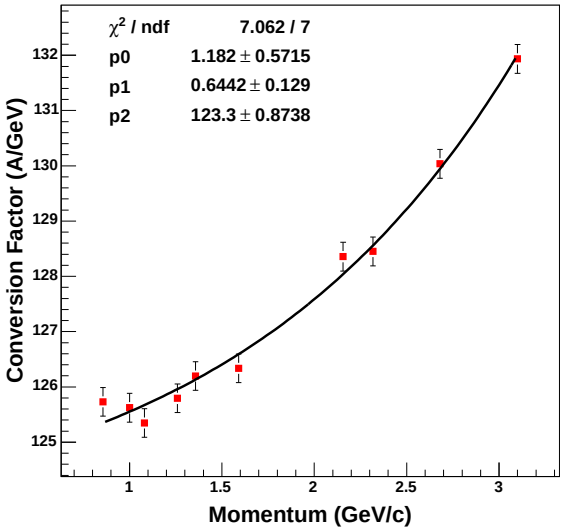

FIG. A.4: Septum magnet conversion factor at 9° based on the central foil's $y_{\rm tg}$ position. The beam energy was 3.777 GeV.

case. When the 2.134 GeV data were optimized, the spectrometer focal plane offsets optimization centered the target coordinates at this energy, but when the tensor elements were applied to the other optics data sets, the target positions were shifted from their nominal values. When no major detector configuration changes are made during an experiment, the offsets in the focal plane variables are expected to be stable.

When the matrix elements were optimized at 1.096 GeV and 2.844 GeV, the focal plane offsets changed to recenter the target positions. If the matrix elements are used to reconstruct the target coordinates at momenta between the optimized settings, shifts occur in $y_{\rm tg}$ and $\phi_{\rm tg}$. When the septum current does not match the required field for the spectrometer momentum setting, the central scattering angle is either a little too large or too small compared to the desired central scattering angle of 6°. Due to the connection between $y_{\rm tg}$ and $\phi_{\rm tg}$ discussed in Section A.1, a shift in $\phi_{\rm tg}$ leads to a shift in $y_{\rm tg}$. Only the

coordinates perpendicular to the dispersive direction are affected, since the septum bends particles in the horizontal plane. These shifts have to be corrected in order to obtain the correct target coordinates.

A.3.3 Database Prescription to Correct Shifts

In order to correct the shifts seen in $y_{\rm tg}$ and $\phi_{\rm tg}$ between the optimized momenta, a correction was applied by using the difference in the focal plane offsets. At the optimized settings, the $y_{\rm fp}$ and $\phi_{\rm fp}$ offsets for 6° and 9° were fit to an exponential. The fit parameters are listed in Table A.1 and defined in Eq. (A.4),

$$y_{\rm fp}^{\rm off} = C_0 \exp(P_0 C_1) + C_2, \tag{A.4}$$

where P_0 is the central momentum of the spectrometer.

Angle	Offset	C_0 (mm)	C_1 $(\mathrm{GeV}/c)^{-1}$	C_2 (mm)
6°	$y_{\rm fp}$	–6.3E–02	1.25	–5.69
	$\phi_{\rm fp}$	–0.82	0.62	0.25
9°	$y_{\rm fp}$	–1.8E–04	2.96	–5.94
	$\phi_{\rm fp}$	–3.7E–02	1.38	–1.04

TABLE A.1: Focal plane offset fit parameters for 6° and 9°.

From these coefficients, the focal plane offsets for each momentum setting were determined. Then the shift in the focal plane offsets between the optimized momentum and the unoptimized momentum is determined by

$$\delta y_{\rm fp} = y_{\rm fp}^{\rm opt} - y_{\rm fp}^{\rm off} \tag{A.5}$$

$$\delta\phi_{\rm fp} = \phi_{\rm fp}^{\rm opt} - \phi_{\rm fp}^{\rm off} \tag{A.6}$$

where $y_{\rm fp}^{\rm opt}$ and $\phi_{\rm fp}^{\rm opt}$ are the optimized offsets from one of the databases. The focal plane offset shifts are then multiplied by the first order $y_{\rm tg}$ and $\phi_{\rm tg}$ matrix elements to obtain the shift corrections at the target.

$$\begin{bmatrix} \delta y \\ \delta\phi \end{bmatrix}_{\rm tg} = \begin{bmatrix} < y|y > & < y|\phi > \\ < \phi|y > & < \phi|\phi > \end{bmatrix} \begin{bmatrix} \delta y \\ \delta\phi \end{bmatrix}_{\rm fp} \tag{A.7}$$

The corrected target variables are then determined from Eqs. (A.8) and (A.9).

$$y_{\rm tg}^{\rm c} = y_{\rm tg} + \delta y_{\rm tg} \tag{A.8}$$

$$\phi_{\rm tg}^{\rm c} = \phi_{\rm tg} + \delta\phi_{\rm tg} \tag{A.9}$$

The data acquired for E97-110 covered the full momentum range of the right spectrometer, and for each angle, this range was divided among the optimized databases. The range of validity for each database was defined in the following manner:

$$R_{\rm lim} = \frac{E_1 - E_2}{2} \tag{A.10}$$

where E_1 and E_2 are adjacent momenta at which the matrix elements were optimized, and $R_{\rm lim}$ is the transition momentum between two databases. Table A.2 gives the valid ranges for the optimized databases.

Angle	Database Energy (GeV)	Lower Limit (GeV/c)	Upper Limit (GeV/c)
6°	1.096	0.872	1.60
	2.134	1.60	2.489
	2.844	2.489	3.40
9°	1.147	0.428	1.691
	2.235	1.691	2.686
	3.319	2.686	3.40

TABLE A.2: Database validity ranges for 6° and 9°.

A module named THaSeptumShiftCor.cxx was written to implement the shift correction procedure for the Hall A ROOT/C++ Analyzer. The Hall A User Software Development Kit [120] was used to build a library for this module, which can then be loaded within a ROOT macro. The module requires no additional input other than what is normally required to run the Analyzer and outputs the shift corrected target coordinates for y_{tg} and ϕ_{tg}.

The database module was tested using data that covered the full momentum range of the spectrometer for all beam energies and at both angles. A comparison for z_{react} is made before and after shift corrections in Fig. A.5 for data taken at beam energies of 2.844 GeV and 4.208 GeV. Since z_{react} is corrected for the beam position, a direct comparison can be made between different momentum settings. After applying the shift corrections at 6°, the z_{react} position was reasonably centered for spectrometer momenta below 2.3 GeV/c. At the highest momentum settings, above 3.0 GeV/c, the shifts were over-corrected. For the 4.208 GeV data, this was confirmed by determining the carbon foil central peak position. Carbon foil data provide a sharp peak at discrete z_{react} positions, which can be compared to the positions from optics data. The shifts between momenta of 2.3 GeV/c and 2.8 GeV/c also appear over-corrected. However, there is no carbon data in this momentum

range to verify this hypothesis. The shift corrections between 2.5 GeV/c and 3.2 GeV/c were scaled to eliminate the excess corrections at these momenta. The plots in Fig. A.5 already have the scaled shift corrections taken into account.

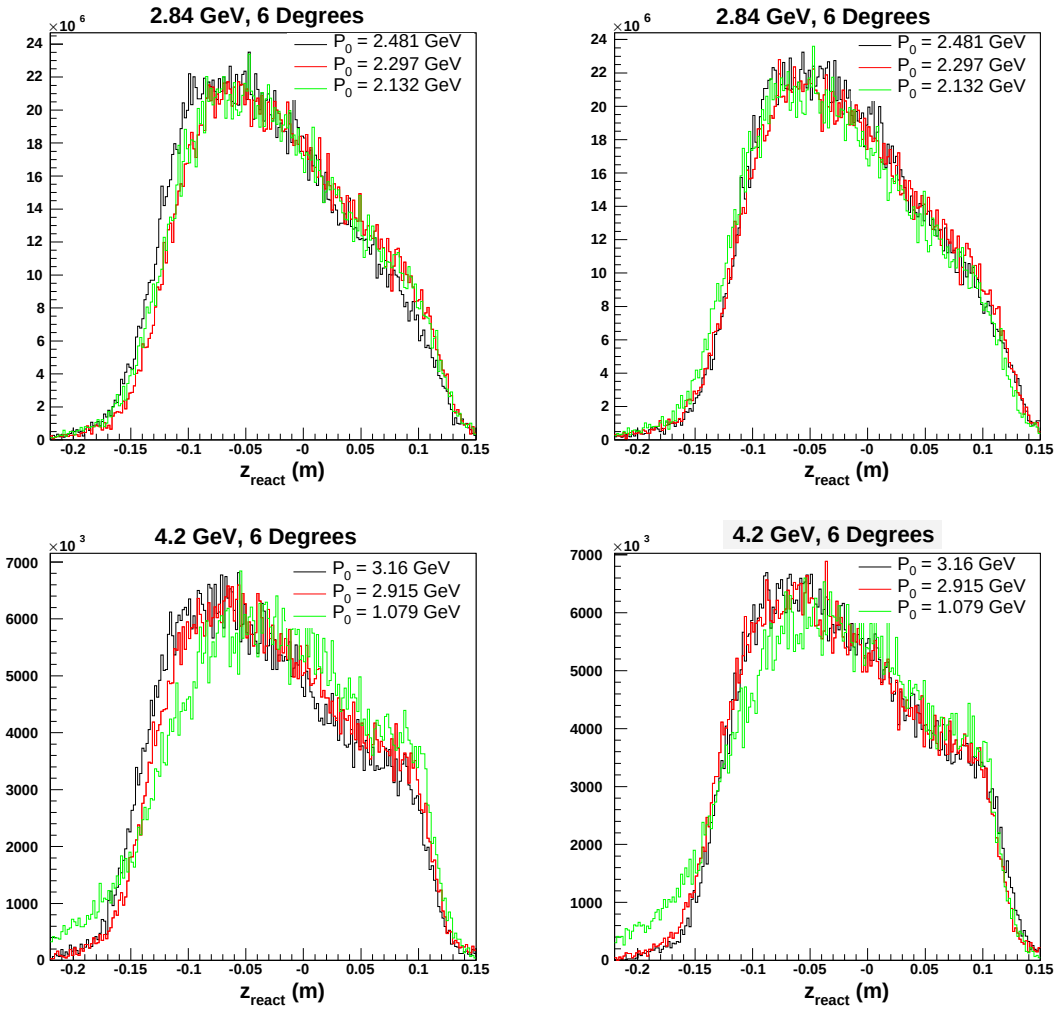

FIG. A.5: Reconstruction for z_{react} before (left) and after (right) shift corrections. In the top row, the 2.844 GeV data is shown, and in the bottom row, 4.208 GeV.

A.3.4 Shift Corrections at 9°

In Section A.3.1, the septum magnet conversion factor for 9° was determined by an exponential fit to data acquired with a carbon foil. Since the septum current was set based on the saturation curve, a shift correction at 9° should not be needed. However, the $y_{\rm tg}$ spectrum was not centered at each momentum setting for the 3.777 GeV energy. Plus there are a few instances where the magnet current was set incorrectly by an Ampere. So a separate correction is needed in these cases.

To determine the corrections for the 9° data, the $z_{\rm react}$ central foil peak was fit with a Gaussian function plus a flat background term for the non-elastic carbon runs. The fit was used to determine the centroid of the peak along $z_{\rm react}$. For each of the runs, the conversion factor was determined from the central spectrometer momentum (P_0) and the septum current ($I_{\rm sep}$).

$$CF_{\rm sep} = \frac{I_{\rm sep}}{P_0} \tag{A.11}$$

In Fig. A.6 the difference between the actual conversion factor and the one from the exponential fit is shown versus the $z_{\rm react}$ position. In the left plot, there are a handful of points below the fit. These points all use the modifications for the 3.319 GeV database mentioned in Section A.2. In the right plot, the spectrometer focal plane offsets in the 3.319 GeV database were replaced by the offsets in the 2.235 GeV database. With the replaced offsets, the outlying points now agree with the rest of the data. For the analysis, the 2.235 GeV offsets will be used for the 3.319 GeV database.

The data were fit to a line without a constant term. This is because when the difference in the conversion factor (ΔCF) is zero, $z_{\rm react}$ should also be zero. For each run, the $z_{\rm react}$ correction is then determined from the slope of the line (p_1), and the corrected $z_{\rm react}$

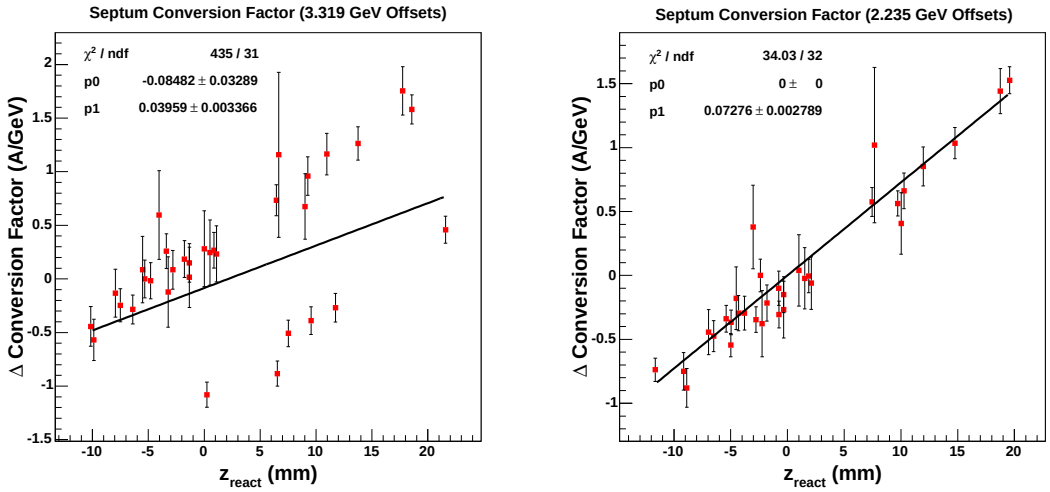

FIG. A.6: Central foil $z_{\rm react}$ positions versus the difference between the conversion factor from the data and one based on the exponential fi t to the saturation curve. Only 9° non-elastic data are included in the plots using the 3.319 GeV spectrometer focal plane offsets (left) and 2.235 GeV offsets (right).

position is given by Eq. (A.13). A similar set of equations exists for the $\phi_{\rm tg}$ corrections discussed below.

$$\Delta z_{\rm react} = \frac{\Delta CF}{p_1} \tag{A.12}$$

$$z^{\rm c}_{\rm react} = z_{\rm react} + \Delta z_{\rm react} \tag{A.13}$$

The shift corrections for $\phi_{\rm tg}$ were determined in a similar manner, but without sieve-slit data, the $\phi_{\rm tg}$ distribution does not have a sharp peak. For the 3.777 GeV data, data exists with the same central momentum but different currents on the septum magnet. By using the average shift from the left and right edge of the $\phi_{\rm tg}$ distribution, $\phi_{\rm tg}$'s dependence on ΔCF can be determined. The shift in $\phi_{\rm tg}$ versus the difference in the septum conversion factor is shown in Fig. A.7. As in the $z_{\rm react}$ corrections, the data were fit to a

line without a constant term. Then the $\phi_{\rm tg}$ correction is determined for each run based on the slope of the line.

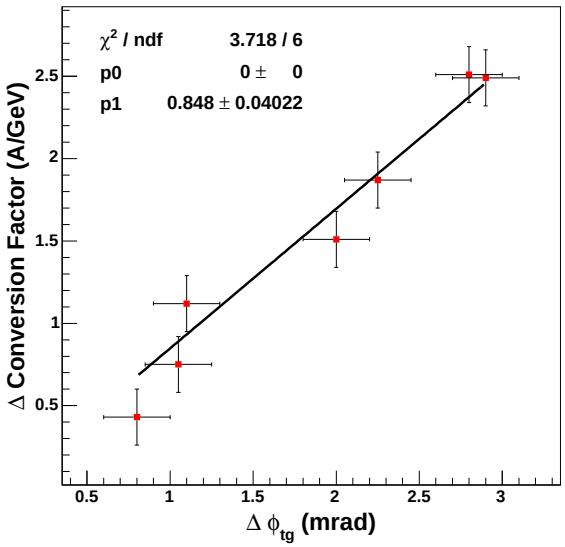

FIG. A.7: Shift in the $\phi_{\rm tg}$ distribution versus the difference between the conversion factor from the data and one based on the exponential fi t to the saturation curve. The shift is determined from data with the same central momentum but different septum currents.

A database was created that contains the $z_{\rm react}$ and $\phi_{\rm tg}$ shift corrections for each 9° run. Since the saturation curve is fairly flat below 1.3 GeV/c, the shift corrections are not used below this momentum. The module created for the 6° shift corrections mentioned in Section A.3.3 was modified to read the database and incorporate the 9° corrections by using Eq. (A.13) and the equivalent equation for $\phi_{\rm tg}$. The corrections were tested and found to work extremely well. The $\phi_{\rm tg}$ and $z_{\rm react}$ distributions are shown in Fig. A.8 before and after shift corrections were applied. The data are from two runs with the same central momentum but different septum currents. After corrections, both $\phi_{\rm tg}$ and $z_{\rm react}$ overlap well between the two runs. For $z_{\rm react}$, the dashed lines indicate the nominal

positions for the carbon foils at 9°. The central foil for both runs is centered with respect to the central line.

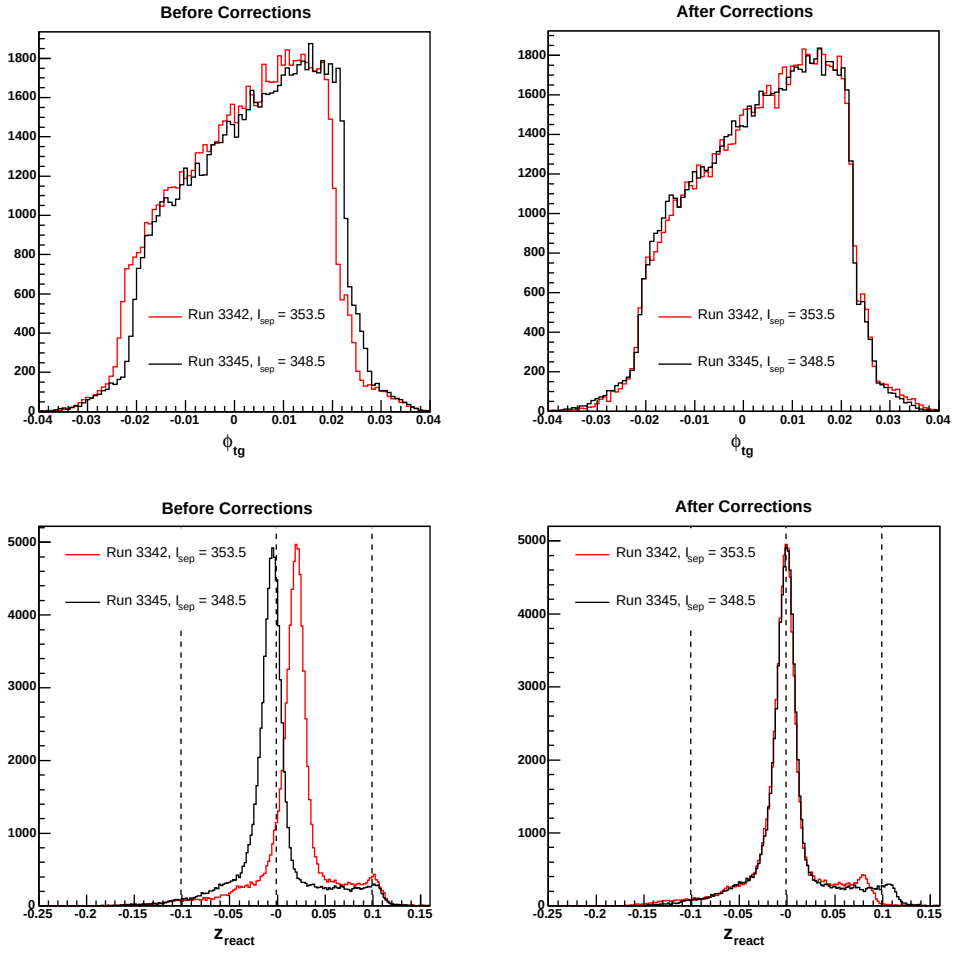

FIG. A.8: The $\phi_{\rm tg}$ (top) and $z_{\rm react}$ (bottom) distributions before (left) and after (right) 9° shift corrections were applied. The dashed lines represent the nominal $z_{\rm react}$ positions.

APPENDIX B

Spectrometer Acceptance

B.1 Spectrometer Acceptance

In Chapter 7, the unpolarized cross section was given by

$$\sigma_0^{\rm raw} = \frac{d\sigma^{\rm raw}}{d\Omega dE'} = \frac{ps_1 N}{N_{\rm in}\rho LT\epsilon_{\rm det}} \frac{1}{\Delta\Omega\Delta E'\Delta Z}\,, \tag{B.1}$$

which is dependent on knowledge of the spectrometer acceptance:

$$\frac{1}{\Delta\Omega\Delta E'\Delta Z}\,, \tag{B.2}$$

where $\Delta\Omega$ is the solid angle acceptance, $\Delta E'$ the momentum acceptance for each spectrometer setting and ΔZ the target length seen by the spectrometer. Due to the fields created by the spectrometer magnets, the acceptance may not coincide with the geometrical apertures of the spectrometer. The acceptance instead depends on the particle's trajectory, momentum and interaction vertex. Hence, the acceptance is determined from a monte carlo simulation [121].

In the simulation, random trajectories are generated that cover an illuminated region that is larger than the actual acceptance in momentum and solid angle. The simulation uses knowledge of the transport properties of the spectrometer magnets and the physical location of the apertures to determine if a randomly generated ray passes through to the spectrometer's focal plane. The acceptance is then extracted by forming the ratio of total generated events to those that pass through the spectrometer apertures and analysis cuts. The acceptance can then be expressed as

$$\frac{1}{\Delta\Omega\Delta E'\Delta Z} = \frac{N_{\rm MC}^{\rm trail}}{N_{\rm MC}^{\rm acc}} \frac{1}{\Delta\Omega_{\rm MC}\Delta E'_{\rm MC}\Delta Z_{\rm MC}} \,, \tag{B.3}$$

where $N_{\rm MC}^{\rm trail}$ is the total number of trial events generated in the simulation. $N_{\rm MC}^{\rm acc}$ is the number of events that survive the transport through the spectrometer model and acceptance cuts. The illuminated solid angle, momentum and target length are given by $\Delta\Omega_{\rm MC}$, $\Delta E'_{\rm MC}$ and $\Delta Z_{\rm MC}$, which were chosen to be larger than the actual values.

For experiment E97-110, fifty million random events ($N_{\rm MC}^{\rm trail}$) were generated for each momentum setting covering a solid angle of 14 mSr. The simulated target length was 40 cm and covered a momentum spread of $\pm$ 7%. The simulation was updated to incorporate tranport functions that include the septum magnet and the collimators used during the experiment.

B.2 Asymmetry Acceptance Cuts

Since the asymmetry is a ratio of cross sections, the acceptance cancels out. This allows us to use larger acceptance cuts in the asymmetry analysis, which is statistically limited unlike the cross sections. For the asymmetry analysis, the following cuts were chosen for the 6° and 9° data:

- $|\theta_{\rm tg}| < 50$ mrad
- $|\phi_{\rm tg}| < 30$ mrad
- $|z_{\rm react}| < 30$ cm
- $|\delta| < 4.5\%$

The target variables are defined in Section 6.4.1.

Additional cuts were included at the collimator locations to remove events that traversed through part of the collimator. These two-dimensional cuts are based on the collimator positions. For the target collimators, the positions were recalculated with respect to the nominal 6° or 9° central ray. Due to the nature of the cuts, it is useful to define variables related to the collimators. The vertical and horizontal position at the sieve-slit collimator aperture are given by $x_{\rm svcoll}$ and $y_{\rm svcoll}$ respectively:

$$x_{\rm svcoll} = x_{\rm tg} + L_{\rm svcoll} \cdot \theta_{\rm tg} \,, \tag{B.4}$$

and

$$y_{\rm svcoll} = y_{\rm tg} + L_{\rm svcoll} \cdot \phi_{\rm tg} \,, \tag{B.5}$$

where $L_{\rm svcoll}$ = 0.833 m from Table 6.11. Two additional variables are related to the transverse position at the target collimators:

$$y_{\rm ucoll} = y_{\rm tg} + L_{\rm ucoll} \cdot \phi_{\rm tg} \,, \tag{B.6}$$

and

$$y_{\rm dcoll} = y_{\rm tg} + L_{\rm dcoll} \cdot \phi_{\rm tg} \,, \tag{B.7}$$

where $y_{\rm ucoll}$ is the transverse position at the upstream target collimator, and $y_{\rm dcoll}$ is the transverse position at the downstream target collimator. The lengths $L_{\rm ucoll}$ and $L_{\rm dcoll}$ are

the distances from the center of the target to the upstream and downstream collimators respectively. These lengths are related to the upstream (downstream) collimator $x_{\mathrm{u(d)}}$ and $z_{\mathrm{u(d)}}$ positions given in Table 6.10:

$$L_{\mathrm{ucoll}} = z'_{\mathrm{u}} = x_{\mathrm{u}} \cos\theta_0 + z_{\mathrm{u}} \sin\theta_0 \,, \tag{B.8}$$

$$L_{\mathrm{dcoll}} = z'_{\mathrm{d}} = x_{\mathrm{d}} \cos\theta_0 + z_{\mathrm{d}} \sin\theta_0 \,, \tag{B.9}$$

where θ_0 is the central angle of the spectrometer: 6° or 9°.

Using the above variables, the following collimator cuts were used in both the asymmetry and cross section analyses for both angles:

- $|x_{\mathrm{svcoll}}| < 0.049$ m
- $|y_{\mathrm{svcoll}}| < 0.028$ m
- $y_{\mathrm{ucoll}} > UCOL$
- $y_{\mathrm{dcoll}} < DCOL$

where $UCOL$ and $DCOL$ are related to the x and z positions of the upstream and downstream collimators respectively and calculated from:

$$UCOL = x'_{\mathrm{u}} = z_{\mathrm{u}} \cos\theta_0 - x_{\mathrm{u}} \sin\theta_0 \,, \tag{B.10}$$

$$DCOL = x'_{\mathrm{d}} = z_{\mathrm{d}} \cos\theta_0 - x_{\mathrm{d}} \sin\theta_0 \,, \tag{B.11}$$

These values are given in Table B.1.

B.3 Cross-Section Acceptance Study

A thorough study of the acceptance was performed testing the reproduction of the target quantities from the simulation. Since the collimators already reduce the target

Angle	$L_{\rm ucoll}$ (cm)	$L_{\rm dcoll}$ (cm)	$UCOL$ (cm)	$DCOL$ (cm)
6°	3.04	41.90	-1.01	0.59
9°	2.41	30.22	-0.85	1.52

TABLE B.1: Target collimator parameters used for the collimator cuts.

length by almost a factor of two, we preferred to keep the acceptance cuts as loose as possible. However two background processes required us to use tighter acceptance cuts.

B.3.1 Background in $\theta_{\rm tg}$

The first background produces a sharp peak in the out-of-plane angle ($\theta_{\rm tg}$) acceptance at -26 mrad. This peak dominates the empty reference cell spectrum as shown in Fig. B.1 and is present for all targets. The events from this peak are also well separated in the

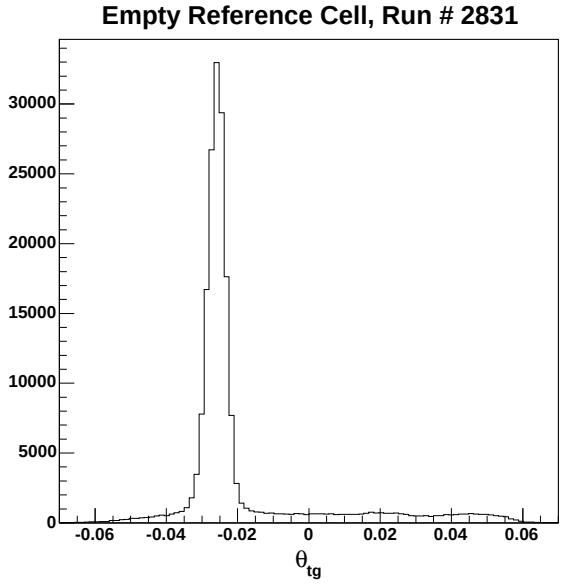

FIG. B.1: Empty Reference Cell Spectrum for $\theta_{\rm tg}$ showing a peak at -26 mrad.

spectrometer focal plane from the main events. These two facts imply that the background

is due to some process independent of the target and is also unpolarized. The peak in the $\theta_{\rm tg}$ acceptance is also seen for the 9° data but is approximately two times smaller. This background can easily removed from the data by subtracting the empty reference cell yield from the ^{3}He yield. However a depression is left in place of the peak after subtraction, which is shown in Fig. B.2. The black curve represents the data, and the simulation, weighted by the Mott cross section, is shown in red. The data were acquired with an incident beam energy of 4.2 GeV and central spectrometer momentum of 1.7 GeV$/c$. In this region, the invariant mass W = 2.3 GeV is beyond the resonance region, and the Mott cross section is expected to approximate the acceptance reasonably well in this region.

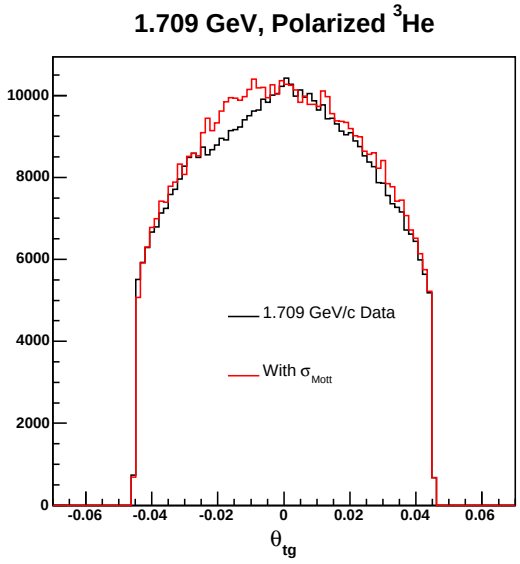

FIG. B.2: Background-subtracted spectrum for $\theta_{\rm tg}$.

The unpolarized cross sections were determined using the full $\theta_{\rm tg}$ acceptance within $\pm$ 45 mrad and the positive half ($\theta_{\rm tg} > 0$ mrad) of the acceptance. For the 6° data, the cross section from the full acceptance was smaller by 4-5%. At 9°, the effect was only

2-3%, which agrees with the factor of two difference seen in the acceptance studies. Since the simulation reproduces the acceptance reasonably well for $\theta_{\rm tg} > 0$ mrad, we decided to only use this region in the cross section analysis. The full $\theta_{\rm tg}$ acceptance was used in the asymmetry analysis. A thorough study of the effects from this background will be conducted in the future, and hopefully the negative half of the acceptance can be kept in the final analysis.

B.3.2 Collimator Background

The collimator cuts are beneficial by removing events from the target cell's glass end windows. However the collimators themselves become a source of potential background. This background results from scattered electrons from the target passing through part of the collimator without being stopped. Electrons that go through this process will lose energy and produce a radiative tail. This is expected to be especially important for electrons scattering elastically, since the elastic cross section is large at 6° and 9°. A study of how the elastic tails are modified by collimator punch-through was studied in Ref. [122]. For the second run period kinematics, the size of the effect is summarized in Table B.2. The

Energy (GeV)	Angle	$\nu_{\rm max}$ (GeV)	Correction
2.135	6°	1.25	5.0%
2.845	6°	1.9	3.5%
4.209	6°	3.2	−2%
1.147	9°	0.7	7.0%
2.234	9°	1.9	3.6%
3.319	9°	1.7	0.3%
3.775	9°	3.0	−2.1%
4.404	9°	3.0	0.9%

TABLE B.2: Collimator punch-through correction from elastic radiative tails.

size of the correction is given for the maximum value of the energy transfer ν for each energy. The correction also includes finite acceptance and target size effects. For the lowest energies, the size of the correction is the largest. Above 2 GeV, the correction is typically $\leq 5\%$.

The study in [122] did not include an estimation for the inelastic contribution; however a full simulation is in preparation to investigate the effect from inelastic punch-through [69].

B.3.3 Acceptance Cuts

Due to the concern about effects from electrons rescattering through the collimators, a set of conservative acceptance cuts were chosen to reduce these effects. The collimator cuts discussed in Section B.2 are tighter than the physical collimator locations. For the cross section analysis, a tighter cut was placed on $z_{\rm react}$ for the same reasons. Because of differences between the 6° and 9° acceptances, slightly different cuts were chosen.

The acceptance cuts for the 6° data are as follows:

- 0 mrad $< \theta_{\rm tg} <$ 45 mrad
- $-$30 mrad $< \phi_{\rm tg} <$ 26 mrad
- $|y_{\rm tg}| <$ 1.5 cm
- $z_{\rm react} <$ 6 cm
- $|\delta| <$ 3.5%
- $(y_{\rm tg} + 1.8\phi_{\rm tg}) >$ $-$0.04 m
- $(y_{\rm tg} + 1.75\phi_{\rm tg}) <$ 0.03 m

The acceptance cuts used for the 9° data are:

- 0 mrad $< \theta_{\rm tg} <$ 45 mrad
- $-$30 mrad $< \phi_{\rm tg} <$ 27 mrad
- $-$1.5 cm $< y_{\rm tg} <$ 2.1 cm
- $z_{\rm react} <$ 9 cm
- $|\delta| <$ 3.5%
- $(y_{\rm tg} + 1.8\phi_{\rm tg}) > -$0.04 m
- $(y_{\rm tg} + 1.75\phi_{\rm tg}) <$ 0.04 m

These cuts are in addition to the collimator cuts discussed earlier. In Fig. B.3, the 6° data at W = 2.3 GeV are compared to the simulation weighted by the Mott cross section using the above cuts with the full $\theta_{\rm tg}$ acceptance.

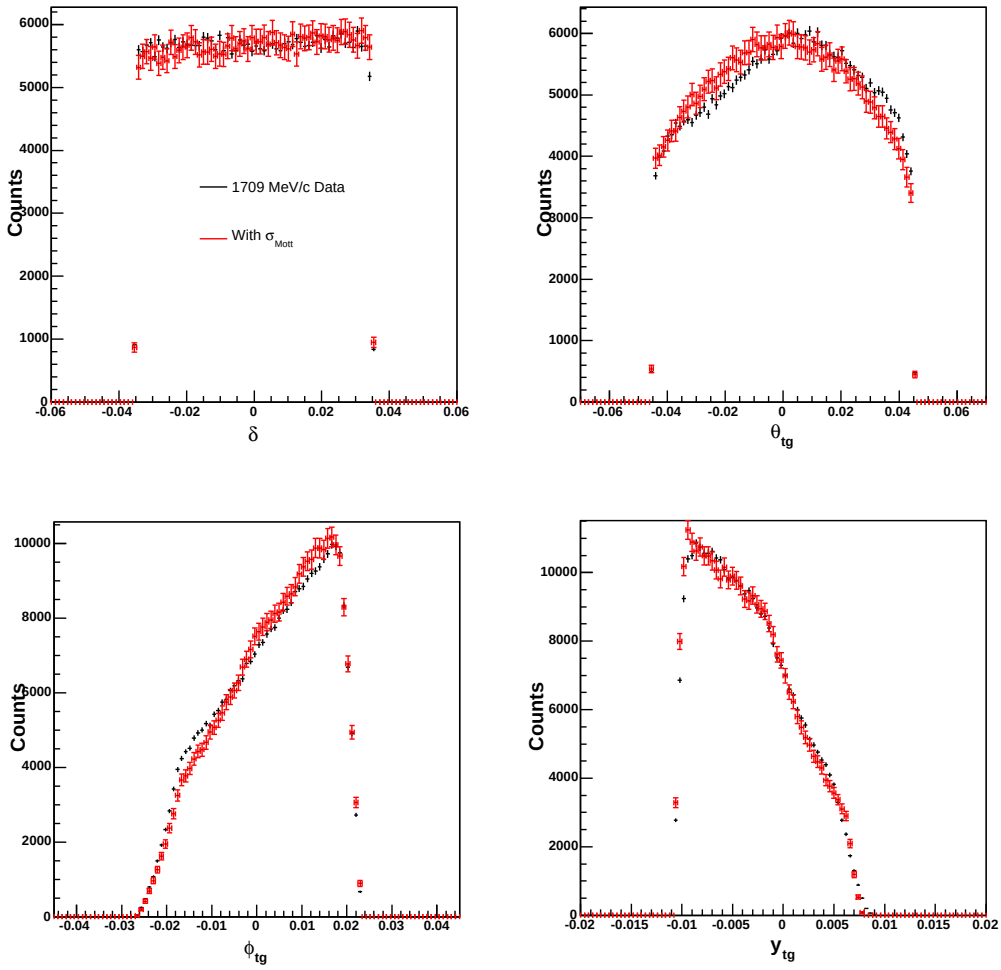

FIG. B.3: ^{3}He target spectrum comparison for δ (top,left), $\theta_{\rm tg}$ (top, right) $\phi_{\rm tg}$ (bottom, left) and $y_{\rm tg}$ (bottom, right).

APPENDIX C

Statistical Uncertainty and Prescale Factors

The statistical uncertainty on the asymmetry is determined from:

$$\sigma_{\rm A} \simeq 2\sqrt{\frac{N^+N^-}{N_{\rm tot}^3}}, \tag{C.1}$$

where $N^+(N^-)$ is the number of events with helicity +1(-1), and $N_{\rm tot}$ = N^+ + N^-. Here the uncertainties on N^+ and N^- are given by the Poisson distribution. In the case when the asymmetry is small enough such that $N^+ \approx N^-$, then the uncertainty on the asymmetry becomes:

$$\sigma_{\rm A} \simeq \sqrt{\frac{1}{N_{\rm tot}}}. \tag{C.2}$$

For experiment E97-110, the majority of the data were prescaled to reduce the burden on the DAQ system and keep the deadtime less than 20%. Unfortunately prescaling complicates the calculation of the statistical uncertainty, so Eq. (C.2) does not give the correct answer when the prescale factor is greater than one. The uncertainty can be corrected by multiplying the number of events by the prescale factor. However this method

is not applicable because the deadtime correction and acceptance cuts need to be taken into account.

A third method was used, instead, that attempts to account for the deadtime and acceptance cuts [69, 123]. In this method, the unprescaled triggers and detected events are treated using a binomial distribution. This is a reasonable assumption since the prescaled events are a subset of the unprescaled triggers. Plus the good events after acceptance cuts are a subset of the total number of detected events without cuts. The following equation was derived using a binomial distribution for the three sets of data:

$$\sigma_{\mathrm{N}^{\pm}} = \frac{ps_1 g^{\pm}}{Q^{\pm} LT^{\pm}} \sqrt{\frac{1}{T_1^{\pm}} - \frac{1}{t^{\pm}} + \frac{1}{g^{\pm}}}, \tag{C.3}$$

where $\sigma_{\mathrm{N}^{\pm}}$ is the uncertainty on the number of accepted events with helicity ± 1 and ps_1 is the prescale factor for T_1 events. Q, LT and T_1 are the helicity-dependent charge, livetime and the number of main triggers, respectively. The total number of detected events is represented by $t^{\pm}$ and the number of good electron events after acceptance cuts by $g^{\pm}$ for the two helicity states. If there is no deadtime and the prescale factor is equal to one, then $\sigma_{\mathrm{N}^{\pm}} = \frac{1}{Q^{\pm}}\sqrt{g^{\pm}}$ and Eq. (C.2) becomes valid again.

BIBLIOGRAPHY

[1] I. Estermann and O. Stern, Phys. Rev. **45**, 761 (1934).

[2] R. Frisch and O. Stern, Zeits. f. Physik **85**, 4 (1933).

[3] J. I. Friedman and H. W. Kendall, Ann. Rev. Nucl. Part. Sci. **22**, 203 (1972).

[4] J. Ashman et al. (European Muon), Nucl. Phys. **B328**, 1 (1989).

[5] A. W. Thomas and W. Weise, *The Structure of the Nucleon* (Wiley-Vch, Berlin, 2001).

[6] X. Zheng, private communication.

[7] M. N. Rosenbluth, Phys. Rev. **79** (1950).

[8] M. K. Jones et al., Phys. Rev. Lett. **84**, 1398 (2000).

[9] O. Gayou et al., Phys. Rev. Lett. **88**, 092301 (2002).

[10] K. J. Slifer, Ph.D. thesis, Temple University (2004).

[11] D. E. Groom et al., Eur. Phys. J. **C15** (2000).

[12] J. D. Bjorken and E. A. Paschos, Phys. Rev. **185**, 1975 (1969).

[13] R. P. Feynman, Phys. Rev. Lett. **23**, 1415 (1969).

[14] C. G. Callan, Jr. and D. J. Gross, Phys. Rev. Lett. **22**, 156 (1969).

[15] Y. L. Dokshitzer, Sov. Phys. JETP **46**, 641 (1977).

[16] V. N. Gribov and L. N. Lipatov, Sov. J. Nucl. Phys. **15**, 438 (1972).

[17] G. Altarelli and G. Parisi, Nucl. Phys. **B126**, 298 (1977).

[18] D. Drechsel, S. S. Kamalov, and L. Tiator, Phys. Rev. **D63**, 114010 (2001).

[19] D. Drechsel and L. Tiator, Ann. Rev. Nucl. Part. Sci. **54**, 69 (2004).

[20] L. N. Hand, Phys. Rev. **129**, 1834 (1963).

[21] F. J. Gilman, Phys. Rev. **167**, 1365 (1968).

[22] S. B. Gerasimov, Yad. Fiz. **2**, 598 (1965).

[23] S. B. Gerasimov, Sov. J. Nucl. Phys. **2**, 430 (1966).

[24] S. D. Drell and A. C. Hearn, Phys. Rev. Lett. **16**, 908 (1966).

[25] M. Hosoda and K. Yamamoto, Prog. Theor. Phys. (Kyoto) **30**, 425 (1966).

[26] F. E. Low, Phys. Rev. **96**, 1428 (1954).

[27] M. Gell-Mann and M. L. Goldberger, Phys. Rev. **96**, 1433 (1954).

[28] J. Ahrens et al. (GDH), Phys. Rev. Lett. **87**, 022003 (2001).

[29] H. Dutz et al. (GDH), Phys. Rev. Lett. **91**, 192001 (2003).

[30] H. Dutz et al. (GDH), Phys. Rev. Lett. **94**, 162001 (2005).

[31] J. Ahrens et al., Phys. Rev. Lett. **97** (2006).

[32] H. R. Weller (HIgS GDH), in *Proceedings of the Third International Symposium on the Gerasimov-Drell-Hearn Sum Rule and its Extensions*, edited by S. Kuhn and J.-P. Chen (World Scientific, New Jersey, 2005).

[33] M. Anselmino, B. L. Ioffe, and E. Leader, Sov. J. Nucl. Phys. **49**, 136 (1989).

[34] R. Pantforder (1998), `hep-ph/9805434`.

[35] X.-D. Ji and J. Osborne, J. Phys. **G27**, 127 (2001).

[36] D. Drechsel, B. Pasquini, and M. Vanderhaeghen, Phys. Rept. **378**, 99 (2003).

[37] H. Burkhardt and W. N. Cottingham, Annals Phys. **56**, 453 (1970).

[38] V. Bernard, N. Kaiser, and U.-G. Meissner, Int. J. Mod. Phys. **E4**, 193 (1995).

[39] J. Goldstone, Nuovo Cim. **19**, 154 (1961).

[40] J. Goldstone, A. Salam, and S. Weinberg, Phys. Rev. **127**, 965 (1962).

[41] X.-D. Ji, C.-W. Kao, and J. Osborne, Phys. Lett. **B472**, 1 (2000).

[42] V. Bernard, T. R. Hemmert, and U.-G. Meissner, Phys. Lett. **B545**, 105 (2002).

[43] C. W. Kao, T. Spitzenberg, and M. Vanderhaeghen, Phys. Rev. **D67**, 016001 (2003).

[44] V. Bernard, T. R. Hemmert, and U.-G. Meissner, Phys. Rev. **D67**, 076008 (2003).

[45] V. Bernard, N. Kaiser, and U. G. Meissner, Phys. Rev. **D48**, 3062 (1993).

[46] V. D. Burkert, Phys. Rev. **D63**, 097904 (2001).

[47] K. G. Wilson, Phys. Rev. **179**, 1499 (1969).

[48] S. Wandzura and F. Wilczek, Phys. Lett. **B72**, 195 (1977).

[49] J. P. Chen, A. Deur, and Z.-E. Meziani, Mod. Phys. Lett. **A20**, 2745 (2005).

[50] B. W. Filippone and X.-D. Ji, Adv. Nucl. Phys. **26**, 1 (2001).

[51] J. D. Bjorken, Phys. Rev. **148**, 1467 (1966).

[52] U.-G. Meissner (2006), `hep-ph/0610200`.

[53] V. Bernard and U.-G. Meissner (2006), `hep-ph/0611231`.

[54] D. Drechsel, O. Hanstein, S. S. Kamalov, and L. Tiator, Nucl. Phys. **A645**, 145 (1999).

[55] R. Fatemi et al. (CLAS), Phys. Rev. Lett. **91**, 222002 (2003).

[56] J. Yun et al. (CLAS), Phys. Rev. **C67**, 055204 (2003).

[57] M. Amarian et al. (Jefferson Lab E94010), Phys. Rev. Lett. **89**, 242301 (2002).

[58] K. Ackerstaff et al. (HERMES), Phys. Lett. **B444**, 531 (1998).

[59] M. Amarian et al. (Jefferson Lab E94010), Phys. Rev. Lett. **93**, 152301 (2004).

[60] P. L. Anthony et al. (E155), Phys. Lett. **B553**, 18 (2003).

[61] M. Gockeler et al., Phys. Rev. **D63**, 074506 (2001).

[62] P. Brindza et al., in *IEEE Transactions on Applied Superconductivity* (2001), vol. 11, p. 1594.

[63] H. -J. Lu, private communication.

[64] L. J. Kaufman, Ph.D. thesis, University of Massachusetts Amherst (2007).

[65] M. Pitt, Technical Report, Helicity Control Requests from the G^0 Experiment, G^0 Collaboration, (unpublished), http://www.jlab.org/∼rom/g0helicity.pdf, (2001).

[66] G. D. Cates et al., Nucl. Instr. Meth. **A278**, 293 (1989).

[67] J. Alcorn et al., Nucl. Instrum. Meth. **A522**, 294 (2004).

[68] M. Jones, Technical Report, Report on BCM calibration for Nov 13 2002 run, Jefferson Lab, (unpublished), (2002).

[69] T. Holmstrom, private communication.

[70] V. Sulkosky, Technical Report, E97-110 Collaboration, (unpublished), http://hallaweb.jlab.org/experiment/E97-110/tech/tech_notes.html, TN-E97110-10, (2006).

[71] C. Yan, Technical Report, Hall C Raster System – The Second Generation, Jefferson Lab, (unpublished), (1997).

[72] Hall A Beam and Polarimeters webpage, http://hallaweb.jlab.org/equipment/beam.html.

[73] P. H. Solvignon, Ph.D. thesis, Temple University (2006).

[74] J. Singh, Small Angle GDH Run Summary webpage, http://www.jlab.org/%7Esinghj/runsummary/.

[75] B. Anderson et al. (Jefferson Lab E95-001), Phys. Rev. **C75**, 034003 (2007).

[76] X. Zheng et al. (Jefferson Lab Hall A), Phys. Rev. **C70**, 065207 (2004).

[77] K. Kramer et al., Phys. Rev. Lett. **95**, 142002 (2005).

[78] J.-P. Chen, Hall A Polarized ^{3}He Target System, http://hallaweb.jlab.org/equipment/targets/polhe3/polhe3_tgt.html.

[79] J. Singh, private communication.

[80] B. Chann, E. Babcock, L. W. Anderson, and T. Walker, Phys. Rev. A **66**, 032703 (2002).

[81] T. J. Killian, Phys. Rev. **27**, 578 (1926).

[82] X. Zheng, Ph.D. thesis, Massachusetts Institute of Technology (2007).

[83] N. R. Newbury et al., Phys. Rev. **A48**, 4411 (1993).

[84] J. Singh, Technical Report, Polarization Gradients in A Two Chambered Cell, Jefferson Lab, (unpublished), http://www.jlab.org/%7Esinghj/runsummary/, (2006).

[85] A. Abragam, *Principles of Nuclear Magnetism* (Oxford University Press, Oxford, UK, 1961).

[86] K. M. Kramer, Ph.D. thesis, The College of William and Mary (2003).

[87] M. Romalis and G. Cates, Phys. Rev. **A58**, 4 (1998).

[88] W. Korsch, Technical Report, E94-010 Collaboration, (unpublished), http://www.jlab.org/e94010/tech_notes.html, TN-E94010-11, (1998).

[89] N. Liyanage, Technical Report, JLab-TN-01-049, Jefferson Lab, (unpublished), http://hallaweb.jlab.org/publications/Technotes/technote.html, (2001).

[90] Details of JLab E94-107 can be found at http://hallaweb.jlab.org/experiment/E94-107/.

[91] J.-P. Chen, A. Deur, and F. Garibaldi spokespersons, Jefferson Lab Experiment E97-110, http://hallaweb.jlab.org/experiment/E97-110/.

[92] K. G. Fissum et al., Nucl. Instrum. Meth. **A474**, 108 (2001).

[93] M. Iodice et al., Nucl. Instrum. Meth. **A411**, 223 (1998).

[94] N. Liyanage, Technical Report, JLab-TN-02-012, Jefferson Lab, (unpublished), http://hallaweb.jlab.org/publications/Technotes/technote.html, (2002).

[95] Survery Reports A879r, A881, A887r and A893, http://hallaweb.jlab.org/news/minutes/Survey_Reports/.

[96] B. Reitz, Analyzing BPMs, (unpublished), http://hallaweb.jlab.org/root/doc/bpm.html.

[97] E. A. J. M. Offerman, ESPACE User's Guide, http://hallaweb.jlab.org/espace/docs.html.

[98] ROOT/C++ Analyzer for Hall A, http://hallaweb.jlab.org/root/index.html.

[99] Physics Analysis Workstation, http://wwwasd.web.cern.ch/wwwasd/paw/.

[100] N. Liyanage, private communication.

[101] V. Sulkosky, Technical Report, E97-110 Collaboration, (unpublished), http://hallaweb.jlab.org/experiment/E97-110/tech/tech_notes.html, TN-E97110-08, (2005).

[102] V. Sulkosky, E97-110 Tensor Elements for the Right HRS, http://hallaweb.jlab.org/experiment/E97-110/analysis.html.

[103] J. Yuan, private communication.

[104] H. -J. Lu, Technical Report, E97-110 Collaboration, (unpublished), http://hallaweb.jlab.org/experiment/E97-110/tech/tech_notes.html, TN-E97110-07, (2005).

[105] V. Sulkosky, Technical Report, E97-110 Collaboration, (unpublished), http://hallaweb.jlab.org/experiment/E97-110/tech/tech_notes.html, TN-E97110-07, (2007).

[106] A. Deur and S. Jensen, Technical Report, E94-010 Collaboration, (unpublished), http://www.jlab.org/e94010/tech_notes.html, TN-E94010-34, (2000).

[107] X. Zhan, Technical Report, E97-110 Collaboration, (unpublished), http://hallaweb.jlab.org/experiment/E97-110/tech/tech_notes.html, TN-E97110-11, (2006).

[108] A. Deur, Technical Report, E97-110 Collaboration, (unpublished), http://hallaweb.jlab.org/experiment/E97-110/tech/tech_notes.html, TN-E97110-04, (2003).

[109] R. Feuerbach, private communication.

[110] L. W. Mo and Y.-S. Tsai, Rev. Mod. Phys. **41**, 205 (1969).

[111] K. Slifer, Technical Report, E94-010 Collaboration, (unpublished), http://www.jlab.org/e94010/tech_notes.html, TN-E94010-44, (2003).

[112] I. V. Akushevich and N. M. Shumeiko, J. Phys. **G20**, 513 (1994).

[113] I. V. Akushevich et al., Comput. Phys. Commun. **104**, 201 (1997).

[114] J. Singh and V. Sulkosky, Technical Report, Radiation Thickness, Collisional Thickness and Most Probable Collisional Energy Loss for E97-110, Jefferson Lab, (unpublished), http://www.jlab.org/%7Esinghj/runsummary/, (2007).

[115] J. L. Friar, B. F. Gibson, G. L. Payne, A. M. Bernstein, and T. E. Chupp, Phys. Rev. **C42**, 2310 (1990).

[116] C. Ciofi degli Atti and S. Scopetta, Phys. Lett. **B404**, 223 (1997).

[117] J.-P. Chen, private communication.

[118] A. Kievsky, E. Pace, and G. Salme, in *Proceedings of the Third International Symposium on the Gerasimov-Drell-Hearn Sum Rule and its Extensions*, edited by S. Kuhn and J.-P. Chen (World Scientific, New Jersey, 2005).

[119] J. LeRose, private communication.

[120] R. Michaels, User Software Development Kit v1.1, http://hallaweb.jlab.org/root /index.html.

[121] A. Deur, Technical Report, E94-010 Collaboration, (unpublished), http://www.jlab.org/e94010/tech_notes.html, TN-E94010-33, (2000).

[122] A. Deur, Technical Report, E97-110 Collaboration, (unpublished), http://hallaweb. jlab.org/experiment/E97-110/tech/tech_notes.html, TN-E97110-06, (2003).

[123] A. Deur, private communication.

[redacted]

Vincent Anthony Sulkosky

Vincent Anthony Sulkosky [redacted] Graduated from Derry Area High School in Derry, Pennsylvania in May 1994. In May 1998, received a Bachelor of Science degree in physics from Saint Vincent College and was awarded the Saint Vincent College Academic Excellence award in physics. During the summer of 1999, he entered the graduate program in physics at the College of William and Mary. In 2000, he joined the Hadronic Physics Group at William and Mary under the guidance of Dr. Todd Averett to develop and enhance his knowledge and experience in experimental nuclear physics. Received a Masters of Science degree in physics from the College of William and Mary in December 2000. He defended this dissertation on 13 April 2007 at the College of William and Mary. In April 2007, he began his post graduate work as a Postdoctoral Research Associate at Jefferson Lab in Newport News, Virginia.